Using Diamonds to Make Photons

by

Peter Clive

Presented as a thesis for the degree of

Doctor of Philosophy

Department of Physics and Astronomy

University of Glasgow

January 2002

Abstract

The possible methods of optimising the use of diamond radiators in producing photon beams to be used in photonuclear experiments was investigated. The photons emitted as a result of scattering electrons in diamond crystals, or radiators, is a useful source of high energy photons for use in photonuclear experiments. A primary electron beam is directed onto the diamond at an angle which produces coherent scattering known as coherent bremsstrahlung, which results in a polarised peak in the photon spectrum. Techniques for selecting the most favourable diamonds have been investigated, using optical and X-ray techniques such as crossed polaroid analysis and X-ray topography to characterise the diamonds with a view to correlating their attributes with their performance as radiators. The consequences which the irradiation the diamonds undergo have for the useful lifetime of the radiators were also investigated, using additional spectroscopic techniques to attempt identification of the crystal defects caused by the radiation damage. Rocking curve analysis, the measurement of the angular spread of X-ray reflections, was used to determine the quality of the lattice structure of the crystals as a predictor of radiator performance in coherent bremsstrahlung experiments. Electron scattering processes not formerly used in this context were investigated to determine their utility; channeling radiation, which is emitted when the electrons' trajectories are confined to directions close to the crystal axis, was generated and found to be useful as a photon beam source, when collimated. A ridge-like structure similar to channeling radiation, but occurring at angles with respect to the crystal axis greater than those consistent with the channeling regime, was observed, which has no precedent described in the literature. Further avenues of investigation are proposed.

Acknowledgements

I would like to express my deep gratitude to my supervisors; to Professor Robert Owens for his insight, patience and forebearance; and to Dr. Ken Livingston for his able assistance and technical expertise. The Stonehenge plot devised by Dr. Livingston was exceptionally useful and must be considered the final word in crystal alignment. As well as Ken, I would like to thank Dr. John Annand for the provision of the robust and stable data acquisition system ACQU which was used to acquire the data in this work relating to electron scattering. The collaboration of Dr. James Kellie in the field of X-ray scattering and matters related to crystal selection has been greatly appreciated also.

I would like to thank Professor Guenther Rosner, the research group head, and the other members of staff who have collaborated and assisted in the work presented in this thesis, Dr. David Ireland, Dr. Douglas MacGregor, Dr Ian Anthony, Dr. Cameron McGeorge and Dr. Dan Watts.

The assistance and advice offered by Jeff Harris as an introduction to the world of diamonds is greatly appreciated. I would like to thank him also for letting me use his petrographic microscope, showing me how to use it and commenting on the things I saw through it. The work using X-rays to assess diamonds benefited enormously from the input of Ranko Vrcelj and I am grateful to David Laundy and Simon Teats for prompt assistance and general advice regarding the operation of experimental station 7.6 at the Daresbury SRS. Also I am grateful to Andrew Lang for general assistance and advice relating to the properties of diamonds and their measurement.

Without the assistance of the technical staff this study would not have been possible. I would like to thank Scott Lumsden who has worked a great deal on developing the silicon strip detector system outlined in chapter 6, Peter Kerr, who has always been ready to chat about cars, and Leslie Murray.

I would like to thank my partner Gillian Ferguson for the support she has given me. Her patience has been perhaps a miracle of nature, certainly she has been tested by this at least as much as I have. My parents and sisters have likewise sustained me.

I would like to extend my thanks to my fellow students for their tolerance of my various foibles and their good companionship. Ruth Sanderson, Lotte Fogg, Steven MacLaughlin, Westley Ingram, Duncan Middleton, Derek Glazier, Finlay MacKay, Andreas Reiter, David Hamilton , Chris Gordon and Joseph Melone have helped sustain me and been forthcoming at those head-scratching times with suggestions and solutions. My fellow students Stephen MacAllister, Stefan Franczuk, Farooq Sadiq, Andrew Scott, Iskender Akkurt and Calum Powrie have moved on to pastures new but their companionship was enjoyed while they were in the group. Chris and Joseph's help in relation to assessing the quality of the Mainz diamond is very much appreciated.

Finally I would like to thank E.P.S.R.C. who funded the studentship.

Declaration

The experimental results presented herein were obtained by the Experimental Nuclear Physics group at Glasgow in collaboration with the group at Mainz. Experimental work was performed in Glasgow, Mainz and Daresbury and I participated fully in all such research. The analysis of the data acquired was performed by me and this thesis was written by myself.

Peter Clive

Contents

Chapter 1

Introduction

1.1 Introduction

A popular source of photons for use in photonuclear studies is the beam generated by scattering a primary electron beam off a crystal radiator. A suitable target can then be placed in the photon beam and the products of the ensuing photonuclear reactions observed. It is necessary for the beam to have well known properties in order to derive information from the experiment about the photons' interactions with the target. The residual energy of an electron can be measured in a spectrometer and associated with a photon by the detection of the electron in time coincidence with the products of the reaction in which the photon participated, this photon having been created by the scattering of the electron. The energy of the photon can be deduced from the energy of the degraded electron. Polarisation information can be obtained by orienting the crystal in relation to the primary electron beam so as to produce coherent bremsstrahlung. This is useful in photonuclear experiments. [1]

The desirability of using polarised photons arises when one considers that, in general, sums and averages over spin states are measured when unpolarised photons are used to determine a photonuclear cross-section. Components of the transition amplitude which are not unambiguously separated can, however, be investigated by a measurement of the photon asymmetry,

$$\Sigma = \frac{d\sigma_{||} - d\sigma_{\perp}}{d\sigma_{||} + d\sigma_{\perp}}$$

where $d\sigma_{||}$ and $d\sigma_{\perp}$ are the differential cross sections using photons polarised parallel and perpendicular to the reaction plane respectively. This allows the cross section to be expressed as

$$d\sigma(\phi) = d\sigma_{unpol.}[1 + \Sigma\cos(2\phi)]$$

where $d\sigma(\phi)$ is the differential cross section for unpolarised photons and ϕ is the angle between the electric vector of the photon and the reaction plane. In practice

$$\Sigma = \frac{1}{P}\frac{Y_{\parallel}^{obs} - Y_{\perp}^{obs}}{Y_{\parallel}^{obs} + Y_{\perp}^{obs}}$$

Where P is the degree of linear polarisation and $Y_{\parallel}^{obs}$ and $Y_{\perp}^{obs}$ are the observed reaction yields parallel and perpendicular to the reaction plane respectively. Knowledge of the photon asymmetry allows investigation of reaction mechanisms that are sensitive to spin variables. Theoretically

$$\Sigma = \frac{W_{TT}}{W_T} = \frac{W^{xx} - W^{yy}}{W^{xx} + W^{yy}}$$

where W_{TT} and W_T are responses of the nucleus to the transverse components of the electromagnetic interaction, such that Σ allows the x and y components of the hadronic tensor, W, to be distinguished. [2]

1.2 Aims & Objectives

The purpose of this study is to investigate the optimisation of the production of real photons in photonuclear studies created by scattering electrons from diamonds. This can be achieved by acquiring greater confidence in the properties of the photon beam, and by ensuring that these properties are suitable for the application. Desirable properties include a high degree of polarisation, and being a tunable source of monochromatic photons. The existing methods of producing a photon beam are examined and improvements proposed. Novel methods involving the production of channeling radiation are investigated. This necessarily involves a knowledge of electron scattering processes in diamond, which are outlined in this chapter.

Another avenue through which optimisation can be achieved is the identification

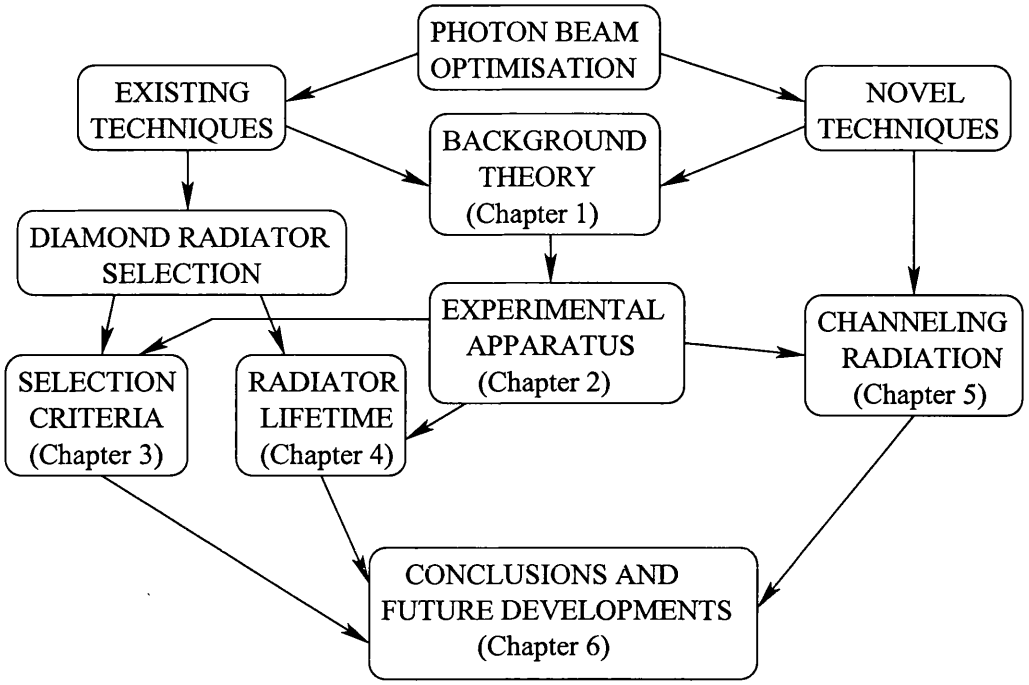

Figure 1.1: A flow diagram illustrating the contents of this study.

of criteria by which more suitable specimens of diamond can be selected for use as crystal radiators. Many of the diagnostic techniques for characterising diamonds involve X-ray scattering, and the theory regarding this is outlined later in this chapter. These and other techniques provide information about the diamonds, and one objective of this study is to ascertain whether such information, which characterises the samples, can be correlated with their performance as diamond radiators in photonuclear experiments. This is discussed in chapter 3.

A diamond can be considered as having a finite lifetime as a radiator due to the severe radiation damage incurred by its use. Samples for the study of this lifetime and indications of when a diamond may be nearing the end of its useful lifetime dose of beamtime are limited by the availability of suitably damaged crystals. However a study of one such sample comprises chapter 4.

An investigation of channeling radiation in order to ascertain its usefulness as a

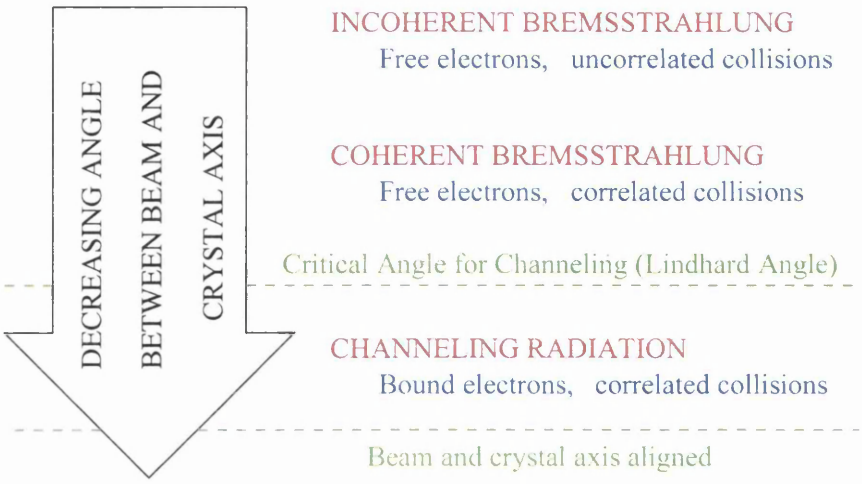

Figure 1.2: The three regimes of electron scattering that occur in diamond.

source of photons for photonuclear studies forms chapter 5. The apparatus and experimental setup and method required to achieve these objectives are described in chapter 2. Chapter 6 outlines the possible directions of future research arising from the work conducted in this study. The structure of this study is shown in figure 1.1. In essence this study addresses three questions.

1. What kind of diamonds are the best to use in photonuclear studies ? This is addressed in chapter 3

2. How is their performance as radiators in these studies degraded by sustained use through radiation damage ? This is addressed in chapter 4.

3. Can they be used in a another way, not currently exploited, such as channeling radiation ? This is addressed in chapter 5.

1.3 The Three Regimes of Electron Scattering

When a well collimated high energy ($\sim 1GeV$) electron beam is incident upon a diamond radiator, photon production is dominated by one of three processes.

These processes are characterised by the angle the primary electron beam forms with the diamond's crystallographic axes. When the beam does not form a small enough angle with one of the crystal major axes the scattering occurs as though an amorphous, non-crystalline radiator was being used. The photon spectrum is determined by the momentum transfer from individual electrons to individual atomic nuclei as if arranged at random, and is the well known and understood incoherent bremsstrahlung spectrum. The electrons remain unbound, and the collisions are uncorrelated. The trajectories of the electrons are not modified by their interaction with the crystal medium in any systematic way. This incoherent contribution is the dominant component of the photon spectrum and emission due to other processes is superimposed upon this. The processes of interest in this study result in features superimposed upon this dominant shape, and so the data presented here relating to the production of photons have been divided through by a reference incoherent spectrum obtained by scattering electrons off an amorphous nickel radiator. This results in the data presented being a relative intensity, $I_{measured}/I_{incoherent}$.

When the crystal is oriented so that the beam forms a smaller angle with a crystal plane, the collisions between an electron and the atomic nuclei become correlated and the momentum transfer can be described as being made to the crystal plane as a whole - the crystal lattice coherently takes up the momentum transfer. In fact the momentum transfer corresponds to a reciprocal lattice vector, as is the case with Bragg scattering of X-rays. However the electrons remain unbound.

Once the angle between the electron beam and the crystal plane or axis falls below a critical level, close to complete alignment, the correlation of the collisions is such as to govern the motion of the electrons; the electrons become trapped in a certain trajectory and radiate as bound electrons. This is the channeling regime, the radiation is termed channeling radiation and the electrons are channeled. The

potential of the nuclei, when averaged along the length of the axis, constitutes a string potential from which the electrons cannot escape, since the energy they have transverse to the string is limited by the angle the beam forms with the axis.

These three regimes of electron scattering in diamond are illustrated in figure 1.2. A review of the theory associated with them follows.

1.4 Crystal Lattice Formalism

To understand the effect of the diamond's crystal lattice and its interaction in momentum space with an incident electron or photon beam it is necessary to have in place the appropriate formalism for describing this interaction. The regular array of atoms in a diamond's crystal lattice is manifested in momentum space as a set of reciprocal lattice vectors which represent a preferred set of momentum transfers. In any scattering process, these momentum transfers are taken up coherently by the lattice rather than incoherently by individual atoms or nuclei. In the case of X-ray or Bragg scattering photons are scattered by the distribution of atomic electrons, whereas in coherent bremsstrahlung electrons are scattered by atomic nuclei, but in both cases the same set of preferred momentum transfers apply, and the same reciprocal lattice representation is relevant.

1.4.1 Direct Lattice in Configuration Space

A crystal presents a periodic potential to an incident beam, $V(\underline{r}) = V(\underline{r} + \underline{L})$ where $\underline{L}$ is a lattice vector corresponding to one of a discrete set of translations in configuration space of the direct lattice. Different kinds of crystal lattice exhibit different degrees of translational and rotational symmetry. The face centred cubic

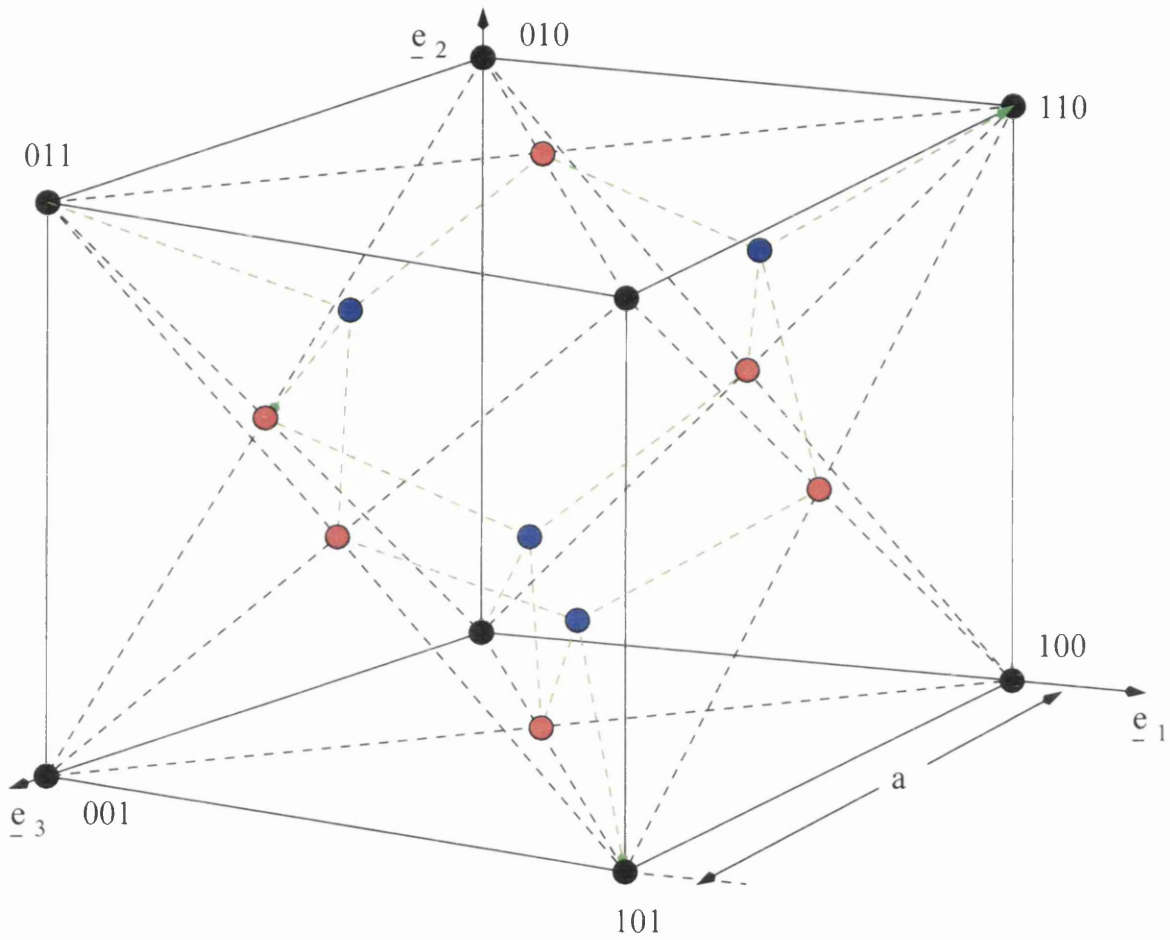

Figure 1.3: The arrangement of carbon atoms in the unit cell of diamond.

lattice (fcc) of diamond will be discussed here.

The atoms in the fcc lattice of diamond are placed in relation to each other in the pattern shown in figure 1.3. Features are colour coded. Black atoms are at the corners of the unit cell, red atoms are at the face centres and blue atoms are at the points $(\frac{1}{4},\frac{1}{4},\frac{1}{4})$, $(\frac{3}{4},\frac{1}{4},\frac{3}{4})$, $(\frac{3}{4},\frac{3}{4},\frac{1}{4})$, $(\frac{1}{4},\frac{3}{4},\frac{3}{4})$, where co-ordinates are measured in units of the lattice constant a = 3.56 Å. Covalent bonds are shown in green indicating their tetrahedral structure, which can be seen on inspecting the atoms wholly enclosed in the unit cell. Each atom forms 4 purely homopolar covalent bonds with its 4 nearest neighbours to give a strong rigid tetrahedral structure. This structure has implications for the Debye temperature of diamond, ensuring it is higher for diamond than for any other material at 2230 K.

It can be seen that a repeating set of atoms or unit cell can be defined which can be used as the basic block which is repeated throughout configuration space to construct the crystal lattice. This is the unit cell, which has three perpendicular axes equal in length (in the case of diamond), $\underline{a}_k = a\underline{e}_k$, where $\underline{e}_i \cdot \underline{e}_k = \delta_{ik}$, i,k = 1,2,3. If we define a radius vector in terms of this basis, $\underline{r} = \sum_{k=1}^{3} ax_k\underline{e}_k$, where x_k is measured in units of a, then we see that the lattice looks the same if it undergoes a translation $\underline{r}$ where x_k are integers, so that under these conditions $\underline{r} = \underline{L} = \sum_{k=1}^{3} an_k\underline{e}_k$, a lattice vector.

A lattice plane is one which contains two lattice vectors, or three lattice points $\underline{L}_i$ one of which can be re-defined to be the origin. If the unit vector normal to the lattice plane is $\underline{n}_0 = \sum_{k=1}^{3} c_k\underline{e}_k$, and no lattice point has been re-defined to be the origin, then the distance from the plane to the origin is $d = \underline{n}_0 \cdot \underline{r}$ where $\underline{r}$ is a point in the plane. Also the distance between the plane and the origin can be found from the points at which the plane intersects the axes, as is shown below. The origin can be considered to be a lattice point which lies in a parallel lattice plane so that this distance can be considered the distance between parallel planes

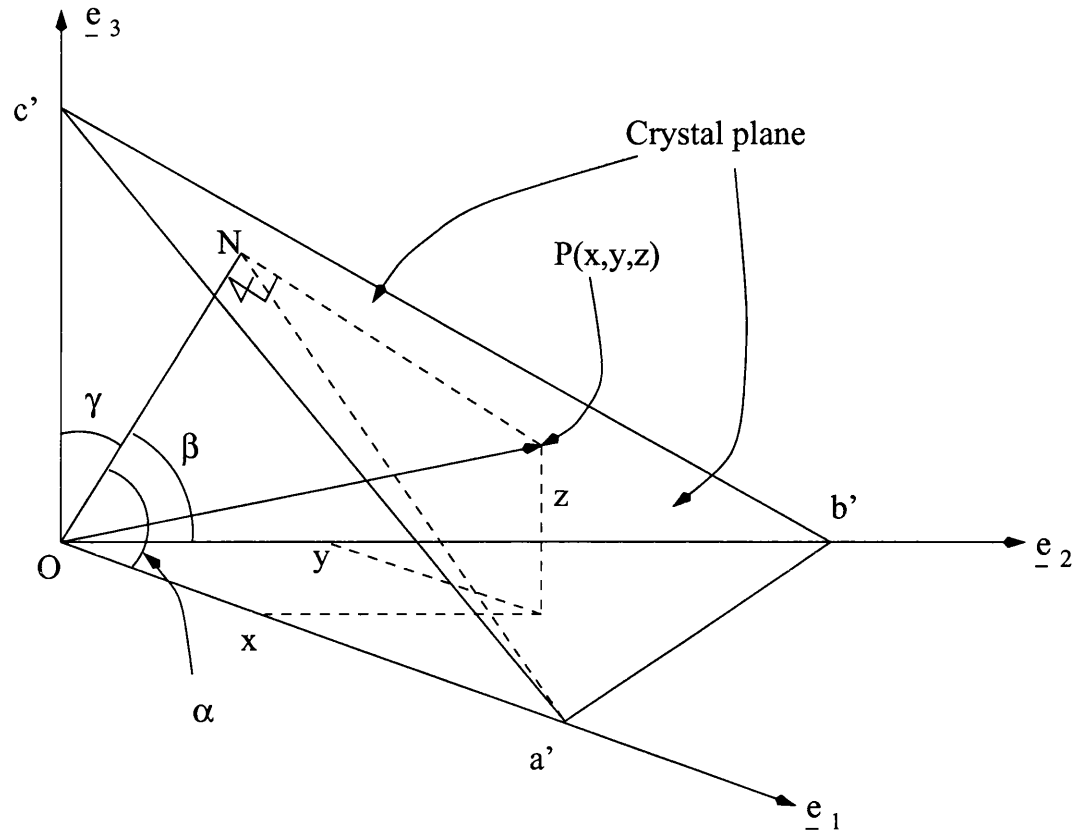

Figure 1.4: A plane intersecting the crystal axes.

belonging to a family or set of parallel lattice planes. The reciprocal of this distance will give the basis of understanding the momentum transfer to the lattice due to scattering processes involving that set of planes.

From figure 1.4 we see that the direction cosines of the normal to the plane are the interplanar distance divided by the axis intersections, $\cos\alpha = d/a'$, $\cos\beta = d/b'$ and $\cos\gamma = d/c'$, where d is the length of the line normal to the plane which extends between the plane and the origin. The projection of a vector terminating on the surface $\underline{r}$, connecting the origin to the point P(x,y,z) on the surface, onto the line perpendicular to the surface through the origin (of length d) is that line itself, shown as ON in the diagram, so $d = x\cos\alpha + y\cos\beta + z\cos\gamma \Rightarrow x/a' + y/b' + z/c' = 1$ is the equation of the plane. If we express the intercepts

and ordinates in units of the lattice constant a we obtain $\sum_{k=1}^{3}(x_k/\alpha_k) = 1$ where α_k are the intercepts expressed in units of a. From this d is obtained by observing that as direction cosines $\cos^2\alpha + \cos^2\beta + \cos^2\gamma = 1$

$$d^2\left(\frac{1}{(\alpha_1 a)^2} + \frac{1}{(\alpha_2 a)^2} + \frac{1}{(\gamma_1 a)^2}\right) = 1 \Rightarrow d = \frac{a}{\left\{\sum_{k=1}^{3}\left(\frac{1}{\alpha_k}\right)^2\right\}^{\frac{1}{2}}} = \underline{n}_0 \cdot \underline{r}$$

If the plane is a lattice plane it contains at least three lattice points $\underline{L}_i = \sum_{k=1}^{3} an_{ik}\underline{e}_k$, $i = 1, 2, 3$ therefore

$$\underline{n}_0 \cdot \underline{r} = \left(\sum_{k=1}^{3} c_k \underline{e}_k\right) \cdot \left(\sum_{k=1}^{3} an_{ik}\underline{e}_k\right) = d \Rightarrow \sum_{k=1}^{3} n_{ik}\frac{ac_k}{d} = 1$$

that is NY = I where the elements of the 3×3 matrix N are n_{ik} and the elements of the 3×1 matrix Y are

$$\frac{ac_k}{d} = \frac{1}{D}\sum_{i=1}^{3} D_{ik}$$

where D and D_{ik} are the determinant and sub-determinants of N, since $Y = N^{-1}I$, and are integers since the elements of N, n_{ik}, are integers. Since $\underline{n}_0 \cdot \underline{r} = d$

$$\sum_{k=1}^{3}\frac{ac_k}{d}x_k = 1 \Rightarrow \sum_{k=1}^{3}\left(\sum_{i=1}^{3} D_{ik}\right)x_k = D \Rightarrow \sum_{k=1}^{3} h_k x_k = H$$

is the equation of the crystal plane on the reduction of D and $\sum_{i=1}^{3} D_{ik}$ by a common divider. H and h_k are integers and x_k are measured in units of a.

1.4.2 Reciprocal Lattice in Momentum Space

It is known that in general the equation of a plane is $\sum_{k=1}^{3}(x_k/\alpha_k) = 1$ therefore $\alpha_k = H/h_k$. The ratios of the axis intersections of parallel planes α_i/α_k are the same and are unaffected by the value of H so that H is an arbitrary integer denoting one of a family of parallel planes characterised by the indices h_k which are termed Miller indices. If H = 1 is taken as representative of this set of planes

it is found that the distance between the plane thus determined and the origin, which is the distance between successive planes in this family of parallel crystal planes, is

$$d_0 = \frac{a}{\left\{\sum_{k=1}^{3} h_k^2\right\}^{\frac{1}{2}}}$$

For example, the plane which intersects the axes at points (1,0,0), (0,1,0) and (0,0,1), which are lattice points, has Miller indices (1,1,1) and $d_0^{1,1,1} = a/\sqrt{3}$. Similarly to the crystal direct lattice in configuration space where each point corresponds to a corner of unit cell and is related to the distribution of atoms in space, a reciprocal lattice can be defined with points corresponding to vectors which characterise each set of parallel crystal planes whose magnitude is proportional to the reciprocal of the interplanar distance and whose direction is normal to the plane

$$\underline{g} = \frac{2\pi}{d_0}\underline{n}_0 = 2\pi \sum_{k=1}^{3} \frac{c_k \underline{e}_k}{d_0} = 2\pi \sum_{k=1}^{3} \frac{a c_k}{d_0} \frac{\underline{e}_k}{a} = 2\pi \sum_{k=1}^{3} h_k \frac{\underline{e}_k}{a}$$

selecting as representative the plane defined by H = 1. This gives a set of basis vectors for the reciprocal lattice $\underline{b}_k = 2\pi(\underline{e}_k/a)$, $k = 1, 2, 3$, so that $\underline{g} = \sum_{k=1}^{3} h_k b_k$ and $g_k = (2\pi/a)h_k$. More generally the reciprocal lattice vectors can be defined as

$$\underline{b}_i = \frac{2\pi(\underline{a}_j \times \underline{a}_k)}{\underline{a}_i \cdot (\underline{a}_j \times \underline{a}_k)}$$

It has been mentioned that this reciprocal lattice representation of the crystal is the most convenient for investigating processes involving momentum exchange taken up by the lattice, and this can be illustrated using the most simple such process, Bragg scattering.

When Bragg scattering occurs the momentum transferred $\underline{q}$ to the lattice is the difference between the momenta of the incident and reflected photons. From geometrical considerations shown in figure figure 1.5 it can be seen that the

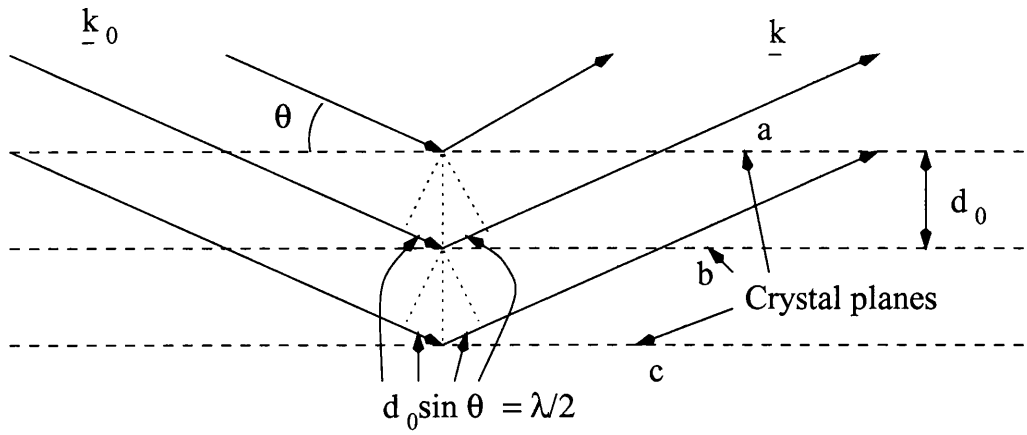

Figure 1.5: X-rays reflected from crystal planes - Bragg's law.

conditions for constructive interference occur when $2d_0 \sin\theta = n\lambda$ where n is an integer. Therefore

$$\underline{q} = \underline{k}_0 - \underline{k} = 2|\underline{k}_0|\underline{n}_0 \sin\theta = \frac{2h}{\lambda}\underline{n}_0 \sin\theta = 2\pi\hbar\frac{n}{d_0}\underline{n}_0 = n\underline{g}$$

as in these units $\hbar = 1$. Reflections for which $n > 1$ are those where there are planes from the same set of parallel crystal planes intervening between those from which the reflections are occurring.

It is apparent from the case of Bragg scattering that the reciprocal lattice vectors are the set of permissible momentum transfers which can be taken up coherently by the lattice rather than by individual atoms or nuclei. The smallest recoil that can be taken up coherently is seen to be $g^{min} = 2\pi/a$.

1.4.3 Structure Factor

The reciprocal lattice is the Fourier transform of the direct lattice. Each unit cell within the lattice however has a distribution of atoms that contribute to the scattered intensity with different phases which need to be added to give a factor which modifies the scattered intensity as determined by the reciprocal lattice. Inspection of figure 1.3 shows the atoms contained within the dia-

mond unit cell and their locations. The factor which modifies the calculation of the scattered intensity is obtained by taking the Fourier transform of the unit cell itself and is termed the structure factor, $\underline{S}_g$, which is a function of the reciprocal lattice vector $\underline{g} = (h_1, h_2, h_3)$ as the relative phases of the reflections from the atoms contained within the unit cell depends upon the orientation of the cell with regard to the incident beam. The structure factor is given by $S = \sum_i f_i \exp\{-2\pi i(h_1 u + h_2 v + h_3 w)\}$ where u, v and w are the co-ordinates of the atoms within the unit cell in units of a, and $f_i = f$ is an atomic scattering factor, found by considering classical elastic scattering, which is termed Thomson scattering. The scattering by the atomic electrons are added with regard to phase just as they are when calculating the structure factor in relation to the locations of the atoms in the unit cell with the exception that the electronic charge distribution is treated as continuous. This gives an integral rather than a summation

$$f_i = \int_{\rho(r)} \rho(r) \exp(2\pi i \underline{q} \cdot \underline{r}) dV$$

where $\rho(r)dV$ is the probability of finding an electron in the volume element dV at r measured from the nucleus and $\underline{q} = \underline{k} - \underline{k}_0 = (2\sin\theta)/\lambda$ is the momentum transfer. f_i is seen to be the Fourier transform of the electron density.

It is apparent that summing over the unit cell will result in contributions from some atoms destructively interfering with contributions from others. It is seen that the structure factor for diamond is given therefore by the expression

$$S = \left[1 + e^{i\frac{\pi}{2}(h_1+h_2+h_3)}\right] \cdot \left[1 + e^{i\pi(h_2+h_3)} + e^{i\pi(h_3+h_1)} + e^{i\pi(h_1+h_2)}\right]$$

where h_k are the Miller indices.

The fcc direct lattice of diamond can be seen as two simple cubic lattices, one displaced by $(\frac{1}{4}, \frac{1}{4}, \frac{1}{4})$ relative to the other. The interference of the reflected flux from the various components of the diamond unit cell can be constructive as well

as destructive. It is seen that

1. $|S|^2 = 64$ if h_k are even and $\sum h_k$ is a multiple of 4
2. $|S|^2 = 32$ if h_k are all odd
3. $|S|^2 = 0$ if h_k are both even and odd or if all h_k are even but their sum is not a multiple of 4

1.5 Coherent Bremsstrahlung

The Bethe-Heitler cross-section describes bremsstrahlung [3]. However in the 1950's and 1960's it became necessary to modify this cross-section to account for orientational effects in bremsstrahlung and particle transmission produced using single crystals [4]. Coherent bremsstrahlung bears a similarity to Bragg scattering. Whereas in Bragg scattering the change in photon momentum must equal a reciprocal lattice vector, coherent bremsstrahlung requires that the change in momentum of the electron and, in addition, the recoil of the emitted photon are taken up coherently by the crystal lattice. In both cases we have q = g, where $g = \sum_{k=1}^{3} h_k\, b_k$ is a reciprocal lattice vector, h_k being the Miller indices and b_k the basis vectors of the reciprocal lattice. In Bragg scattering q = k - k', the difference between the incident and scattered photon momenta. In coherent bremsstrahlung $q = p_0 - p - k$, the difference between the incident electron momentum and the momenta of the scattered electron and emitted photon. If this equals a reciprocal lattice vector the electrons interact coherently with entire crystal planes rather than with isolated atoms and the cross-section is enhanced accordingly [5, 6].

In Bragg scattering the photons are scattered off the atomic electron distribution, whereas in coherent bremsstrahlung electrons are scattered by atomic nuclei, but

the same regular array of atoms in the lattice in both cases means that the same reciprocal lattice representation is relevant.

The kinematics of bremsstrahlung,described below, define a range of possible momentum transfers associated with a given energy of emitted photon. The combination of this with the Bragg condition above and suitable collimation results in a discrete-like spectrum. Coherent bremsstrahlung occurs when one of the crystal's reciprocal lattice vectors falls within the region of possible momentum transfer values known as the momentum 'pancake' or Uberall disk, which is derived from the kinematics of coherent bremsstrahlung.

The primary electron beam has an energy of $E_0 \gg m_e c^2$ and so the radiation is directed into a cone of half angle $\frac{m_e c^2}{E_0}$ around the primary beam direction. The wavelength of the electrons is much smaller than the lattice constant $a \sim \mathring{A}$. However, in conditions where the longitudinal momentum transfer to the lattice is small, its reciprocal, the "effective" lattice parameter that indicates the volume of the lattice sampled by the scattering process is much larger than the unit cell, $q_l \cdot a \ll 1 \Rightarrow a_{eff} = 1/q_l \gg a$ (by the Heisenberg uncertainty principle), so that the interaction of the electrons can be considered to be with the lattice as a whole rather than an isolated atom in it.

An interesting point to note about this characteristic angle of coherent bremsstrahlung,

$$\theta_{char} = \frac{m_e c^2}{E_0}$$

is its relationship with the angle which characterises the angular spread of electrons in the crystal caused by multiple scattering

$$\theta_{scat} = \frac{21.2}{E_0}\sqrt{t}$$

where t is the radiator thickness in radiation lengths (the radiation length of diamond is approximately 0.15m). The ratio of the two is independent of the

primary beam energy, being

$$\frac{\theta_{scat}}{\theta_{char}} = \frac{21.2}{m_e c^2}\sqrt{t}$$

which implies that for the opening angle of the electrons angular distribution caused by multiple scattering not to dominate the behaviour of the spectrum, the radiator must be very thin, of the order of $\theta_{scat}/\theta_{char} = 10^{-4}$ radiation lengths [7], where a radiation length is the distance within which the energetic electron has lost all but 1/e of its energy by bremsstrahlung.

1.5.1 Kinematics of Bremsstrahlung

The range of permitted momentum transfers for a given photon energy is represented in reciprocal lattice space as the Uberall disk. This disk is described by the following inequalities

$$\delta \leq q_l \leq 2\delta \; and \; 0 \leq q_t \leq 2x$$

$$where \; x = \frac{k}{E_0} \; and \; \delta = \frac{1}{2E_0}\frac{x}{1-x}$$

where q_t is the momentum transfer from the electron to the crystal transverse to the beam, q_l is the longitudinal momentum transfer, E_0 is the energy of the incident electron and k is the energy of the photon produced, expressed in natural units $\hbar = c = m = 1$. The reciprocal lattice vector selects a momentum transfer which then determines the energy of the photon via the pancake. Changing the orientation of the diamond, and hence its reciprocal lattice, places the reciprocal lattice vector within a different pancake corresponding to different values of x and k, i.e. a different photon energy.

The electron e is scattered by nucleus N according to the scheme

$$e + N \rightarrow N + e + \gamma$$

$$\underline{p}_0 = \underline{q} + \underline{p} + \underline{k}$$

where $\underline{p}_0$ is the primary electron beam momentum, $\underline{q}$ is the momentum transfer to the crystal lattice, $\underline{p}$ is the emergent electron momentum and $\underline{k}$ is the photon momentum. Natural dimensionless units in which $\hbar = m_e = c = 1$ are employed. Also, neglecting the recoil energy, we have $E_0 = E + k$, where E_0 is the primary beam energy, E is the energy of the emergent electron and k is the photon energy. The photon energy is more conveniently expressed as the dimensionless relative energy $x = k/E_0$.

The kinematics of bremsstrahlung, coherent and incoherent, define a range of momentum transfers longitudinal and transverse to the primary electron beam that are associated with a given energy of photon emission. The rotational symmetry of the process with respect to the primary beam makes analysis in terms of longitudinal and transverse components convenient. Inspection of the diagrams shown in figure 1.6 reveals the range within which the transverse and longitudinal components of the momentum transfer, $\underline{q}_t$ and $\underline{q}_l$, can vary while keeping x constant. In this diagram $\underline{p}_0$ is the primary beam momentum, $\underline{p}$ is the emergent electron momentum, $\underline{k}$ is the photon momentum, $\underline{q}$ is the momentum transfer to the crystal lattice and the subscripts l and t relate to momentum components transverse or longitudinal to the axis defined by the primary electron beam. θ_e is the angle by which the electron is scattered and θ_k is the angle at which the photon is emitted. The diagram on the left of figure 1.6 shows the longitudinal components of the vectors, viewing in a direction perpendicular to the direction of the primary electron beam, while the figure on the left shows the transverse components, viewing them in the direction of the beam.

It is seen that the momentum transfer, $\underline{q} = \underline{p}_0 - \underline{p} - \underline{k}$, has longitudinal and

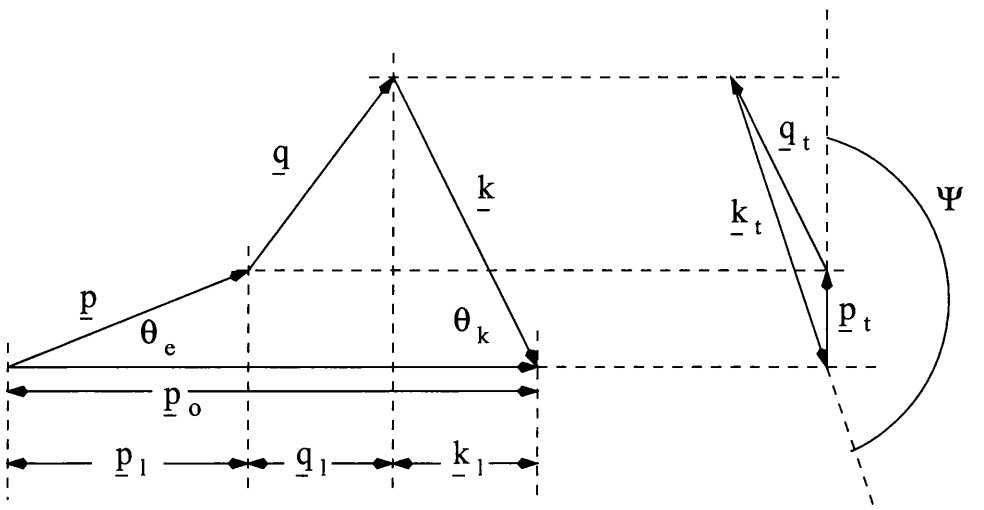

Figure 1.6: The kinematics of bremsstrahlung

transverse components

$$q_l = p_0 - p\cos\theta_e - k\cos\theta_k$$

$$q_t^2 = k_t^2 + p_t^2 + 2k_t p_t \cos\Psi = p^2\theta_e^2 + k^2\theta_k^2 + 2pk\theta_e\theta_k\cos\Psi$$

from which it is apparent that forward emission, $\theta_e = \theta_k = 0$, gives a minimum for q_l of

$$q_l^{min} = p_0 - p - k = \frac{1}{2E_0}\frac{x}{1-x} = \delta$$

using the approximation $p = \sqrt{E^2 - 1} \simeq E - \frac{1}{2E}$, $p_0 \simeq E_0 - \frac{1}{2E_0}$, and since $E = E_0 - k = E_0(1-x)$. This also trivially yields the minimum $q_t = 0$. A maximum of $q_l^{max} = 2\delta$ is obtained by taking $\theta_k = \theta_\gamma = 1/E_0$, since emission is mainly confined within the cone of these dimensions, and $\theta_e \simeq \theta_k\frac{k}{E} = \frac{k}{EE_0}$. This is not as "hard" a limit however as some emission does occur outwith this cone. Taking a small angle approximation, so that

$$q_l = p_0 - p\cos\theta_e - k\cos\theta_k$$

$$\Rightarrow q_l = p_0 - p - k + \frac{1}{2}(p\theta_e^2 + k\theta_k^2) = \delta + \frac{1}{2}(p\theta_e^2 + k\theta_k^2)$$

we find that $q_l^{max} \simeq 2\delta$. Noticing that $\Psi = 0$ gives a maximum for q_t in the above expression of $q_t^{max} = 2x$, giving as limits for the nuclear recoil

$$\delta \leq q_l \leq 2\delta$$

$$0 \leq q_t \leq 2x$$

which defines a "pancake" of permissible momentum transfers in q-space or reciprocal lattice space corresponding to a given relative photon energy x. This is termed the momentum pancake. The pancake for a desired energy can be selected by orienting the crystal such that a reciprocal lattice vector falls within the pancake so that a momentum transfer which results in the desired energy is taken up coherently by the lattice, enhancing that energy in the bremsstrahlung spectrum.

The boundaries of the pancake can be found more exactly by considering that the minimum value of q_l given here only applies when $q_t = \theta_k = \theta_e = 0$. It is necessary to know what the minimum value of q_l is for non-zero values of q_t and θ_k in order to know the effects of collimation which limits θ_k.

The small angle approximation $q_l = \delta + \frac{1}{2}(p\theta_e^2 + k\theta_k^2)$ can be expressed as

$$2(q_l - \delta)/E_0 \equiv Q = (1-x)\theta_e^2 + x\theta_k^2$$

by employing the approximation p = E. q_t is at its largest for $\Psi = 0 \Rightarrow q_t = p\theta_e + k\theta_k$ from which θ_e can be eliminated using this expression for Q to give q_t in terms of θ_k as

$$q_t/E_0 = \sqrt{1-x}\sqrt{Q - x\theta_k^2} + x\theta_k$$

Values of q_t corresponding to non-zero Ψ will be less than this and will correspond to q-values lying within the pancake rather than on its boundary. Differentiating with respect to θ_k gives a maximum of q_t at

$$\theta_k^2 = \hat{\theta}_k^2 = Q \Rightarrow q_t = \hat{q}_t = \sqrt{Q}E_0 = \sqrt{2E_0(q_l - \delta)}$$

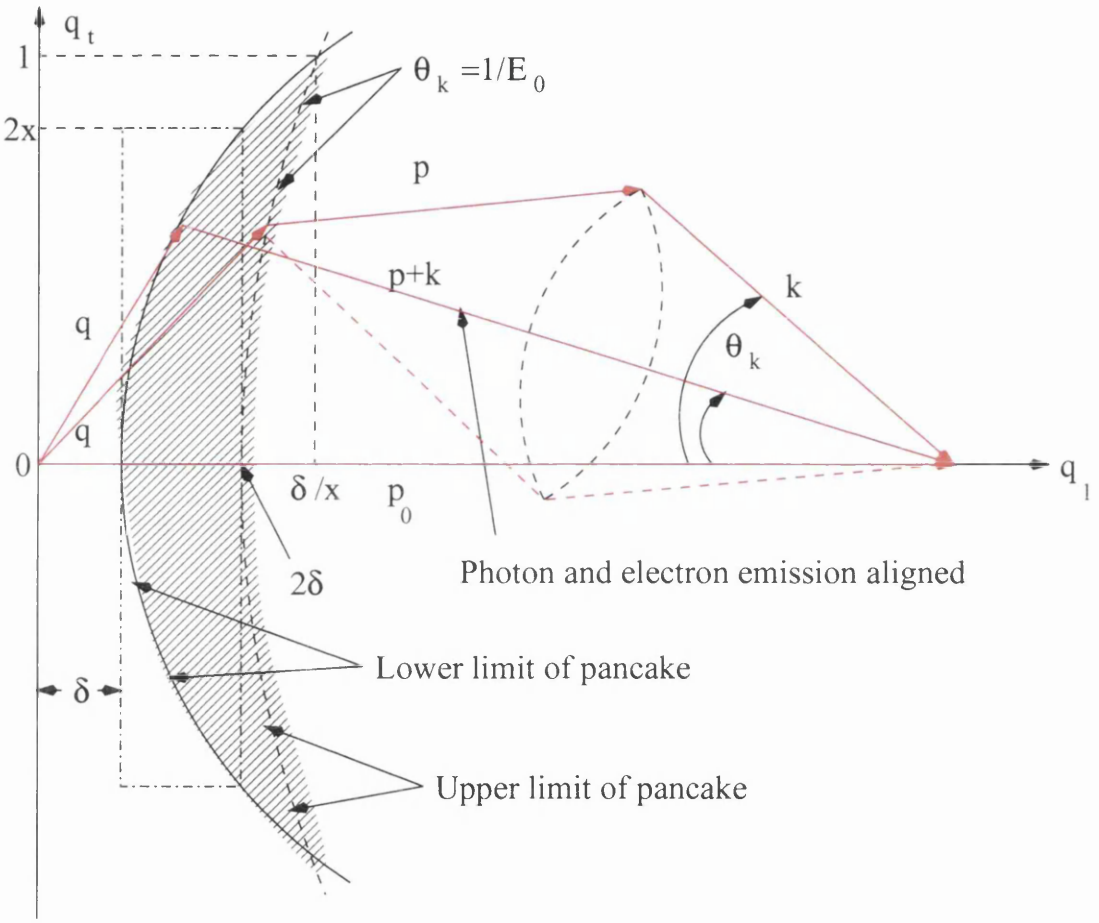

Figure 1.7: The momentum pancake.

$$\left(\Rightarrow \hat{q}_t = \hat{\theta}_k E_0\right)$$

For a given q, if q_t is maximised then q_l is minimised as

$$q_l^{min} = \delta + \frac{\hat{q}_t^2}{2E_0} = \delta + \frac{E_0\hat{\theta}_k^2}{2}$$

giving an expression in terms of q_l and q_t components of the recoil for the lower limit surface of the pancake in q-space showing it to be a paraboloid. At the lower boundary $Q = (1-x)\theta_e^2 + x\theta_k^2$ and $\theta_k^2 = \hat{\theta}_k^2 = Q$ from which it is found that $\theta_k^2 = \theta_e^2 = Q$ and so the emergent electron and the emitted photon are aligned, as seen in figure 1.7 which illustrates the momentum pancake.

To find the upper boundary of the momentum pancake the case $\theta_k = 1/E_0$ is considered. Since $Q = 2(q_l - \delta)/E_0$ and $q_t/E_0 = \sqrt{1-x}\sqrt{Q - x\theta_k^2} + x\theta_k$ we find in general that

$$q_l = \delta + \frac{(E_0\theta_k)^2}{2E_0}\left\{\frac{1}{1-x}\left(\frac{q_t}{E_0\theta_k} - x\right)^2 + x\right\}$$

Taking $\theta_k = 1/E_0$ this gives

$$q_l^{max} = \delta + \frac{1}{2E_0}\left\{\frac{1}{1-x}(q_t - x)^2 + x\right\}$$

which reduces to 2δ if $q_t = 0$. Also, if the maximum for q_t in terms of θ_k given above is inserted $q_l^{max} \simeq \delta + 1/2E_0 = \delta/x$ is obtained. Thus

$$q_l^{min} = \delta + \frac{\hat{q}_t^2}{2E_0}$$

$$q_l^{max} = \begin{cases} 2\delta & \text{if } q_t = 0 \\ \delta/x & \text{if } q_t = \hat{q}_t = 1 \end{cases}$$

The effects of collimation can now be investigated. Until now the pancake corresponding to a given value of x and hence k has been considered, and the various values of q the momentum transfer that will yield this value of x have been found

to lie in a pancake distribution in q-space. Collimation will restrict θ_k and this constraint and a constraint on the recoil momentum will give a range of permitted values for k. For a given q we consider the various momentum pancakes which can contain it and observe the range of x values that give those pancake distributions. Then we consider the portions of these pancakes defined by the restriction placed on the photon emission angle θ_k by collimation.

The upper limit for x corresponds to the lower boundary of the momentum pancake with the highest energy which still contains q. At that boundary

$$q_l = \delta = \frac{1}{2E_0}\left(\frac{x}{1-x}\right) = \frac{1}{2E_0}\left(\frac{x_d}{1-x_d}\right) \Rightarrow x_d = \frac{2E_0 q_l}{1+2E_0 q_l}$$

where x_d is the maximum value of x, the upper limit of its value for a given q. This limit represents a discontinuous drop to zero of the cross-section as it is a result of the "hard" lower limit of the momentum pancake.

A useful convention to adopt when investigating the effects of collimation in specifying a lower limit for x by restricting θ_k is to introduce the relative angles $\vartheta_k = \theta_k E_0$ and $\vartheta_c = \theta_c E_0$ which expresses the emission angle θ_k and collimation angle θ_c as fractions of the natural emission angle $1/E_0$. It is noted also that due to the dimensions of the crystal lattice in use, typically diamond with a lattice constant of 3.56 Å, the typical transverse momentum transfer in coherent bremsstrahlung, $q_t \ll \vartheta_c$. From this we find that the expression for q_l lying within the pancake, in this case the same q but now lying within a pancake corresponding to an $x < x_d$,

$$q_l = \delta + \frac{\vartheta_k^2}{2E_0}\left\{\frac{1}{1-x}\left(\frac{q_t}{\vartheta_k} - x\right)^2 + x\right\} \simeq \delta + \frac{\vartheta_k^2}{2E_0}\frac{x}{1-x} = (\vartheta_k^2+1)\left(\frac{x}{2E_0(1-x)}\right)$$

$$\Rightarrow \vartheta_k^2 = \left(2E_0 q_l \frac{1-x}{x}\right) - 1$$

therefore

$$2E_0 q_l = \frac{x_d}{1-x_d} \Rightarrow \vartheta_k^2 = \left(\frac{x_d}{1-x_d}\frac{1-x}{x}\right) - 1$$

from which it is apparent that the emission angle increases as x decreases. This means that collimation can be used to restrict the emission angle and in doing so suppress emission at lower energies further downbeam than the collimator. Limiting ϑ_k to ϑ_c gives the lower limit for x, x_c, as

$$\vartheta_c^2 = \left(\frac{x_d}{1-x_d}\frac{1-x_c}{x_c}\right) - 1 \Rightarrow x_c = \frac{x_d}{1+\vartheta_c^2(1-x_d)}$$

so that

$$x_c \leq x \leq x_d$$

In the absence of collimation, $\vartheta_c \to \infty$ and x extends down to 0.

To achieve the desired energy of photon emission the crystal is oriented such that a reciprocal lattice vector representing a plane with a high structure factor is placed in the momentum pancake. This causes coherent electron scattering to occur and the radiated spectrum to be peaked. The coherent edge which results from these manipulations is shown in figure 1.8.

1.6 Historical Survey of Channeling Phenomena

In the late fifties and early sixties it became apparent that, as might be expected, there were anisotropies associated with the transmission of charged particles through crystals. It was quickly appreciated that this must in some way be related to the structure and symmetries of the crystal lattice. Anomalously deep penetration occurred when the transmission was aligned with a crystal axis or plane [8, 9, 10, 11]. The first satisfactory explanation of these anomalies was provided by J. U. Lindhard [12] who in 1965 advanced a self-consistent set of approximations that allowed a classical treatment of the problem which yielded a

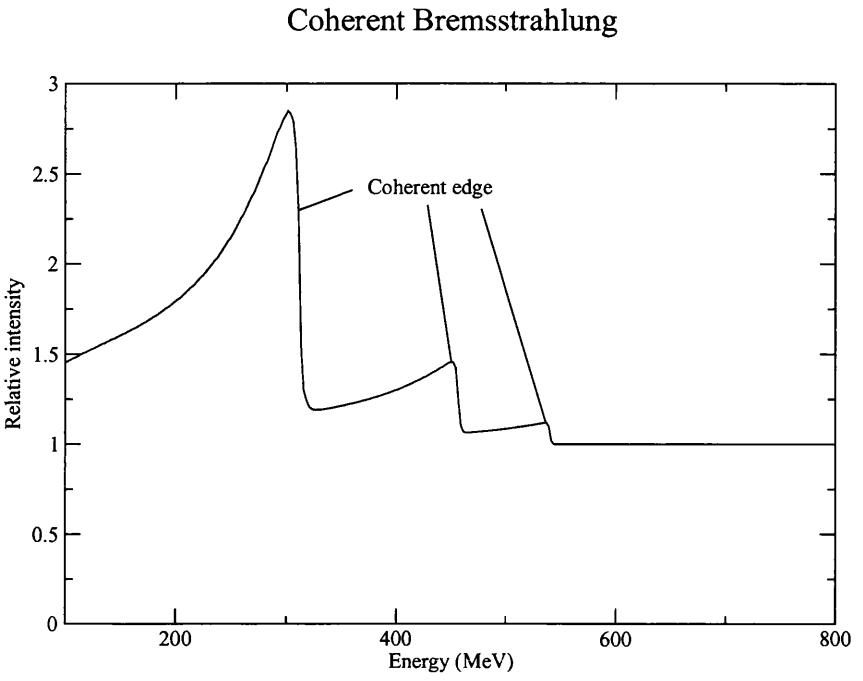

Figure 1.8: Coherent bremsstrahlung.

critical angle, Ψ_l, the Lindhard angle, which describes when to expect channeling to occur. If particle beam is aligned with respect to an axis such that the angle between the two is less than Ψ_l then the particle trajectories become confined along the axis, the particles having insufficient kinetic energy transverse to the axis to overcome the potential barrier posed by it.

The validity of Lindhard's derivation of the axis or string potential was broadly confirmed by experimentalists by observing the flux of particles transmitted through a crystal from a beam or from the decay of embedded radionuclides. Then in 1975 M. A. Kumakhov considered the radiation that must be emitted by charged particles accelerated by a string potential, which he initially approximated as harmonic, and predicted the production of channeling or 'Kumakhov' radiation. Initial interest was stimulated by his prediction that this radiation would be coherent, which subsequently proved to be untrue due to the unrealistic nature of the assumption of a harmonic potential [13, 14].

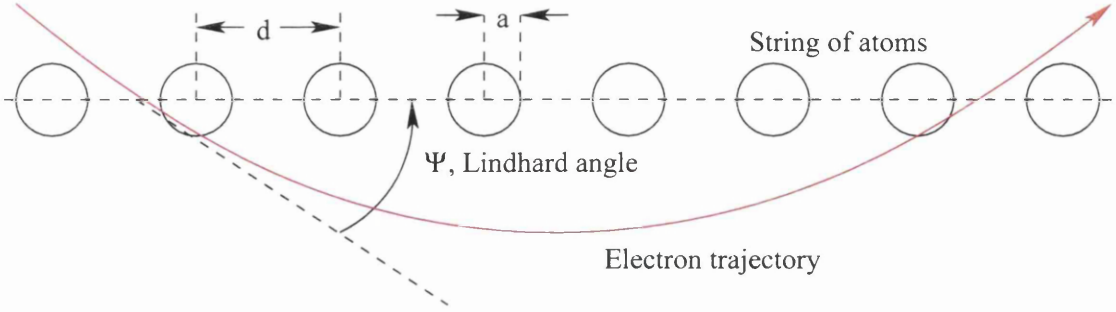

Figure 1.9: Trajectory of an electron undergoing correlated collisions with lattice atoms

In the early eighties the possibility of using a bent crystal as a beam guide was explored as an alternative to cumbersome magnets [15, 16, 17, 18]. It has been proposed that the enhanced pair production that occurs along an axis may form the basis of an improvement in the angular resolution and efficiency of gamma ray telescopes. A further application that occurs to the author is the use of crystals as 'sieves' with which to isolate particular components of a beam, each component having different critical angles due to different charge or mass ($\Rightarrow$ momentum). A given crystal orientation would then select one species by channeling it while deselecting others by blocking.

1.7 Channeling Theory

The phenomenon known as channeling occurs when charged projectiles are incident upon a crystal lattice such that they are confined between crystal planes or along axes. These particles emit a characteristic radiation, known as channeling radiation. One purpose of this study is to investigate the radiation emitted by electrons conforming approximately to the channeling regime using the beam available at Mainz, Germany to ascertain their utility as a source of monoener-

getic linearly polarised photons for use in photonuclear studies. The crystals used are diamonds which have several favourable properties.

In order to achieve the aims of this study a variety of techniques were employed. Coherent bremsstrahlung, which has already been used extensively to produce a high quality photon beam of known energy and degree of linear polarisation, proved useful in orientating the crystals with respect to the beam such that channeling took place. The photon distribution with respect to the crystal angle is symmetrical about the position at which channeling occurs. The quality of the diamonds upon which the beam was incident had to be assessed, and a battery of techniques which addressed various aspects of their suitability was employed, including analysis with polarised light, X-ray topography and rocking curve analysis. In order to resolve the angular distribution of the emitted photons collimation which could be angled to investigate photons emitted off the beam axis was used. Expected developments in this regard involving silicon strip detectors is detailed in chapter 6.

Solids are often treated as dense gases with regard to their penetration by charged particles, and Poisson statistics applied. Exceptions exist, such as Bragg scattering of electrons, coherent bremsstrahlung and particle channeling. Channeling was discovered in the 1960's when ions were found to penetrate further in polycrystalline materials than expected. Strong deviations from normal energy loss were found for ions incident upon a single crystal nearly parallel with an axis. Jens Lindhard's theoretical analysis provided the framework within which this could be understood, supplying a family of approximations valid within a certain energy regime that resulted in the Lindhard or critical angle for channeling, $\Psi_l = (2Z_1Z_2e^2/Ed)^{1/2}$. Z_1 is the charge number of the projectile or particle constituting the beam, Z_2 is the atomic number of the atoms in the crystal, e is the charge on the electron, E is the primary beam energy and d is the distance be-

tween successive atoms in the string of atoms along which the beam is channeled, as shown in figure 1.9. The form of the equation reflects the fact that it is the Coulomb interaction between the projectiles and the string of atoms that is the basis of the string potential. Cgs units are used for concision.

Subsequent applications of channeling are the accurate implantation of ions in semiconductors, the detection of impurities and defects in crystals, and the use of bent single crystals as beam guides.

Channeling in crystals occurs when the incident beam is aligned closely to a crystal axis or plane, causing the collisions between the electrons and the atoms in the crystal to be correlated. This is represented in figure 1.9. The trajectories of the projectile electrons then become trapped or "channeled" between axes or planes and they penetrate further into the crystal. Geometrical transparency does not cause channeling, as is perhaps suggested by a model of a crystal lattice upon viewing along an axis or plane, as a crystal atom is subject to the same flux for random or aligned incidence. Therefore the flux is modified by the lattice, the correlated deflections governing the electron motion. The lattice permits us to approximate the potential by a string of charge. The transverse motion is governed by encounters with individual atoms every $\tau = \frac{d}{v}$. If v is doubled and the angle of incidence halved, the electron experiences the same transverse motion, although the momentum transfer in an individual encounters is halved. Although Bohr's parameter for the strength of the Coulomb interaction with a single atom, $\kappa = 2Z_1Z_2\frac{v_0}{v}$, $v_0 = \frac{e^2}{\hbar}$, is now very small, the interaction is approximated as with the continuum string potential, rather than in terms of the projectiles interaction with single atoms.

Since the path of an electron is nearly a straight line for a single scattering event we can apply the impulse approximation for the momentum transfer which gives us a momentum transfer which is the same in the laboratory and centre of mass

frames, allowing us to consider the motion to be in a fixed external potential. Averaging Lindhard's standard approximation to the Thomas-Fermi potential over the axial direction we obtain the string potential analytically (other atomic potentials can be and are used, but often are only amenable to numerical methods).

$$U(r) = \frac{Z_1 Z_2 e^2}{d} \log\left(\left(\frac{Ca}{r}\right)^2 + 1\right)$$

where $C \simeq \sqrt{3}$, a is the Thomas-Fermi screening radius and r is the axial distance.

Arguments concerning self-consistency, whereby the trajectories calculated using this potential satisfy the conditions that gave rise to the approximations from which the potential was derived, yield the value of the critical angle for channeling, Ψ_l, so that if the angle of incidence $\Psi \leq \Psi_l$, channeling occurs. Similar arguments obtain for planar channeling.

Channeling radiation can be treated several ways. It can be seen classically as connected to the oscillations of the trajectories of channeled particles or quantum mechanically as due to transitions in a potential well corresponding to the trough between strings. For low energy particles ($E \leq 100\ MeV$) the reduced range of transverse energies available for transitions results in a finite number of characteristic lines in the channeling spectrum. For example 16.9 MeV electrons traveling along the (100) plane of silicon have only two bound states. For higher energies of projectile the bound states are so numerous that the spectrum resembles a continuum and the channeled projectiles behave classically, as κ now relates to strings rather than atoms. The increase in the number of bound states which causes the spectrum to tend to a continuum is due to the relativistic contraction of the string which deepens the potential well (between strings in the case of a positively charged channeled particle, or centred on a string in the case of a negatively charged particle). The divergence of the radiation beam is $\sim \frac{1}{\gamma}$

where $\gamma = 1/\sqrt{1 - \frac{v^2}{c^2}}$. This is $\sim$ 1800 for 855 MeV electrons. Such electrons channeled along the $\langle 110 \rangle$ axis of diamond have the peak in this spectrum at around 20 MeV, below the lower limit of my measurements of 50 MeV. However, it is precisely the high energy, off-peak part of the spectrum which is of concern. The systematic exclusion of the peak allows better statistics for this range, by permitting beam currents that would not be tolerable by the apparatus if the peak was being detected.

1.8 Tagged Photons

The production of photons for use in probing the structure of nucleons and nuclei is well established in the Nuclear Physics group at Glasgow. At present coherent bremsstrahlung from electrons in single diamond crystals is used to produce photons of E_γ $\sim$350 MeV and with a degree of linear polarisation of $\sim$50%. The process of coherent bremsstrahlung results in the electric vector being normal to the planes from which the electrons are being scattered. The polarised photons are used in studies of photonuclear reactions. The relative weakness of the electromagnetic to the strong nuclear force means that photons are a good probe of the structure of nucleons and their interactions, and are used for example in the study of (γ,NN) reactions such as the ^{12}C(γ,pp) reaction. Polarised photons are also useful in measuring the polarisability of the pion and in studying meson photoproduction. Coherent bremsstrahlung produces photons with a well defined polarisation state. This means that the measured angle at which the reaction products of interactions between the photon beam and a given target are detected can provide information about whether the interaction was electric or magnetic in nature.

The energy peak in the emission of channeling radiation produced by 855 MeV electrons is characterised by energies too low to be considered useful in this field, but ambiguities exist in the literature about the high energy yield at a small angle to the crystal axis in the range 100 – 1000 MeV which marks the transition from the quantum to the classical regimes in electron channeling.

The experiment has been conducted in a number of stages at the Institűt fűr Kernphysik, Universität Mainz, Germany, with which the Glasgow University Nuclear Structure group have a well established collaboration that has extended over many years. The electron microtron, MAMI-B, that is sited at Mainz, delivers a 100% duty factor 855 MeV electron beam which for the purposes of this experiment is directed into the A2 hall of this facility.

In the A2 hall the beam is incident upon a target crystal held in a goniometer which controls its orientation relative to the beam. The interaction of the beam with the crystal produces photons by coherent and incoherent bremsstrahlung and channeling radiation. Subsequently the energies of the electrons are measured using a tagging spectrometer installed and maintained along with its associated data acquisition hardware and software by the Glasgow group. The energy of a photon can be deduced to within 2 MeV by associating with it an electron of known energy measured in the tagger, using the coincidence of the detection of the photon (or the detection of an event in which it has participated) with the detection of an electron in the tagger.

1.9 X-ray Scattering in Diamonds

Like coherent bremsstrahlung, X-ray scattering reflects the degree of uniformity with which the atoms are arrayed in the crystal lattice, and so is a useful source of information about aspects of diamond quality that relate to photon produc-

tion. Defects in the lattice that will affect photon production will be revealed by analysis of the diamond specimen by means of X-ray scattering.

The theoretical treatment appropriate to this analysis is the dynamical theory of X-ray diffraction. This describes the way in which an X-ray reflection from a crystal plane is not a discrete delta function, but has a minimum width to the curve which describes the way the reflected intensity varies as the orientation of the diamond with respect to the beam changes. This curve is known as the rocking curve. Deviations from this minimum width can yield information about the quality of the diamond for the purposes of photon production. Variations in lattice quantities over the bulk of a sample can be revealed using X-ray topography, which involves acquiring images of the specimens from its X-ray reflection, and again is best understood in the context of the dynamical theory. However, in order to initially set the terms of reference for an elucidation of the dynamical theory, the more familiar kinematical theory will be outlined first, as is conventional.

1.9.1 Kinematical X-ray Diffraction Theory

As in coherent bremsstrahlung, the momentum transfer from the scattered X-ray is taken up coherently by the crystal and therefore is represented by a reciprocal lattice vector. The energy transfer to the crystal is neglected, and in the case of X-ray scattering, this means that the polarisability of the crystal medium is ignored [19], and the refractive index is unity. This assumption is valid for weak scattering and is revised in the case of the dynamical theory. The Fraunhofer or far field approximations of conventional optics, whereby the observer is far removed from the point of scattering in comparison to the dimensions of the volume illuminated, imply that the scattered rays are effectively parallel. The paradigmatic example of the kinematical theory is Bragg scattering.

The electrons are forced to oscillate by the incident X-ray and radiate at the same frequency in all directions. The scattered intensity is found to depend upon the polarisation of the incident X-ray relative to the dispersion plane, and is expressed as a fraction of the incident intensity as

$$\frac{I}{I_0} = \frac{C^2 r_e^2}{R^2}$$

where R is the distance to the observer, $r_e = e/m_e c^2$ is the classical electron radius expressed in cgs units, in which this theory is most concisely expressed, and C is the polarisation dependent factor. If θ is the Bragg angle, $C = \cos 2\theta$ in the case of π polarisation whereby the electric vector is parallel with the dispersion plane, and $C = 1$ in the case of σ polarisation whereby the electric vector is perpendicular to the dispersion plane. In the double crystal experiments included in this study σ polarisation was selected, that is, the electric vector was perpendicular to the plane in which the X-rays were being scattered.

This angular variation applies only to the scattering from an isolated electron and the scattered intensity will be modified by the interference effects which result from the regular array of the electrons in the crystal lattice. To evaluate the interferential effects an interference function $J = \sum_i \exp(2\pi i \underline{r}_i \cdot \underline{q})$ is used which expresses the addition of the X-rays scattered from each unit cell i located at $\underline{r}_i$ from the origin. The scattered amplitude is then $A = S_{hkl} J$ where S_{hkl} is the structure factor for the reflection with Miller indices h,k, and l, and the scattered intensity is $I = A^2$. When the Bragg conditions are satisfied the interferential effects result in a maximal scattered intensity.

The circumstances in which the planes reflecting the X-rays are perpendicular to the surface of the sample, and the X-rays enter the sample at one surface and exit at the opposite surface, sampling the whole depth of the sample, are termed transmission geometry or the Laue case of diffraction. When reflection is

from planes parallel with the surface one is dealing with the reflection geometry, termed the Bragg case. In the Bragg case the X-rays only penetrate to about an extinction distance into the depth of the diamond, and so only the region of the sample near the incident surface are surveyed. The forward scattered intensity, which propagates into the sample in the incident direction, varies sinusoidally due to dynamical effects which will be described below, and the depth at which this intensity reaches zero is the extinction distance.

The extinction distance x is given by the expression

$$x = \frac{V \cos\theta_B}{\lambda r_e |S_{hkl}| C}$$

where V is the volume of the unit cell, θ_B is the Bragg angle, λ is the X-ray wavelength, S is the structure factor and C is the polarisation factor (C=1). In the work presented in this thesis x was typically of the order of 10 microns.

1.9.2 Dynamical X-ray Diffraction Theory

The dynamical theory is the appropriate description of the X-ray scattering phenomena that occur when using X-ray topography to investigate the specimen's potential as a radiator. The whole crystal can be illuminated and the image acquired from the scattered intensity can reveal the distribution and nature of defects that are present in the sample. These images can be taken using an incident beam with a "white" spectrum, or using an incident beam that has been monochromated using a double crystal geometry. A monochromator is a crystal other than the one to be investigated which is placed in the white beam at an orientation that reflects one wavelength onto the sample being investigated. Double crystal geometry can give greater topographic contrast, which will be discussed in chapter 3. The defects that are revealed can be associated with features ap-

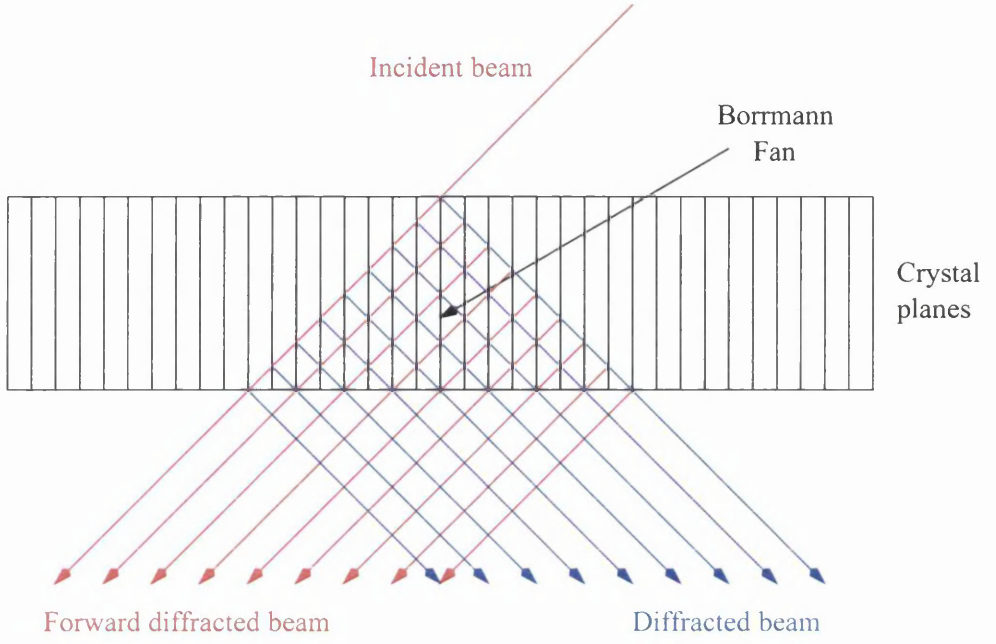

Figure 1.10: The Borrmann fan.

parent in polarised light analyses of the crystal which will be discussed in the next chapter.

The need for the dynamical theory is apparent as a departure from the kinematical regime of assumptions proves necessary when considering scattering from anything other than impractically thin or small crystallites. In other circumstances the scattering is strong and a mechanism for energy transfer can no longer be neglected (hence the term "dynamical"). One must consider the fact that one cannot talk anymore of the incident beam as unmodified by its passage through the crystal medium. When the Bragg conditions are satisfied the orientation of the crystal is such that the diffracted beam itself will be re-diffracted back into the direction of the original incident beam. This is best illustrated by considering the volume of the crystal illuminated by the beam, the Boormann fan, as shown in figure 1.10 . It can be seen that the diffracted intensity results from the scattering of forward diffracted X-rays within this volume. The Borrmann

fan illustrates the need to consider the differential equations, which describe the propagation of the X-rays through the crystal medium prior to and following the interaction, which results in the diffracted intensity, to be coupled. These are derived from Maxwell's equations and incorporate information about the polarisability of the crystal derived from its electric susceptibility. This approach is known as *Takagi-Taupin* theory.

Adopting cgs units for convenience, since this theory is most concisely expressed in cgs units, and assuming the electrical conductivity is zero and the magnetic permeability is unity, the propagation of the X-rays through the crystal medium occurs according to Maxwell's equations

$$\nabla \times \underline{E} = -\frac{1}{c}\frac{\partial \underline{B}}{\partial t} \qquad \nabla \times \underline{H} = \frac{1}{c}\frac{\partial \underline{D}}{\partial t}$$

in which $\underline{E}$ is the electric field, $\underline{B}$ is the magnetic induction, $\underline{D}$ is the electric flux density, $\underline{H}$ is the magnetic field and c is the velocity of light *in vacuo*. Combining these to expressions to eliminate the magnetic terms yields a wave equation in the electric flux density which introduces the effects due to the polarisability of the crystal medium through the electric susceptibility

$$\nabla \times \nabla \times \underline{D} = -\frac{1+\chi}{c}\frac{\partial^2 \underline{D}}{\partial t^2}$$

Momentum is conserved during the scattering process, that is, $\underline{K}_h + \underline{h} = \underline{K}_0$ where $\underline{K}_h$ and $\underline{K}_0$ are the diffracted and forward diffracted wave vectors inside the crystal, however the condition $|\underline{K}_h| = |\underline{K}_0| = 1/\lambda$ is relaxed inside the crystal. It applies only to the incident and diffracted wave vectors outside the crystal, $|\underline{k}_h| = |\underline{k}_0| = 1/\lambda$, in accordance with the Bragg condition.

The Bloch theorem indicates that any solution must exhibit the periodicity of the lattice, therefore

$$\underline{D} = \sum_h \underline{D}_h \exp(-2\pi i \underline{K}_h \cdot \underline{r})$$

Only the diffracted and forward diffracted beams are considered in deriving the two coupled solutions, that is, only $\underline{D}_h$ and $\underline{D}_0$ are considered to be non-zero in the above summation, an approximation taken from the geometry of the Borrmann fan. The periodicity of the lattice is also manifested in the representation of the electric susceptibility of the crystal,

$$\chi(r) = \sum_h \chi_h \exp(-2\pi i \underline{h} \cdot \underline{r})$$

in which χ_h is expressed in terms of the structure factor for the reflection off plane $\underline{h}$, S_h as

$$\chi_h = -\frac{r_e \lambda^2}{\pi V} S_h$$

It should be noted that the refractive index is thus very close to unity and that it is less than unity in contrast to what might be expected at optical wavelengths. The solution of the Maxwell equations inside the crystal taking these considerations into account satisfies

$$\{k^2(1+\chi_0) - \underline{K}_0 \cdot \underline{K}_0\} D_0 + k^2 C \chi_{\bar{h}} D_h = 0$$

$$k^2 C \chi_h D_0 + \{k^2(1+\chi_0) - \underline{K}_h \cdot \underline{K}_h\} D_h = 0$$

where $C = \underline{D}_0 \cdot \underline{D}_h$ is the polarisation factor described above. It is convenient to express these solutions in terms of the deviation parameters for each of the forward diffracted and diffracted wave vectors, defined as

$$\alpha_0 = \frac{1}{2k}\left[\underline{K}_0 \cdot \underline{K}_0 - k^2(1+\chi_0)\right] \qquad \alpha_h = \frac{1}{2k}\left[\underline{K}_h \cdot \underline{K}_h - k^2(1+\chi_0)\right]$$

respectively, which describe the departure of the diffracted and forward diffracted wave vectors from the kinematic assumption that $k_0 = k_h = 1/\lambda$. Substitution into the solution above then yields the range of permissible deviation parameters $\alpha_0 \alpha_h = k^2 C^2 \chi_h \chi_{\bar{h}}$

The ratio of the amplitudes expressed in terms of the deviation parameters will

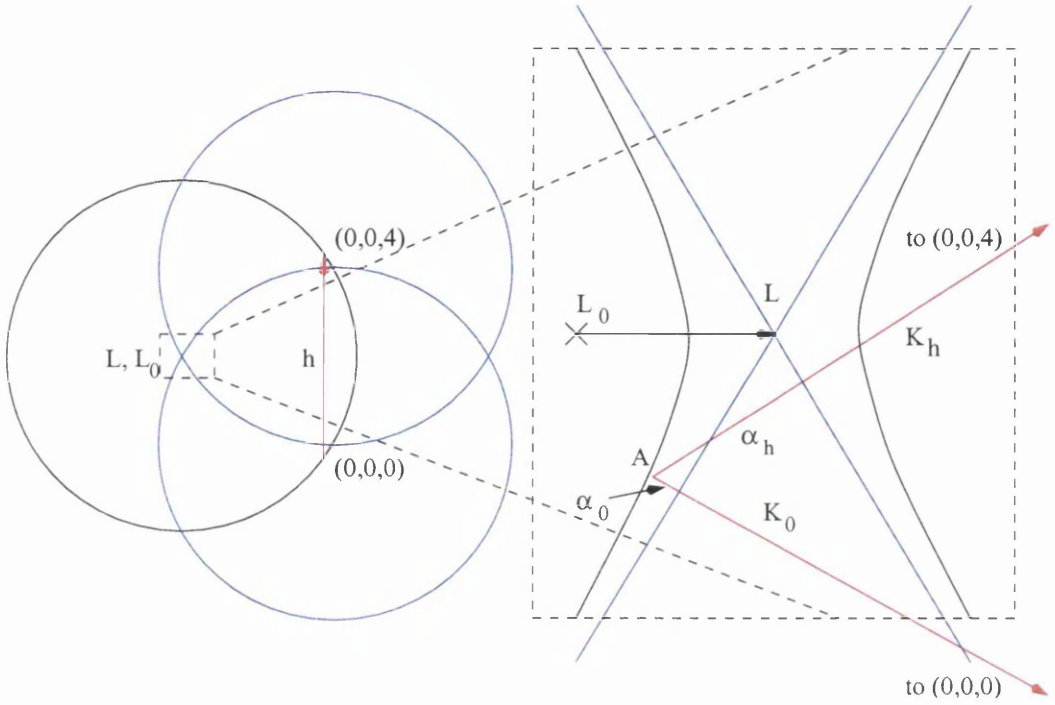

Figure 1.11: Ewald sphere cross-section

give a useful means of deducing the profile of the rocking curve as the scattered intensity is proportional to the square of the diffracted amplitude and the deviation parameters themselves are amenable to a geometric representation in reciprocal lattice space as will be shown. The ratio of diffracted to forward diffracted amplitudes is

$$\frac{D_h}{D_0} = \frac{2\alpha_0}{C\chi_{\bar{h}}k} = \frac{C\chi_h k}{2\alpha_h} \qquad (\frac{D_h}{D_0})^2 = \frac{\alpha_0\chi_h}{\alpha_h\chi_{\bar{h}}}$$

It is seen that the maximum in the diffracted intensity occurs when the deviation parameters are equal.

A graphical representation of the deviation parameters is best achieved in reciprocal lattice space in the Ewald sphere construction shown in figure 1.11. A cross-section of the Ewald sphere construction is shown with two (blue) spheres with centres at either end of the reciprocal lattice vector corresponding to the momentum transfer to the lattice. In the kinematical theory the diffracted and

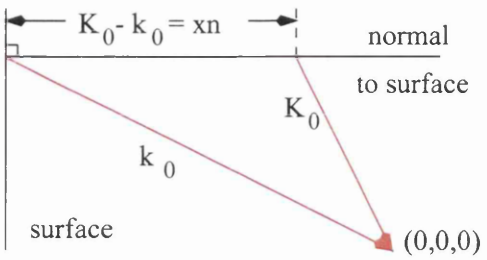

Figure 1.12: X-ray scattering boundary conditions.

forward diffracted wavevectors originate at the intersection of these spheres shown as point L_0, the Laue point. The neighbourhood of L_0 is shown magnified on the right hand side of the diagram, such that the cross-section of the spheres is now approximated using straight lines. The wavevectors inside the crystal connect the centre of the Ewald sphere, L_0, to the points (0,0,0) and (0,0,4), satisfying the Bragg condition.. On the right hand side of the diagram we see this intersection shifted to the Lorentz point L as a result of the refractive correction to the magnitude of these, $(1 + \chi)$. In the dynamical case the locus of points on which the wavevectors inside the crystal originate is no longer the blue lines on the right hand side of the diagram, but the hyperbolae to which these lines are asymptotes. The deviation parameters are then seen to be the length of the lines in reciprocal lattice space connecting the point at which the wavevectors originate, A, to these asymptotes, which are perpendicular to the asymptotes. The shift from L_0 to L is about 1 part in 10^5, justifying the magnification and approximation of the cross-section by straight lines.

The boundary conditions at the surface stipulate that $\underline{K}_0 - \underline{k}_0 = x\underline{n}$, since continuity of the solution of Maxwell's equations at the boundary require the amplitudes and phase velocity parallel to the surface of the crystal to be matched for the solutions inside and outside the crystal, leaving only components normal to the surface. This is illustrated in figure 1.12.

In figure 1.13 the consequences of these boundary conditions are shown. The blue dotted line respresents the cross-section of the Ewald sphere in the Bragg case, and is the locus of Laue points on which the wavevectors outside the crystal, $\underline{k}_0$ and $\underline{k}_h$, originate for different orientations of the diamond. The sphere centred on one end of the reciprocal lattice vector, the point (0,0,4) in figure 1.11, will be rotated round as the point (0,0,4) is rotated about (0,0,0) according to how the diamond is oriented with respect to the beam. The Laue point L_0 traverses this line, which represents the intersection of the spheres centred on (0,0,0) and (0,0,4), as the diamond is rotated. This is shown on the left hand side for the transmission geometry and on the right hand side for the reflection geometry. The geometrical construction of hyperbolae and asymototes representing the locus of points on which the wavevectors $\underline{K}_0$ and $\underline{K}_h$ originate inside the diamond is fixed relative to the diamonds surface, as it is a product of the lattice. The surface of the diamond is represented in green in the figure. The hyperbolae are shown in black. The wavevectors are shown in red. The boundary conditions imply that a line normal to the surface which passes through the Laue point corresponding to the wavevectors outside the diamond will intersect the hyperbolae at the points where the wavevectors inside the diamond originate. These points are termed tie-points. As the orientation of the diamond is changed, such that the Laue point L_0 is swept along the blue dotted lines, it is seen that the tie-points will be swept along the hyperbolae and the deviation parameters varied accordingly.

It is seen that there are two tie-points for a given crystal orientation, meaning that there are two diffracted and two forward-diffracted wavevectors inside the crystal with slightly different wavelengths. The interference between these causes a sinusoidal variation in intensity which reaches its first zero at the extinction distance mentioned above. Also this interference can cause fringing in the topographs of exceptionally fine defect free specimens called Pendellösung. The

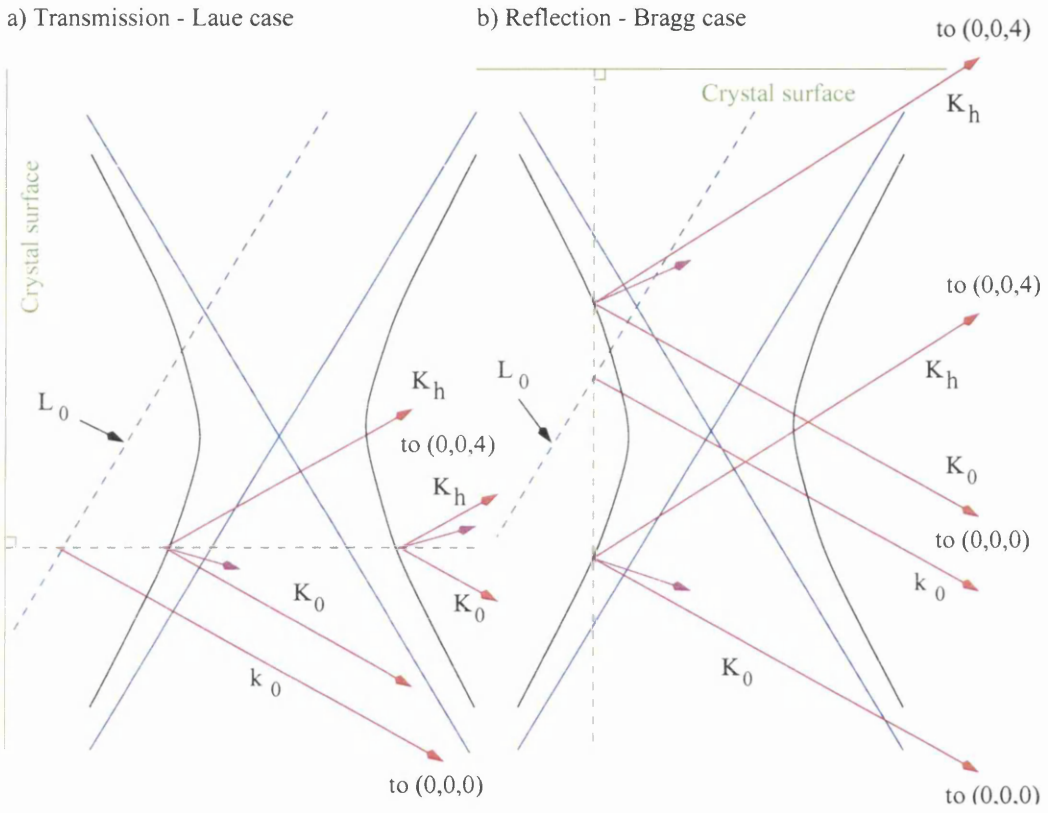

Figure 1.13: Transmission and reflection X-ray diffraction

rocking curve can be obtained by plotting the reflected intensity from the crystal against the crystal angle relative to the incident beam. The transmission rocking curve is found to have a full width at half maximum (FWHM) of

$$\Delta\theta = \frac{2|C|e^2\lambda^2|F_h'|}{\pi V mc^2 sin(2\theta)}$$

where θ is the Bragg angle, V is the volume of the unit cell and F_h' is the structure factor associated with the reciprocal lattice vector of the plane reflecting the X-rays. C is a factor whose value is 1 if the polarisation of the incident wave is perpendicular to the reflection plane, that is, if σ polarisation prevails as has been discussed previously, which was the case in these studies. Departure of the rocking curve profile from the Lorenzian ideal and of the FWHM from this theoretical minimum which results from using a perfect crystal indicate the presence of defects and mosaic structure which may have implications for the suitability of the specimen under scrutiny for use in photonuclear studies and may provide information which helps identify the nature of the defects. Linear defects can be very effectively diagnosed using imaging techniques which use dynamical effects to provide images of the crystal with contrast.

Chapter 2

Experimental Setup & Apparatus

2.1 Introduction

The experimental work comprising this thesis, excluding some diagnostic measurements of the diamond radiators, was performed at the Mainzer Microtron MAMI-B at the Institut fur Kernphysik at the Johannes Gutenberg Universitat, Mainz, Germany. Some x-ray measurements of the properties of the diamond radiators were made at the electron synchrotron at Daresbury, England. Analysis of the strain fields in the diamond radiators was achieved using polarised light analyses performed at Glasgow University.

In Mainz a high quality 100 % duty factor continuous electron beam is delivered with a primary beam energy of 855 MeV. This is incident upon the diamond radiator, and the energies of the photons radiated by the electrons scattered in the radiator are obtained by an analysis of the residual energies of the electrons in the Glasgow tagging spectrometer. If information regarding the angular distribution of the photons is not required the analysis of residual energies is sufficient without the constraint of coincidence, since every degraded photon is associated with a photon. However if information is required concerning the angular distribution of photons emitted from the radiator, that is, not every photon of interest is associated with a degraded electron, then the photons are tagged, their energies deduced from their detection in time coincidence with the degraded electron. This extends to photonuclear experiments in which the reaction products produced at the target upon which the photon beam is incident are measured in coincidence with the degraded electron so that the energy of the photon which was associated with their production can be deduced. Photons must also be tagged if cases of multiple emission of photons from individual electrons are to be discerned.

In the context of this study, information regarding angular distribution of the emitted photons was obtained by restricting which photons were detected using

collimation, which could be offset mechanically using an arrangement of shims. The photons were then detected in a lead glass or NaI detector in coincidence with the degraded electrons. More sophisticated techniques for deriving similar information which are under development as described in chapter 6.

The apparatus pertaining to spectroscopic techniques only employed in this study in the investigation of the effects of radiation damage to diamonds incurred during photonuclear experiments is described in the chapter relating to that aspect of the current study.

2.2 The Mainz Electron Microtron

The use of a continuous beam in photonuclear experiments allows a higher ratio of real to random coincidences to be obtained than would be possible using a pulsed beam of the same average current. MAMI-B was developed to provide a facility which offered this with beam energies up to 1 GeV. Experiments with tagged photons have enjoyed a revival in the last two decades as a result of the provision of such facilities.

MAMI-B delivers a 100 % duty factor electron beam with a primary beam energy of 855 MeV, a resolution of 60 keV and a beam emittance of less than 0.04π mm.mrad. The 100 % duty factor confers the advantage of highest real to random coincidence ratio for a given beam current [20, 21]. Although the tagged photon technique was originally proposed earlier, exploitation was prevented until the 1980's because of the poor real to random ratios which would have resulted from the pulsed machines available up to that point, which had duty factors $\leq 0.1\%$.

The Mainzer Microtron, MAMI-B, employs three stages to accelerate electrons to the energy of the beam before transport in to the experimental hall by means of

steering dipole and focusing quadrupole magnets. A 100 keV gun injects electrons into a linear accelerator (LINAC) which boosts their energy to 3.5 MeV. The beam is then injected into the first of the three stages. In the first stage the electrons are circulated 18 times, attaining an energy of 14 MeV, in the second stage 51 turns bring the energy to 180 MeV before the final 90 turn microtron produces a 855 MeV beam.

A plan of the MAMI-B facility is shown in figure 2.1. In each leg of each stage the electrons are accelerated in a LINAC by a radio frequency electric field before being recirculated back through a return pipe into the LINAC by bending magnets at either end. Each circulation uses a different return pipe due to the increasing radial trajectory of the beam. This is illustrated in figure 2.2. These legs through the LINAC give the beam a small amount of additional energy which cumulatively result in the energy of the beam delivered to the experimental hall, the beam gaining 0.6 MeV per circulation in the first stage, 3.24 MeV in the second and 7.5 MeV in the third. The time required for each circuit of the beam differs by an integer number of periods of the accelerating field, ensuring that the electrons arrive back at the LINAC in phase. It is due to the small energy gain at each pass of the electrons that the power requirements of the accelerating cavity are low enough for it to be operated in continuous wave mode.

The radio frequency electric fields are driven by phase locked klystron oscillators, which do impose microstructure on the beam, but the frequency (2.45 GHz) allows us to consider the beam to be essentially continuous. The maximum beam intensity is around 100μA but, due to restrictions imposed by the count rates the spectrometer can tolerate, the microtron is operated at around 20 nA in conjunction with the spectrometer. This is limited by the maximum rate a spectrometer channel can handle, which is around 1 MHz. The low emittance of the beam, which is among the best currently available, is favourable to coherent

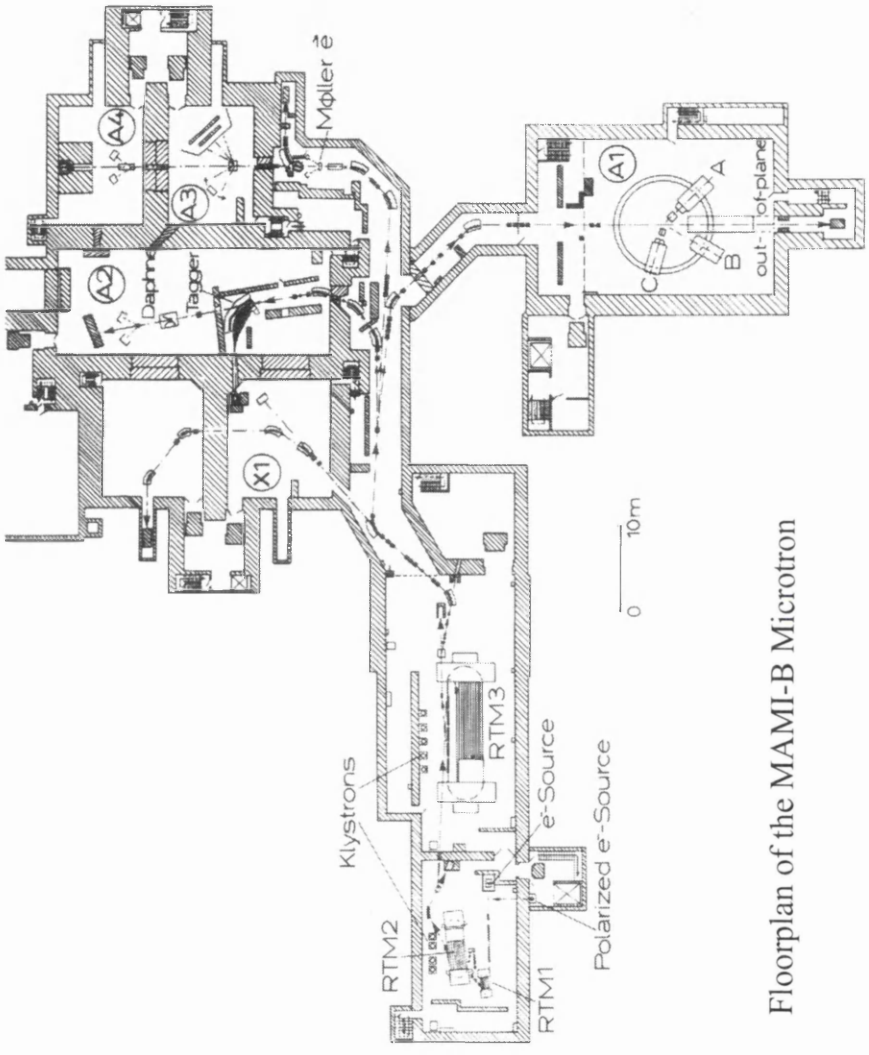

Figure 2.1: MAMI-B, with the A2 experimental hall, where this study was conducted clearly shown.

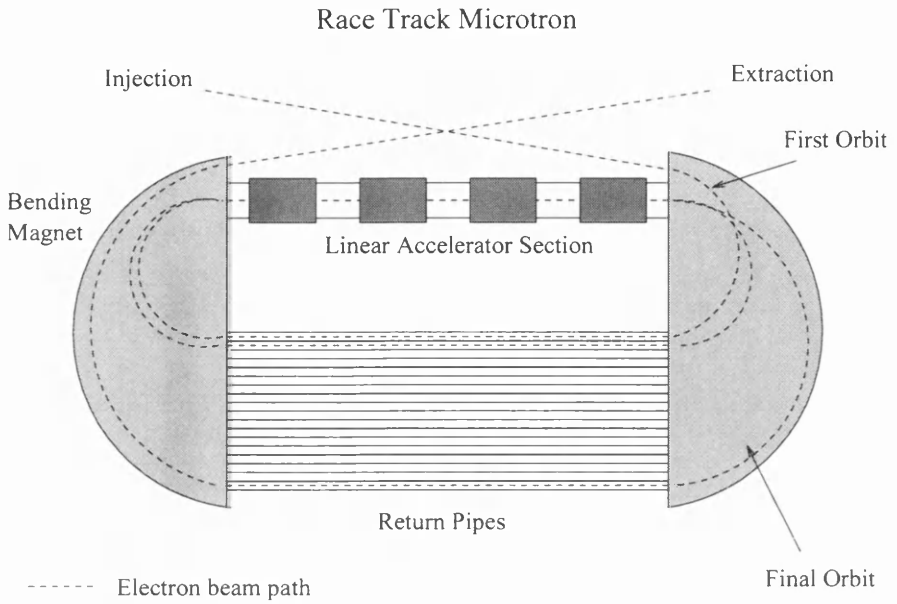

Figure 2.2: Schematic diagram of a racetrack microtron.

bremsstrahlung. The beam also exhibits high stability.

2.3 The Glasgow Tagging Spectrometer

The electron beam is scattered coherently in the regular lattice structure of the diamond radiator, inducing bremsstrahlung, and the energy of the emitted photons is deduced by detecting them or the products of reactions in which they have participated in coincidence with the degraded electron, whose energy is analysed in the spectrometer. The energy of the photon can be deduced to be

$$E_\gamma = E_e - E_{e'} \tag{2.1}$$

E_e is the primary beam energy and $E_{e'}$ is found using the Glasgow Tagging Spectrometer or Tagger [22, 23]. The electron beam passes from the radiator into a large magnetic dipole which maintains a constant and homogeneous field which focuses the scattered electrons onto an array of 353 scintillators which lie on the

4.5 m focal plane. These are fitted with photomultiplier tubes whose outputs are read by dual threshold discriminators which generate logic pulses from which timing information can be derived with a resolution of $\leq$ 1 ns. The scintillators are arranged perpendicular to the electron trajectories such that they overlap, so that a real electron will pass through two scintillator elements. This helps to suppress the effect of random background counts in individual elements. Thus there are 352 channels, each with an average energy resolution 2 MeV, in the focal plane, covering an energy range from 40 MeV to 790 MeV. This represents a large momentum acceptance, with p_{max} to p_{min} approximately 16 to 1, allowing 88% of the energy range to be tagged. The intrinsic resolution of the spectrometer of 0.5% is around 120 keV. The Tagger is illustrated in figure 2.3.

A small quadrupole provides additional focusing prior to the main dipole. The photon beam can be collimated, at the point where the photon beam leaves the spectrometer in figure 2.3, to enhance the polarisation of the photon beam produced by coherent bremsstrahlung. Collimation enhances the polarisation because the incoherent background is emitted into a larger solid angle than the coherent component. Sweeping magnets down beam from the collimation remove any stray charged particles from the photon beam which may have been produced in the collimators.

Each channel of the spectrometer is limited to a count rate of around 1 MHz due to the danger of burnout of the photomultiplier tubes. This limits the beam current into the spectrometer. However, sections of the tagger focal plane detector array that correspond to low photon energy (i.e. high residual electron energy) can be switched off, allowing a higher current to be used, as the photon flux is higher at lower energies. This is particularly useful if high energy features of a phenomenon such as channeling radiation are being investigated.

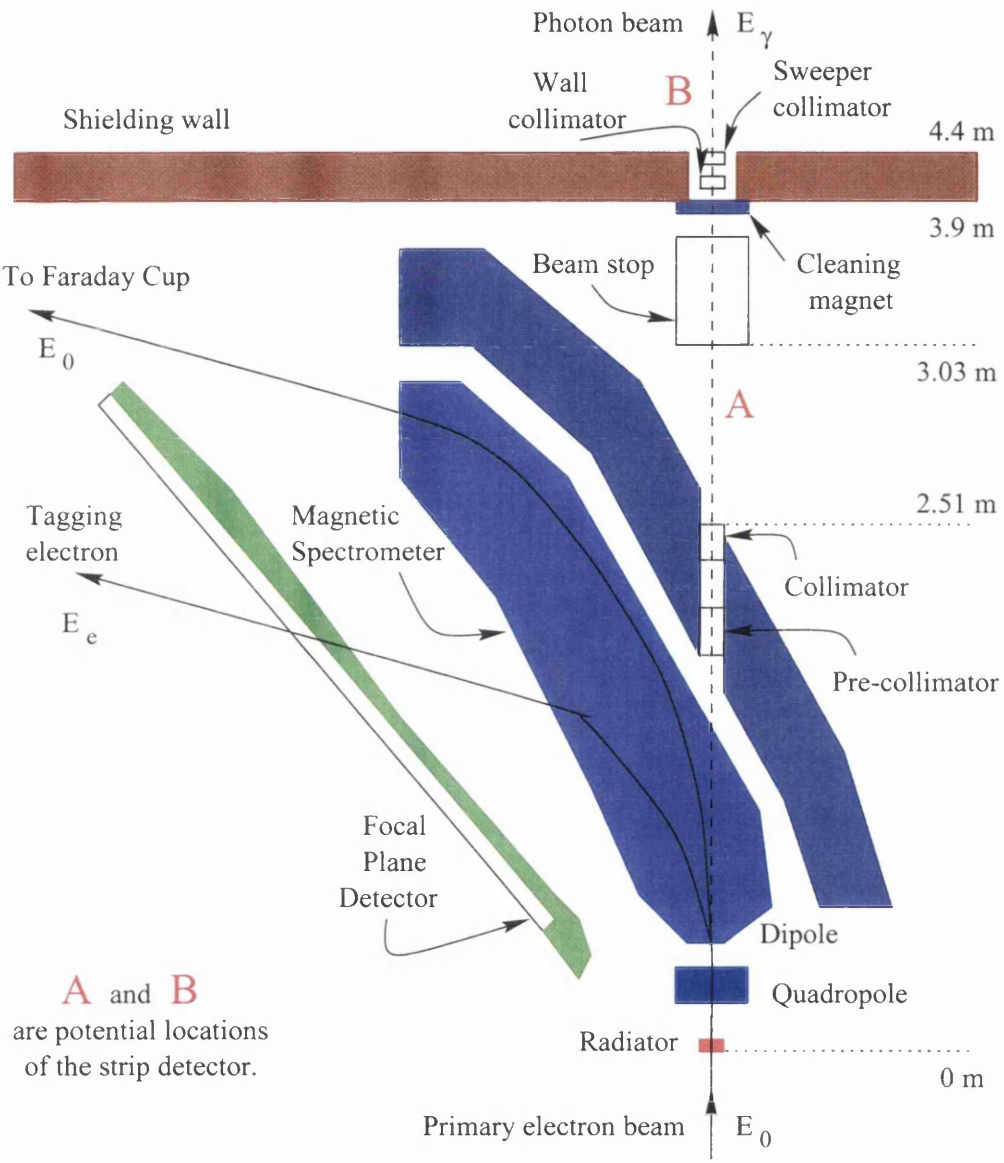

Figure 2.3: Glasgow tagging spectrometer

2.4 Controlling the Diamond

The electrons are scattered off a radiator, in this case a diamond single crystal, which is held in the beam and oriented with respect to it by a goniometer which can rotate the sample around three mutually orthogonal axes and move the crystal along two translational axes perpendicular to the beam. The rotations and translations of the crystal are driven by stepper motors whose step size impose the angular resolution of crystal orientation with respect to the three rotational axes. The goniometer is shown in figure 2.4. It should be noted that the rotational axes are nested, with the mechanism that effects azimuthal rotations mounted upon that which performs rotations around a horizontal axis, which in turn lies on the mechanism that performs rotations around a vertical axis.

These rotations allow the crystal to be aligned with a given axis parallel with the beam, or with a given reciprocal lattice vector located in a specific momentum pancake as described in the exposition of coherent bremsstrahlung.

Rotations can be performed incrementally, allowing the coherent bremsstrahlung spectrum to be plotted for a range of crystal angles, as seen in figure 2.5. With each step the angle between the crystal and the beam is incremented by the step size. This process is referred to as a scan, and can be performed on any of the axes. The resolution of the scans is limited by the smallest step size available, which can be found in table 2.1 for each of the axes [24]. Channeling phenomena can be investigated by scanning on the horizontal axis H or vertical axis V near the zero position, at which the crystal axis of interest is aligned parallel with the beam. A description of how these zero positions are obtained is given later in this section. The crystal can be aligned at or near the channeling regime described by Lindhard's critical angle for channeling, Ψ_L.

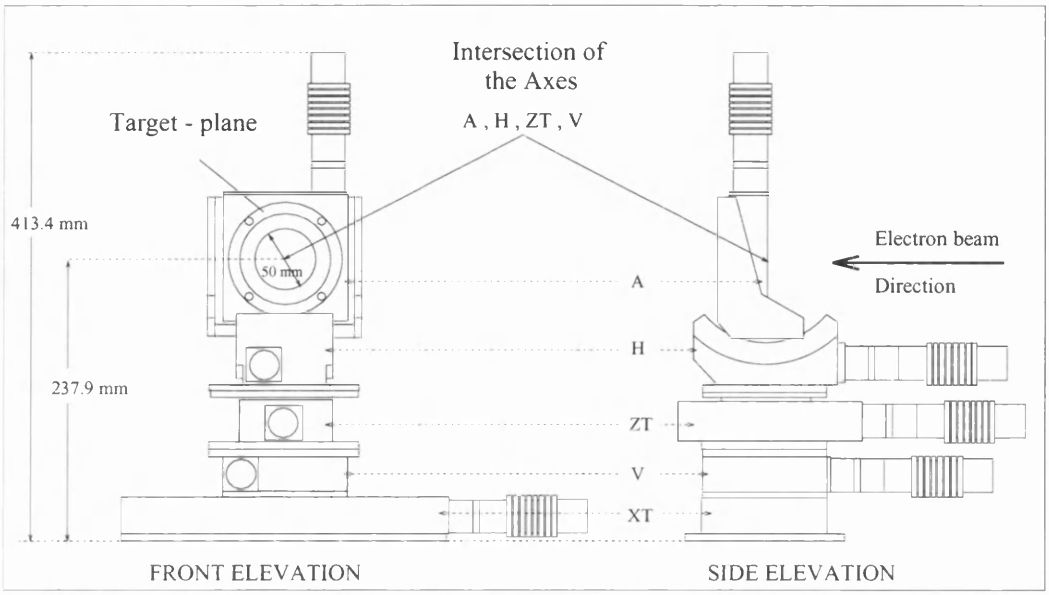

Figure 2.4: The goniometer on which radiators are mounted in the electron beam.

Axis	*Range*	*Precision*
A	360°	0.01°
H	±10°	0.001°
ZT	$\pm 2mm$	0.0001 mm
V	±10°	0.001°
XT	150 mm	0.001 mm

Table 2.1: Properties of the drives controlling the goniometer's five degrees of freedom. 1° = 17 mrad.

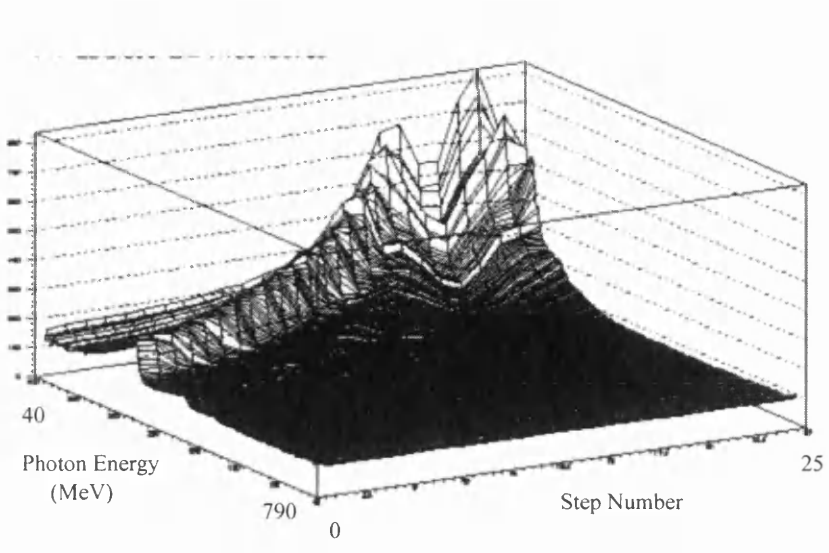

Figure 2.5: A scan through the zero position. The step size is 0.5 mrad.

2.4.1 Mounting the Diamond

The radiators are mounted on a wheel which is then mounted onto the goniometer. The crystal radiator is placed in the middle of the wheel so as to ensure it lies at the intersection of the three rotational axes. Movements along the translational axes can ensure that this intersection lies on the beamline. Amorphous radiators can be located at one of three sites around the edge of the wheel and brought into the beam by translational movements, as the orientation of these radiators with respect to the rotational axes does not affect the resultant incoherent bremsstrahlung spectrum, other than perhaps a rise in overall intensity due to the oblique angle of the beam relative to the radiator causing the beam to pass through a greater thickness of radiator. The wheel is illustrated in figure 2.6, viewed from downbeam of the wheel. It is seen that the diamond is mounted in the middle at the intersection of the goniometer's rotational axes to allow orientational effects to investigated and exploited.

The crystal is mounted onto a frame which is then attached to the centre of the wheel. The diamonds are mounted onto mounting wires, typically gold or

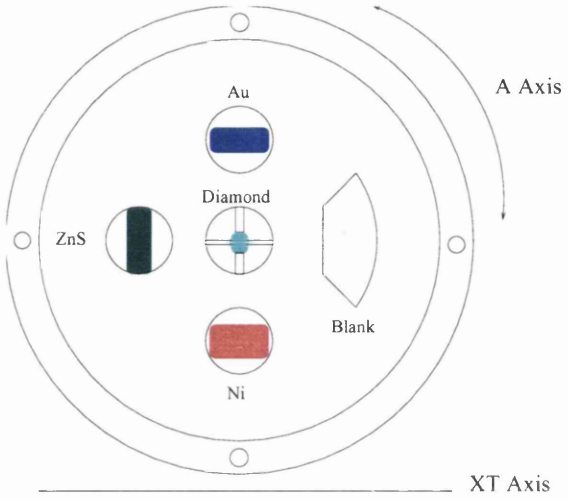

Figure 2.6: The goniometer wheel.

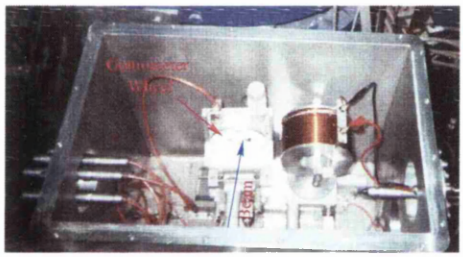

Figure 2.7: The goniometer is housed inside a vacuum chamber.

gold-tungsten alloy, roughly 20μm thick, using an acetone soluble adhesive . A picture of the goniometer *in situ* is shown in figure 2.7. The beam is represented in figure 2.7 by a blue arrow.

2.4.2 Aligning the Diamond

The diamond orientation was a two stage process. The first stage acquires the orientational offsets to be input into the orientational routine, and the second oriented the diamond so as to place the desired reciprocal lattice vector in a momentum pancake corresponding to the emission of photons of the desired energy

and polarisation.

When the diamond was placed in the beamline it was initially misaligned, that is, the angle between the crystal axis and the beam was non-zero, even with the goniometer angles set to zero. It was necessary to find the offsets to apply to the goniometer angles such that when they were set to zero the axis was aligned with the beam. The mounting of the crystal in the beam is shown schematically in figure 2.8 to illustrate the offsets and the angles whose variation manipulated the orientation of the crystal. The diamond is shown in pink in the centre, mounted on a green plate which can perform the azimuthal rotations ϕ_a. On the diamond in white are seen the traces of the main crystal planes perpendicular to the surface of the diamond, the (004), (040) and (022) planes. The directions of the axes $< 100 >$, $< 010 >$ and $< 001 >$, which are fixed in the crystal, are shown, and the misalignment of the $< 100 >$ axis relative to the beam direction can be seen. The azimuthal rotation is is nested within a blue plate which performs horizontal rotations ϕ_h which is itself nested within a yellow plate which can be rotated about the vertical by ϕ_v. The maximum tilt of the crystal from the plane of the azimuthal rotation plate, ϕ_{tilt_m}, occurs at an azimuthal offset of ϕ_{tilt_a} and the main crystal plane in consideration, in this case the 001 family, has an azimuthal offset from the goniometer zero position of ϕ_a^0. The horizontal and vertical offsets of the beam in relation to the goniometer zero position are $\phi^0_{beam_h}$ and $\phi^0_{beam_v}$ and the offsets of the [100] crystal axis direction in relation to the beam are ϕ_h^0 and ϕ_v^0.

These offsets can be found by employing a procedure which generates what are termed Stonehenge plots [25]. A Stonehenge plot is shown in figure 2.9. A quasi-azimuthal scan is performed, that is, the horizontal and vertical angles are varied according to

$$\phi_h = \phi_h^0 \pm \phi_{inc} \cos \phi_q$$

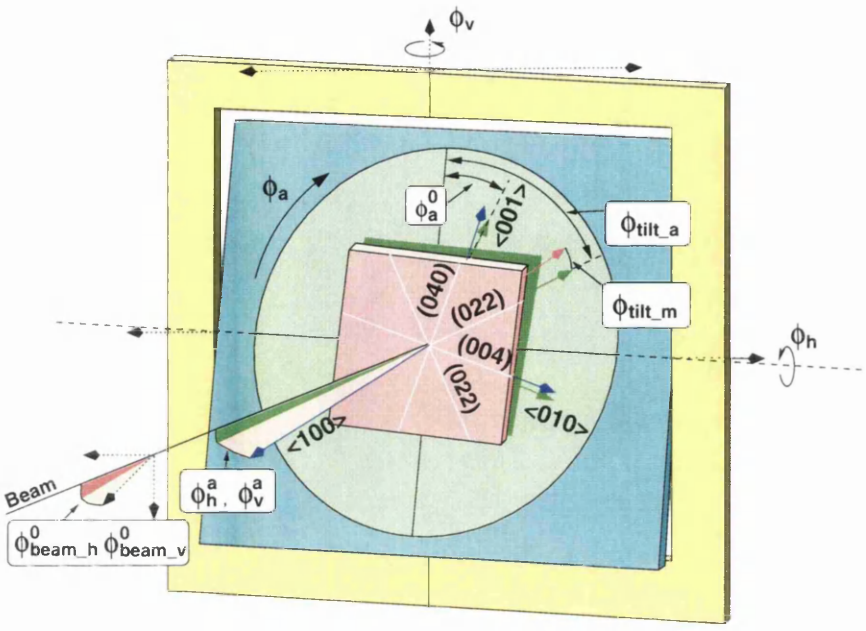

Figure 2.8: Diamond mounting schematic.

$$\phi_v = \phi_v^0 \pm \phi_{inc} \sin \phi_q$$

where $0 \leq \phi_q \leq 2\pi$ and ϕ_q is defined to be the quasi-azimuthal angle. The intensity of the bremsstrahlung above a set threshold is plotted on the points in ϕ_h, ϕ_v-space traversed. ϕ_q can be interpreted as the azimuthal angle about which the projection of the crystal axis onto the plane normal to the beam is rotated as ϕ_h and ϕ_v are varied according to the scheme above.

The symmetry of the lattice is exploited to generate a template which represents the location of the crystal planes in ϕ_h, ϕ_v-space. Maximum intensity will occur as the beam crosses these, so fitting this template to the plot and inspecting the distance between the origin of the plot and the origin of the template yields the offsets. Once the offsets are found these are installed in the code routine that alters the goniometer angle setting so that the goniometer angles can be considered the angles between the beam and the diamond.

The second stage of diamond alignment is to orient the diamond such that a

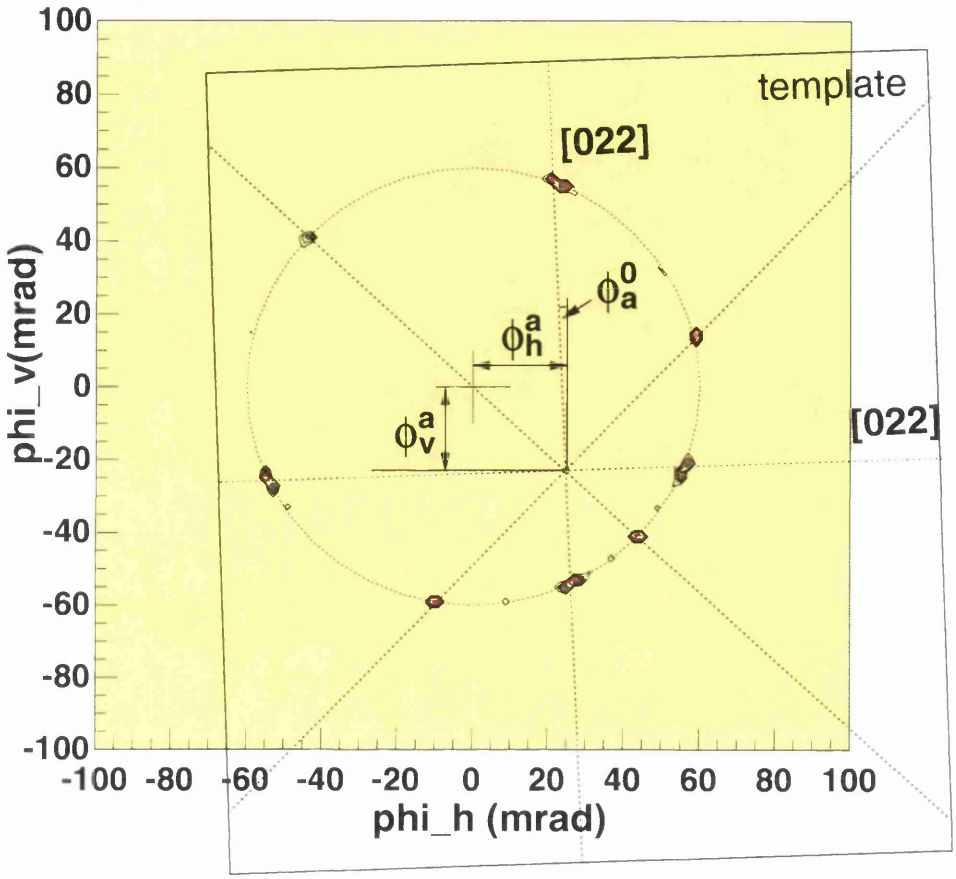

Figure 2.9: A Stonehenge plot.

momentum pancake corresponding to a specified photon energy is selected by a reciprocal lattice vector. This is shown in figure 2.10.

The energy of this peak can be tuned by varying the orientation of the crystal [26]. When the crystal is aligned and in the zero position the beam is normal to its surface, as is shown in a) and b). (a) is the view facing the beam, (b) facing the horizontal axis. The azimuthal angle about the beam has been set at $\frac{\pi}{4}$. The momentum pancake is indicated. (c) and (d) show a rotation about the horizontal axis from above and the side, followed by a rotation about the vertical axis in (e) to bring a reciprocal lattice point within the momentum pancake.

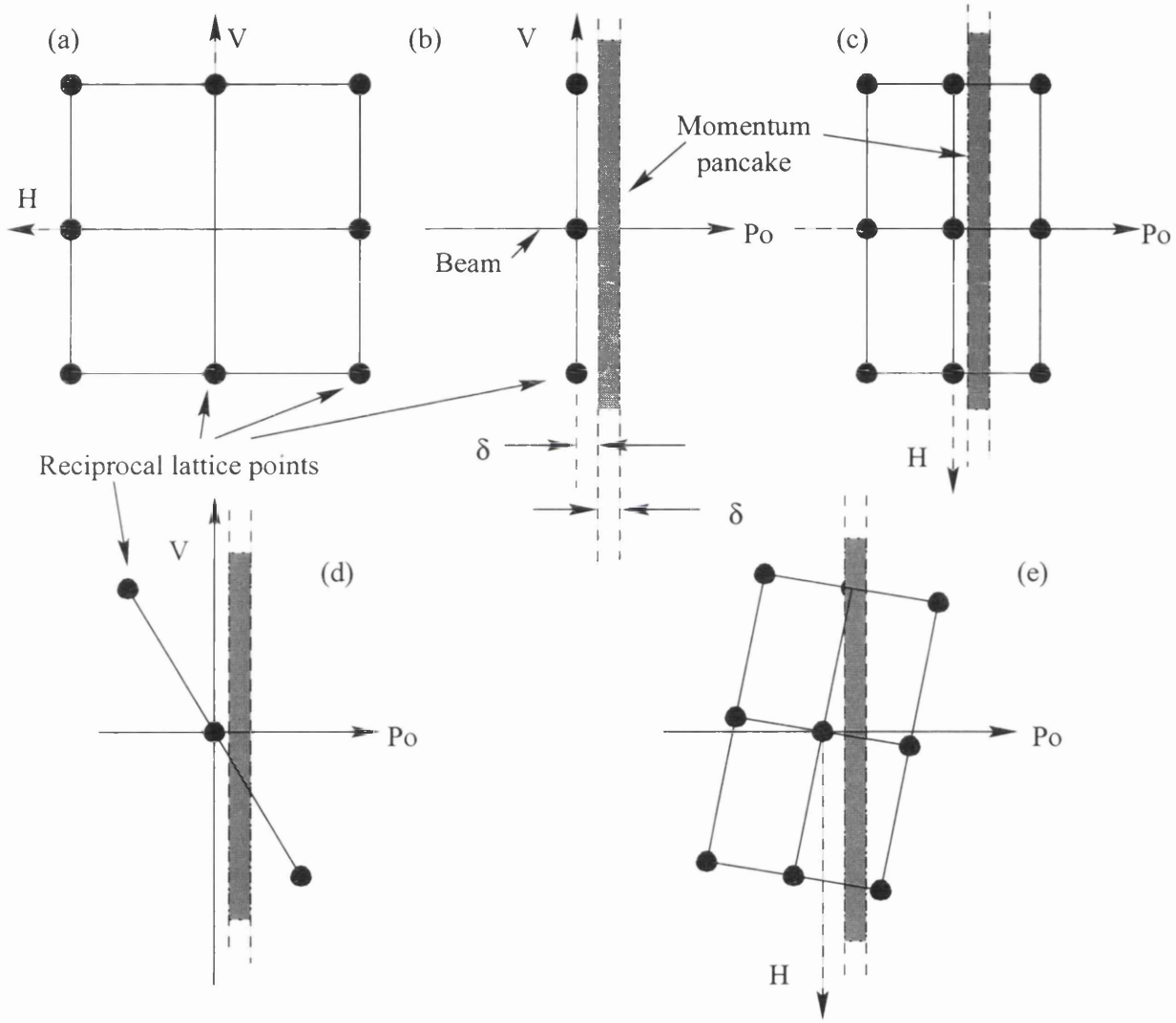

Figure 2.10: The orientation of the reciprocal lattice.

2.5 X-ray Sources

A survey of the defects inherent in the crystal radiators used to induce coherent bremsstrahlung and channeling was seen to be useful, both from the point of view of selecting suitable defect-free specimens for investigating the radiation and also to examine any relationship between the nature of the defects and spectral features in the radiation. The widths of X-ray diffraction peaks, or rocking curves, were measured using a double crystal diffractometer. X-ray topographs of the radiators were also taken which revealed vividly the extent of line defects in the samples. The Synchrotron Radiation Source or SRS at C.C.L.R.C. Daresbury, England, provided a source of X-rays for these diamond diagnostic measurements.

2.5.1 The Daresbury Electron Synchrotron

A white X-ray beam was delivered by an electron storage ring to the experimental station at which the topography was performed. The 2 GeV electrons emit synchrotron radiation as their trajectories are bent in the bending magnets that form the 16 cell FODO lattice of the storage ring. A FODO cell contains a FOcussing and a De-fOcussing quadrupole element. The electrons are injected from a booster ring which is itself filled from a LINAC. The field strength in the dipole bending magnet is 1.2 T, making the bend radius 5.6 m. The overall circumference of the machine is 96 m. The electron beam is bunched and operates in one of two modes, single bunch or multibunch mode. The number of available bunches for circulating electrons is 160, only one of which is occupied with electrons during single bunch mode. Most are filled during multibunch running, with a gap left in the fill structure to minimise beam effects that degrade the properties of

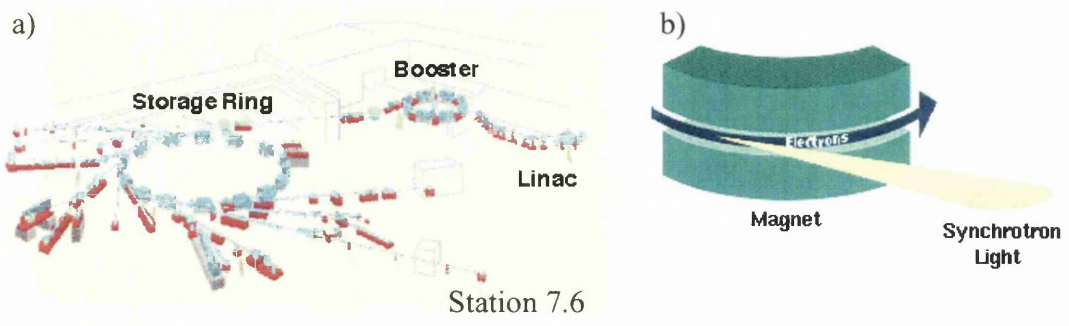

Figure 2.11:

the source. Single bunch mode is useful as a source of pulsed synchrotron light for time-resolved measurements, however multibunch mode provides the greatest intensity and the best source properties. Typical beam current in multibunch mode is between 100 mA and 200 mA. A current of 200 mA gives a photon flux at station 7.6 of 0.67 $\times 10^9$ photons mm^{-2} sec^{-1} within a 0.1 % band-pass of the energy range, centred at 10 keV . The degree of linear polarisation at 10 keV is 0.96.

There are also insertion devices such as multipole wigglers and undulators in some of the straight sections between bending dipole magnets, but none of these were sources of light for the dedicated X-ray topography station used to perform these measurements. This beam is conveyed to station 7.6 along a 76 m vacuum pipe. The large distance from the dipole to the station allows exceptional image resolution to be achieved, since this allows collimation to minimise the beam divergence. The layout of these components relative to each other is shown in figure 2.11. a) shows the location of station 7.6 at the end of a very long beamline allowing excellent resolution. b) shows the ellipse of synchrotron radiation produced at the bending magnet.

The time structure of the beam is determined by its bunched nature. The 160 available bunches of a length of typically 70 ps are separated by 2 ns, and have a

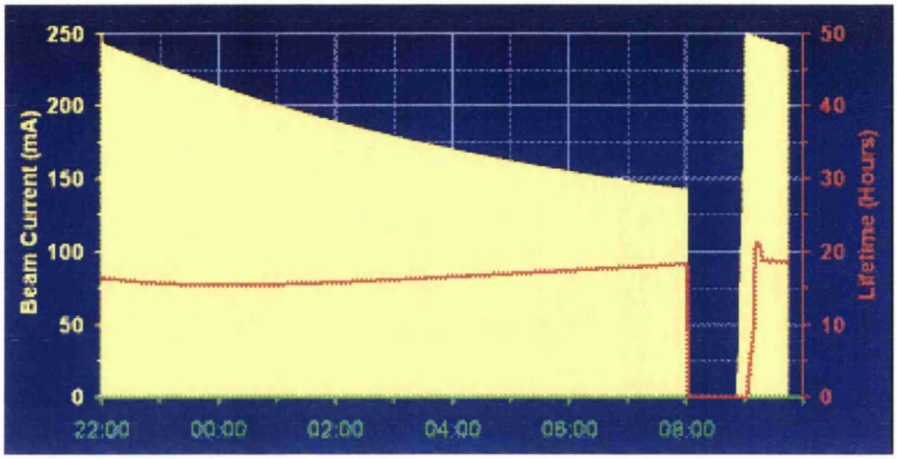

Figure 2.12: A typical decay of the current in the storage ring, followed by a refill.

revolution time of 320 ns. The charge in each bunch varies slightly, such that the pulsed time structure is dominated by the revolution frequency of 3.123 MHz. This is the frequency of the light pulses in single bunch mode. In single bunch mode there is typically some residual charge in the other bunches, usually 10^{-4} less than in the main bunch. The beam current itself decays from its initial peak prior to a beam dump and refill. This takes between 7 and 20 hours. An example of this is shown in figure 2.12. As the timescales of both the beam microstructure and the current decay differ widely from that which characterises the measurements taken, which usually lasted a few minutes, the beam was considered to be essentially stable.

2.5.2 Experimental Station 7.6

Station 7.6 is an experimental station located at the end of an 76m long beamline. The beam is received in a large open and versatile experimental hutch which contains an optical bench and a double crystal diffractometer. This consists of a double arm goniometer with a detector arm for orienting an X-ray detector

relative to the sample being investigated, which is shown in 2.13. It had 4 rotational axes, none of them nested. The beam is shown as a blue line, delivered first to the monochromator, a silicon wafer which selects by Bragg reflection a single wavelength of X-ray. The angle at which this monochromator is oriented is adjusted by rotating it about fineax1, labelled in red on the diagram. This is adjusted to the Bragg angle of the desired wavelength of X-ray, for example a Bragg angle of $\theta_B = 28°.3513$ gives a wavelength of 1Åreflected from the {333} family of planes in silicon. The arm of the diffractometer, again labelled in red, has a goniometer located at either end, one which performed rotations about fineax1 and one which performs rotations about fineax2, labelled in red. With the arm swung up to a position inclined at twice the Bragg angle to the beam, as shown in the diagram, the reflected X-rays shown in blue are delivered to a sample attached to fineax2. A detector arm labelled in red can be used to move an X-ray detector to a position where it can detect the X-rays reflected from the sample.

Placing the sample in the position of the monochromator on fineax1, and a photographic plate on fineax2, allows one to acquire images of the sample using the X-rays reflected from it. These are projection topographs. If illumination of the sample by a single wavelength is desired, it can be mounted on fineax2, a monochromator mounted on fineax1, and the photographic apparatus mounted on the detector arm. This is double crystal topography, so called due to the use of both a crystal sample and a crystal monochromator to provide monochromatic illumination of the sample. With a NaI scintillation detector mounted on the detector arm it was possible to vary the orientation of the sample on fineax2 and observe the variation of the reflected intensity at different orientations, allowing a rocking curve, or plot of this variation with angle, to be obtained.

The beam is collimated using four motorised jaw slits, or shutters, which can also

be adjusted to scan the collimated beam across the sample. Alternatively the sample can be moved across the beam using micrometer screws in the goniometer head in which it is mounted.

When taking a rocking curve the NaI detector which was used saturated at 50,000 counts per second. When sampling a part of the crystal the X-ray flux was reduced by having the shutters closed down to restrict the area of the sample exposed to the beam. However when conducting full crystal rocking curve measurements, that is, when necessarily illuminating the entire sample, aluminium plating can be placed over the window of the detector to attenuate the reflected intensity sufficiently to avoid saturation. Attenuation is generally applied so as to obtain the best possible statistics without incurring saturation.

A laser was in a position to shine a beam down the beamline, aligned with the X-ray beam. This was then used initially to set up the samples and monochromator such that the laser beam was normal to them by observing the laser beam's reflection from their surface. Subsequent to this the elements of the experiment could be rotated into position.

When initially finding the correct orientation of the specimen at which the X-ray reflection occurs in the double crystal geometry, its orientation on fineax2 is scanned through a broad range and an audio threshold on the ratemeter to which the NaI detector is connected is set to give an audible signal when the reflection is traversed. The range through which fineax1 and fineax2 can be scanned is $\pm$10000 arcseconds.

The diamond wafers were attached to mounts which could then be fixed onto the goniometer. A variety of diamonds were already available on mounts, while others needed to be mounted for the first time. Of the existing mounts, not all were compatible with the goniometer at Daresbury and so an adaptor was constructed to allow these to be installed. Similarly the mounting wheel for mounting in

Figure 2.13: The double crystal diffractometer used at station 7.6.

Mainz was modified to take variously mounted diamond specimens.

Preliminary topographic surveys were conducted using D2 or D4 X-ray photographic film, with higher resolution obtained by using Ilford Nuclear emulsion plates.

Section topographs could be obtained by inserting narrow micrometer-controlled slits into the beam in any of the geometrical arrangements described above.

Chapter 3

The Characterisation and Selection of Diamond Radiators

3.1 Introduction

It is important to have some understanding of the quality of the diamond radiators themselves as this will impose its own set of limitations on accuracy in photonuclear experiments in which they are used. An uncertainty in the direction of a reciprocal lattice vector will broaden the angular distribution of the photon emission constituting a channeling peak or degrade a coherent bremsstrahlung energy peak edge. Given that it is important in the context of this study to resolve features in the angular distribution of channeling radiation, a battery of techniques have been employed in ascertaining the nature and extent of imperfections in the specimens used. The aim of the study has been to find to what extent the result of tests deployed to ascertain diamond quality correlate with the performance of diamonds in the context of coherent bremsstrahlung experiments, such that this correlation can be used as the basis for selecting suitable specimens without incurring the expense of beamtime at a coherent bremsstrahlung facility. The technique which incurs the least expense while yielding results highly correlated with diamond performance in coherent bremsstrahlung experiments is the technique of the greatest practical utility.

When using diamonds in photonuclear studies as radiators, there are three possible causes for a distribution of orientations of the beam in relation to the crystal axes to occur, thereby degrading the coherent spectrum obtained. Firstly there is the divergence of the primary electron beam itself. Then the effect of multiple scattering in the diamond must be considered. Finally the variation of lattice parameters in the diamond itself imparts a spread of orientations. All three effects can be considered in comparison to the characteristic opening angle of coherent bremsstrahlung, which can be seen as a maximum permissible limit to each. The amelioration of the first is outwith the scope of this study. The second cause of

degradation can be limited by using radiators as thin as possible. The third is addressed by selecting specimens with the most suitable properties. A further point of comparison is the characteristic angle for channeling, and the properties of the radiator will determine how rapidly de-channeling occurs as the electrons penetrate the crystal. An important point to note is that collimation can improve matters from the perspective of the first two causes, however, no improvement can thus be obtained in relation to the third cause. Collimation will help alleviate the effects of a distribution of electron trajectories, whether it is caused by beam divergence or multiple scattering, but cannot address problems arising from a distribution of crystal orientations.

This survey aims to identify selection criteria for choosing diamonds to use in coherent bremsstrahlung experiments. Electrons are scattered off the diamonds, giving a peaked spectrum superimposed on the incoherent background. The coherent plots displayed in this chapter have had the incoherent background divided out. This can be achieved by dividing the spectrum with an incoherent spectrum exhibiting no coherent peaks acquired by scattering the electron beam off an amorphous radiator or a very misaligned crystal. In the case of this study an amorphous nickel radiator was used.

Since these diamonds are intended for use in coherent bremsstrahlung experiments, the angle which characterises coherent bremsstrahlung forms the basis for comparison with other phenomena arising due to the attributes of diamonds investigated in this study. Photons produced due to coherent bremsstrahlung are emitted mainly into a cone of solid angle

$$\theta_{char} = \frac{m_e c^2}{E_0}$$

m_e being the electron rest mass and E_0 the primary electron beam energy. Coherent radiation is directed into this cone to a greater degree than the incoherent

emission and so the ratio of I_{coh}/I_{incoh} is improved by applying collimation. A distribution of the orientation of a lattice vector due to imperfections in the diamond will, however, cause contributions to the forward directed emission that cannot be corrected for by applying collimation. Multiple scattering causes a spread of electron trajectories that degrades the spectrum and the angle which characterises this is

$$\theta_{scat} = \frac{21.2}{E_0}\sqrt{t} \Rightarrow \frac{\theta_{scat}}{\theta_{char}} = \frac{21.2}{m_e c^2}\sqrt{t}$$

such that the ratio is independent of the primary beam energy and depends only on the crystal thickness, t, in radiation lengths. The radiator should be less than 10^{-4} radiation lengths thick, and the radiation length for diamond is $\sim$ 0.15m. A sample of 10^{-4} radiation lengths in thickness was among those studied.

In this chapter a brief summary of the properties of diamond and its defects is given, followed by a list of the specimens of diamond selected for study. Then the battery of tests applied to these specimens is described and the results presented. Finally conclusions relating to the selection of specimens suitable for use in the production of coherent bremsstrahlung are drawn.

3.2 Diamond and its defects

Diamond consists of carbon with a face centred cubic crystalline structure determined by its tetravalence, each atom forming four strong covalent bonds with its four nearest neighbours. The lattice constant is 3.567Å. The nearest neighbour distance is 1.54Å. There are 1.54×10^{22} atoms per cm^3. The lattice structure has the form of two face centred cubic lattices with one displaced to $(\frac{1}{4}, \frac{1}{4}, \frac{1}{4})$ with respect to the other, which results in a structure factor which favours reflections from planes parallel to the (220) and (400) planes, in that they are enhanced with respect to reflections from other planes. This enhancement is due to the Thomson

scattering of X-rays from the individual atoms in the unit cell adding in phase when these reflections are used. Other reflections are weaker as a combination of destructive and constructive interference occurs.

Diamond has a density of 3.516 g cm^{-3} and a cohesive energy of 7.37 eV/atom. It has the highest bulk modulus of any element, 4.43×10^{11} N/m^2, with the correspondingly lowest compressibility of 2.26×10^{10} m^2/N. The atomic radius of carbon when forming tetrahedral covalent bonds is 0.77Å. The Debye temperature of diamond is 2230 K, which implies that only relatively long wavelength phonon excitations are occupied at room temperature [27]. The thermal conductivity is 1.29 W cm^{-1} K^{-1} at 300 K. The chief impurity is nitrogen, which can occur in concentrations of 1 part in 1000. Trace impurities include transition metals, particularly if they have been used as a catalyst in diamond synthesis.

3.2.1 Diamond Classification

Diamonds are broadly categorised into two classifications, type I and type II. Type I have a relatively high nitrogen content and are formed under conditions of high pressure and temperature in the Earth's mantle or in a synthetic diamond press. Type II diamonds have been naturally or artificially metamorphosed in the geological sense of the term. This serves to reduce the nitrogen content markedly. However, distortions and plastic deformation of the diamonds that occur during their transition to a type II status often causes braided strain structures, bundles of intertwined line defects apparent in polarised light images of the samples, which are seen to dominate their behaviour as radiators for coherent bremsstrahlung. Prior to this study it was assumed that the lower nitrogen content of type II diamonds would be favourable, however it has been found that the strain incurred renders the benefits of the lowered nitrogen content negligible.

Diamonds may be further classified according to the form the nitrogen impurity in them takes. In a type Ia diamond the nitrogen is aggregated, and the most common centre can give a further classification, type IaA containing mostly A centres, which consist of two nitrogen atoms, and, type IaB containing mostly B centres, which consist of four nitrogen atoms, while type IaAB contains both. In type Ib diamonds the nitrogen impurities occur as single unaggregated atoms. Diamonds grow in conditions in which diamond is the stable, energetically favoured form of crystalline carbon, at pressures greater than 50,000 atmospheres and temperatures higher than 1300°C, and each crystal is unique. types Ia, Ib, IIa and IIb occurs naturally in the proportions 98%, 0.1%, 1% to 2% and effectively zero. A final classification is derived from whether the diamonds are natural or synthetic. Diamonds can be formed synthetically by replicating the conditions under which they form naturally in a diamond press which creates high pressures and temperatures under which the carbon dissolves in a metal solvent (nickel, tungsten and vanadium for example). Small metallic inclusions may occur in diamonds manufactured like this resulting in a 'butterfly' shaped strain pattern appearing around them in polarised light images of the samples. Natural and synthetic diamonds may be artificially annealed under high temperature and pressure to alter the composition of the point defects in them for cosmetic purposes but such diamonds are not included in this study. A common method for manufacturing diamonds at low pressures is chemical vapour deposition, or C.V.D., in which a plasma consisting of methane and other gases is heated, often using microwaves, under low pressure, to deposit atoms of carbon on a silicon or silicon carbide substrate. Such diamonds are highly polycrystalline since their formation has nucleated on a surface rather than at a point and as such are unsuitable as radiators in coherent bremsstrahlung experiments. They are not included in this study.

3.2.2 Defects in Diamonds

An ideal lattice structure is devoid of defects, and crystal behaviour must be understood in relation to such structures, however, in a realistic sense there are no ideal crystal lattices, as even the constraint of being of finite extent interrupts the lattice with surfaces. In fact the physical behaviour of crystals is often dominated by the defects which are inherent in the structure, disrupting their translational symmetry, and diamond is no exception.

A structural defect is a configuration of atoms in the lattice which does not conform to the rules that pertain to the ideal reference state of the material, rules which can be used to generate mathematically an ideal lattice. Defects are distributed throughout the lattice in an inhomogeneous way, so that they cannot be accommodated by a revision of those rules. Defects in diamond, that is, inhomogeneous deviations from the ideal lattice structure, can be classified according to their dimensionality. Vacancies or clusters of vacancies have a dimensionality of zero and are known as point defects. When these combine to form a one dimensional structure a line defect is the result. Defects with a dimensionality of two are known as planar defects. A three dimensional defect, in which most lattice sites have been abandoned by the material in that volume, would be termed a phase change !

Point defects

These may be constituted by one of, or a cluster of, three things [28]. A vacancy is a lattice site which is unoccupied. An impurity is an atom of a type of material alien to the crystal occupying a lattice site. An atom which occupies a location between lattice sites is termed interstitial, and if it is an atom of the material which constitutes the crystal it is termed self-interstitial. Defects may be intrinsic, resulting from thermal effects, or may be extrinsic such as those caused by

radiation damage, doping or other external factors.

If the atom that has left the lattice site of a vacancy escapes completely from the lattice the vacancy is termed a Schottky defect. If the atom occupies an interstitial site and the associated strain field does not overlap with that of the vacancy so that they do not recombine the pair of defects are known as a Frenkel defect. Point defects can form complexes which may carry an electrical charge. The electronic energy level transitions associated with such point defects cause optical absorption at variance with the optical properties of the ideal crystal and are known as colour centres, since they bestow upon the crystal colour. In diamond the most common point defect is the Nitrogen impurity. A single nitrogen can occupy up to 1 in 1000 lattice sites, in an unaggregated form, imbuing a yellow hue to the crystal. These nitrogen impurities can aggregate through migration through the crystal to form A centres, comprising two nitrogen atoms, or B centres, comprising four nitrogen atoms plus a vacancy. Denoting a vacancy by V, it is found that N-V, N-V^- and N_3-V centres also occur, the latter yielding a yellowish- brown colour. N-V-N and (N-V-N)$^-$ centres are found to occur after treatment of a diamond with high pressures and temperatures, the latter being very rare in natural diamonds. B centres are found to persist during annealing.

The growth of a crystal is governed by the formation of defects, defect free growth being much slower than defect rich growth. This is because the configuration of the crystal will be one that tends to minimise the Gibbs free energy G. This is given by the expression $G = H + n_i h_i - T(S + \Delta S)$ where n_i is the number of defects of species i, h_i is the enthalpy associated with their formation, H is the enthalpy of formation of the perfect lattice, S is the configurational entropy of the perfect lattice and ΔS is the change in the configurational entropy due to the presence of defects. It is seen that the increase in configurational entropy incurred by the concentration of defects is offset by the energy associated with

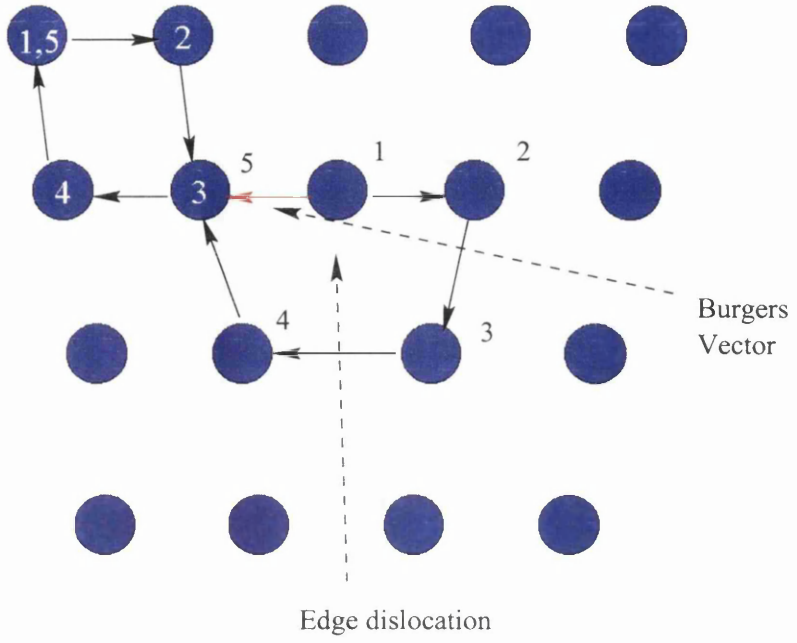

Figure 3.1: A schematic edge dislocation.

their formation, and that a minimum of the Gibbs free energy occurs at a finite concentration of defects. Defects whose concentrations are normally determined by thermodynamic considerations are termed *intrinsic*. The concentration of intrinsic defects however may be affected by the concentration of extrinsic defects, those caused by irradiation and other damage, and the influence of this on the thermodynamic equilibrium characterised by the minimisation of the Gibbs free energy.

Line defects

Line defects are termed dislocations, and have a dimensionality of one. There are two limiting cases of a continuum of possible line defects, the edge dislocation

and the screw dislocation. A line defect can be described as having edge and screw components. A pure edge dislocation can be seen as a structure where an additional half plane has been inserted into the lattice, as shown in figure 3.1. In this figure we see it is characterised by its Burgers vector. This is deduced by considering a loop of atoms which under normal circumstances would terminate on the lattice site on which it originated. If this loop of five lattice sites contains a line defect it is seen that it terminates on a different lattice site to the one on which it originated; the difference between these two lattice sites is the dislocation's Burgers vector. In the figure the sites number with white numbers do not include a dislocation and so site 5 is seen to be identical with site 1. The sites numbered in black enclose a dislocation and the difference between site 1 and 5 is the Burgers vector. It is seen that in the case of an edge dislocation the Burgers vector is perpendicular to the line of the defect, and lies in the slip plane.

The defect may migrate through the crystal medium by slip along the direction of the Burgers vector. The planes along which slip occur are those with the densest atomic packing such as the $\{111\}$ planes and in $\langle 110 \rangle$ directions. Sufficient applied shear stress in any crystallographic direction will induce slip in that direction, however.

A screw dislocation is shown in figure 3.2. Here it is seen that if a loop of lattice sites enclosing the dislocation is traversed it terminates on a lattice site further along the line of the defect, the path having followed a "screw-like" trajectory. Therefore the Burgers vector in the case of a screw dislocation is parallel with the line of the dislocation and the defect migrates in a direction perpendicular to the Burgers vector. In this figure the loop of sites numbered in blue enclose the dislocation, and those numbered in black represent a loop that does not include a dislocation.

In general, the Burgers vector $\underline{b}$ is constant throughout the length of a dislocation,

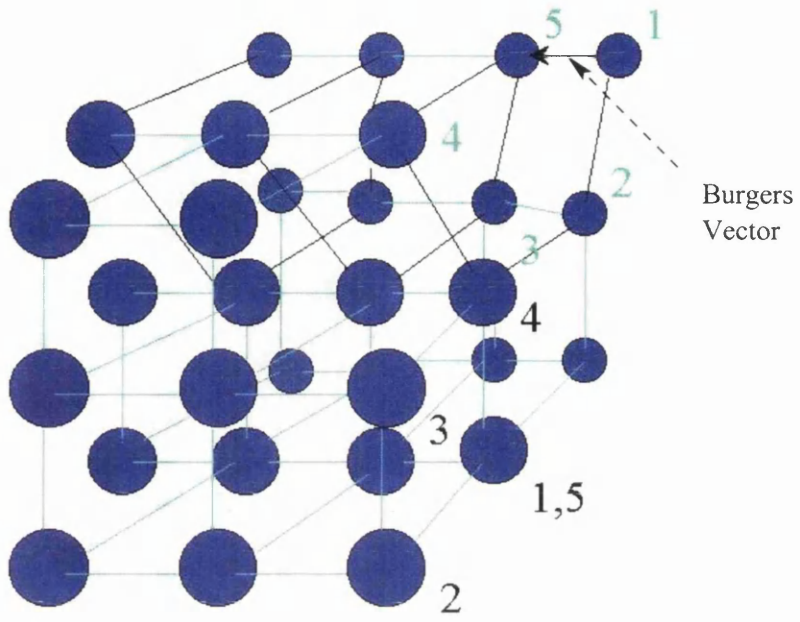

Figure 3.2: A schematic screw dislocation.

even if the dislocation changes direction. This can be seen as the dislocation having different characters at different sections; sometimes screw- like, sometimes edge-like, sometimes a combination of both. It seen from the definition of a Burgers vector that a dislocation cannot end in the middle of a crystal, therefore if it does not terminate at the surface it must form a loop or end at a node of a branched network of dislocations. At such a node Burgers vectors are conserved: $\sum \underline{b} = 0$.

Dislocations induce stress in the crystal, and the associated elastic energy is a few eV per crystal plane threaded by the dislocation [29]. The energy is proportional to b^2, such that it is energetically favourable for a dislocation to branch into dislocations whose energies sum to less than that of the complete dislocation. These may be partial dislocations, whose Burgers vectors are not translation vectors of the lattice; these must therefore border a two dimensional defect such

as a stacking fault.

The Burgers vector of a dislocation can be determined using X-ray topography, which will be described below. The scattering amplitude for the reflected X-rays that form the image is a summation over atoms i in the unit cell

$$F_{hkl} = \sum i f_i \exp(i\underline{G} \cdot \underline{R_i})$$

where $G = G_{hkl}$ is the reciprocal lattice vector of the plane associated with the X-ray reflection. When a dislocation is encountered, R_i no longer satisfies the translational periodicity that characterises the lattice but instead can be written as $R_i' = R_i + u_i$ where u_i is the displacement of the atom from the position it would hold in an ideal lattice. This yields an extra phase factor $\exp(i\underline{G} \cdot \underline{u_i})$ which must equal unity for the reflection from the dislocation to be extinguished, that is for the dislocation to be invisible in the X-ray topograph acquired using reflection $\underline{G}$. Therefore in such topographs where the dislocation is not visible $\underline{G} \cdot \underline{u} = 0$. In the case of screw dislocations $\underline{u}$ is parallel to $\underline{b}$ and so $\underline{G} \cdot \underline{b} = 0$. Screw dislocations are invisible in topographs taken using reflections from planes whose reciprocal lattice vectors are perpendicular to the dislocation line. In the case of edge dislocations this condition also obtains, in addition to $\underline{G} \cdot (\underline{b} \times \underline{t}) = 0$ where $\underline{t}$ is a vector along the dislocation line, since the displacement vector $\underline{u}$ is non-zero in all directions normal to the dislocation line. Edge dislocations are invisible in topographs acquired using reflections from planes whose reciprocal lattice vectors are parallel to the dislocation line.

In the case of line defects arguments relating to the minimisation of Gibbs free energy do not apply. Whereas the formation energy of point defects is independent of the number of atoms in the sample and can thus be offset by a gain in entropy $\sim \ln N$, the formation energy of extended defects is proportional to their dimensions ($\propto N^{1/3}$ in the case of line defects, $\propto N^{2/3}$ in the case of planar de-

fects) and therefore extended defects exist in a metastable state not subject to the constraints of thermal equilibrium. They are therefore more prone to modification through annealing.

Planar defects

Planar defects occur at grain boundaries in polycrystalline samples, and at crystal growth horizons as the deposition of atoms onto the crystal occurs preferentially onto the octahedral surfaces of the $\{111\}$, $\{\bar{1}11\}$, $\{1\bar{1}1\}$, $\{11\bar{1}\}$, $\{\bar{1}\bar{1}1\}$, $\{\bar{1}1\bar{1}\}$, $\{1\bar{1}\bar{1}\}$ and $\{\bar{1}\bar{1}\bar{1}\}$ planes, these planes offering the fastest opportunity to grow. It appears that crystal growth is mediated in part by a nitrogen catalyst which combines with the lattice more easily on these planes, thereby causing this differential growth pattern.

As well as external surfaces, an ostensibly single crystal may contain internal surfaces marking the boundaries between grains, or subdivisions of the crystal. These grain boundaries can be considered a linear array of line dislocations; if edge dislocations, a tilt boundary is the result, which causes a slight misorientation of one grain relative to its neighbour. A linear array of screw dislocations causes a twist boundary between grains, where the misorientation is about an axis perpendicular to the grain boundary. This distribution of orientations within the structure of a single crystal can affect processes that involve the orientation of crystal planes, such as coherent bremsstrahlung and X-ray topography.

3.3 The Samples

A selection of specimens were tested using the various tests described below, and the results of those tests compared to the quality of coherent bremsstrahlung

List of Diamond Specimens Investigated						
Sample	*Name*	*Type*	*Thickness (μm)*	*Thickness (rad. lengths)*	*Plane*	*Synthetic/ Natural*
1	dBb	Ib	100	7×10^{-4}	(001)	Synthetic
2	dBb	Ib	< 18	$< 1.2 \times 10^{-4}$	(001)	Synthetic
3	GWUrr	Ia	50	3.3×10^{-4}	(001)	Synthetic
4	Bonn C	Ib	120	8×10^{-4}	(011)	Synthetic
5	Bonn A	Ib	110	7.3×10^{-4}	(001)	Synthetic
6	GWUgg	IIa	50	3.3×10^{-4}	(001)	Synthetic
7	GWUgr	IIa	100	7×10^{-4}	(001)	Synthetic
8	"Peise"	IIa	40	2.6×10^{-4}	(011)	Natural
9	1236/1	I	100	7×10^{-4}	(001)	Synthetic
10	1236/2	I	100	7×10^{-4}	(001)	Synthetic
11	1236/3	I	100	7×10^{-4}	(001)	Synthetic
12	1236/4	I	100	7×10^{-4}	(001)	Synthetic

Table 3.1: A table listing the samples used in this survey.

spectra produced using them. A code was available [30] which was used to calculate the theoretical coherent spectra that would be obtained using a perfect crystal radiator for comparison with those acquired using the selected samples in order to determine the extent to which the spectra had been degraded by the samples' deviation from the ideal. The list of samples used can be seen in table 3.1, which lists the name by which they were habitually denoted, their classification, thickness in microns and radiation lengths, the crystal plane corresponding to the surface of the specimen and whether it was synthetic or natural in origin.

The samples were selected to cover a range of classifications and thicknesses in

order to allow the efficacy of the procedures employed for determining suitable specimen for coherent bremsstrahlung to be tested. Sample 2 is sample 1 ground down to as thin as present technology permits, to test the effects of diamond thickness.

3.4 Tests of Diamond Quality

Three different and complementary techniques have been used. The first uses polarised light. Strains in the crystal set up local areas of birefringence which can be analysed with polarised light. The specimen is mounted on a petrographic microscope and illuminated from below by light produced using a normal tungsten filament passed through a polaroid. A "crossed" polaroid is mounted above the specimen oriented perpendicular to the polaroid imposing linear polarisation on the light illuminating the sample. If we have a perfect specimen no light should be transmitted, and any light that can be observed corresponds to these areas of local birefringence caused by strain in the crystal. The strain pattern can be clearly observed, photographed using tungsten balanced film, and interpreted. Other tests included an investigation of local misalignments using X-ray topography, and a quantitative assessment of their quality using rocking curve measurements, which give the intensity of an X-ray reflection over a range of angles through which the sample is "rocked".

3.4.1 Petrographic Microscopy

An unstrained diamond is not birefringent. However, areas of strain induce local birefringence in the crystal that can be analysed using polarised light to indicate

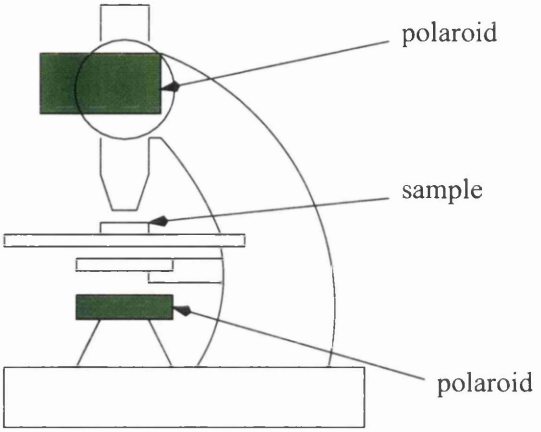

Figure 3.3: A schematic view of a petrographic microscope.

the nature and extent of the strain fields that are present in the crystal [31, 32]. The strain fields may be caused by microscopic inclusions, or stray fragments of foreign matter, often metallic solvent in the case of synthetic diamonds. These are revealed by a characteristic "butterfly" pattern in the image. The strain fields can also be caused by growth horizons as the crystal has formed around a seed. This results in a strain field with a "picture frame" pattern. When the crystal has been metamorphosed geologically while subject to high temperatures and pressures after it has formed, in the Earth's mantle in the case of natural diamonds, in the diamond press in the case of synthetics, plastic deformation can occur, which is revealed by braided strain patterns, in which line defects lie in bundles in the image.

The apparatus required to perform this procedure is shown in figure 3.3. The light source is polarised by a polaroid placed between it and the sample, which is then viewed through a second "crossed" polaroid, whose axis has been rotated by 90 degrees with respect to the first, such that only light whose polarisation vector has been rotated by the strain field will be transmitted through the second polaroid.

It is apparent that different forms of strain field are signatures that characterise particular defects and deformations of the crystal, some of which will be seen to have more serious implications for coherent bremsstrahlung than others, therefore this technique is a good method for initially flagging which specimens may later prove to be inadequate for the purposes of this study.

3.4.2 X-ray Topography

A technique which images all or part of the crystal and which is of great utility in identifying suitable specimens for use in photonuclear studies is X-ray topography. The specimen is illuminated by an intense distant X-ray source to ensure the X-ray beam is parallel. The image of the crystal acquired from the reflected X-rays is an X-ray topograph. Images of the beam taken on reflection (where the reflecting planes are parallel to the surface of the sample) or transmission (where the reflecting planes are perpendicular to the surface) will yield information about the crystal according to the manner in which the conditions for reflection have been modified by the presence of defects. Reflection and transmission topography can be practised using planes that are not strictly parallel and perpendicular to the sample surface respectively - it is sufficient that the diffracted beam observed emerges from the same surface that the primary beam is incident upon in the case of reflection topography, or the opposite surface in the case of transmission topography (having traversed the entire volume of the sample). However planes perpendicular and parallel to the surface were used in this study.

X-ray topographs can be used in conjunction with images of the sample taken using visible polarised light and a crossed polaroid which reveals the features such as defects and inclusions in the specimen by exploiting the local birefringence associated with the strain fields they generate. Topographs taken under the

transmission regime reveal features evident throughout the bulk of the sample and correspond more closely with those revealed using crossed polaroids and optical wavelengths, i.e. so-called petrographic microscopy, whereas images taken using the reflection geometry are heavily weighted in favour of features close to the surface of the sample.

Topographic Contrast

For information regarding the crystal to be extracted from topographs by their inspection, it is necessary to understand to some extent the the origin of the images, that is, how the contrast in the images arises [33]. The interpretation of topographic and rocking curve data can be an intractable inverse problem but some broad classifications can be made.

Topographic contrast can be classified as either orientation contrast or extinction contrast. Orientation contrast is associated with the direction of crystal axes varying as a result of granularity, polycrystalinity, or strain due to differential growth patterns, inclusions and other defects and is illustrated in figure 3.4. The orientation of the crystal is itself changed. In the case of a white or polychromatic X-ray beam, this results in the reflected flux not preserving the parallel nature of the incident beam, and so a distorted image may result. In the case of double crystal experiments, where a monochromatic beam is used, misalignment may result in a reduced reflected flux, or no flux being reflected at all if the orientation of the crystal departs too far from the Bragg conditions. Extinction contrast arises as a result of these conditions being violated due to distortion caused by a defect. In this case the variation in lattice parameters caused by the defect, rather than an orientational variation, is the cause of differential X-ray scattering which manifests itself as topographic contrast. The rate of attenuation of the diffracted beam varies due to the presence of imperfections in the crystal, causing contrast.

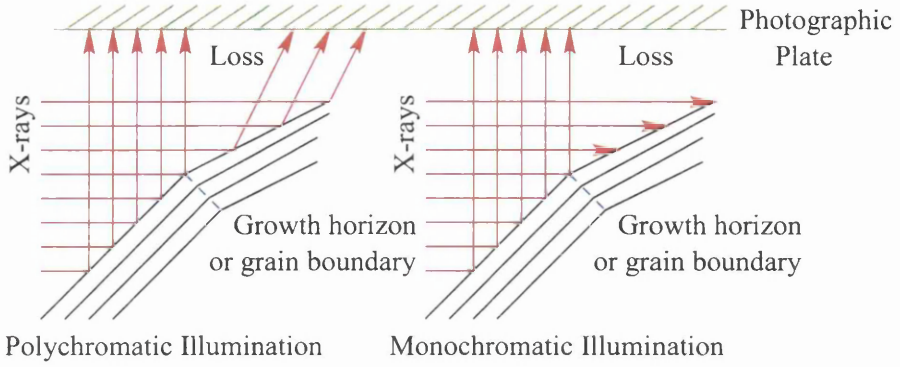

Figure 3.4: The origins of orientational contrast in topography.

Single Crystal Topography

Single crystal topography is sometimes known as projection topography. The sample is oriented to the beam satisfying the Bragg conditions for the reflection of a one wavelength in the white spectrum of the X-ray beam. The whole sample is illuminated by the beam, and the reflection of the parallel X-rays can be used to acquire a photographic image of the crystal. Deviations from the Bragg conditions in regions of the crystal due to defects causing slight misorientation of the crystal planes, or the introduction of phase factors in the scattering of the X-rays due to localised departures from the distribution of scattering centres in the lattice caused by defects, will result in topographic contrast, where the reflected X-ray flux is affected. The experimental setup for projection topography is illustrated on the left of figure 3.5.

Topographs can be acquired in reflection or transmission geometries, shown at the bottom left and top left of figure 3.5 respectively. In the case of reflection geometry, the reflected X-rays exit the same side of the sample as the side upon which the X-rays are incident. Information obtained using this method pertains

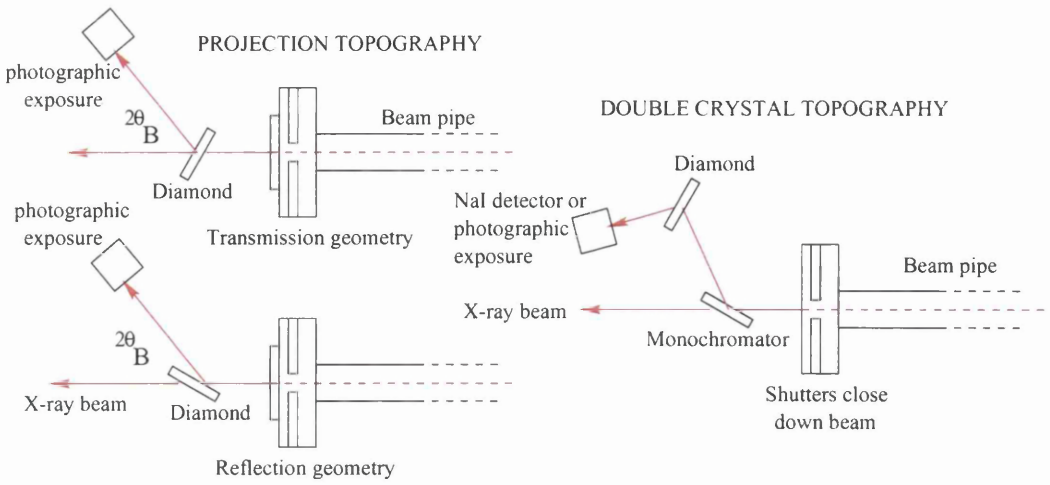

Figure 3.5: The different geometries of X-ray topography.

to the surface regions of the diamond. In the case of transmission geometry, the reflected X-rays are seen to be transmitted through the body of the specimen, and exit the opposite side to the side upon which the X-rays were incident. The entire crystal is sampled using this method and information obtained pertains to the whole volume of the crystal.

Double Crystal Topography

A single wavelength for the purposes of analysing a specimen can be selected by using a monochromator. This is illustrated on the right of figure 3.5. A crystal of silicon is typically used, and placed in the beam, oriented to satisfy the Bragg condition for the desired wavelength, which is thus selected by reflection from the monochromator. The diamond is placed in this monochromatic beam and oriented to satisfy the Bragg conditions for reflection from a specific set of planes. The reflection of this monochromatic beam from the sample can be used to obtain a photographic image, or topograph, of the sample. This topograph is

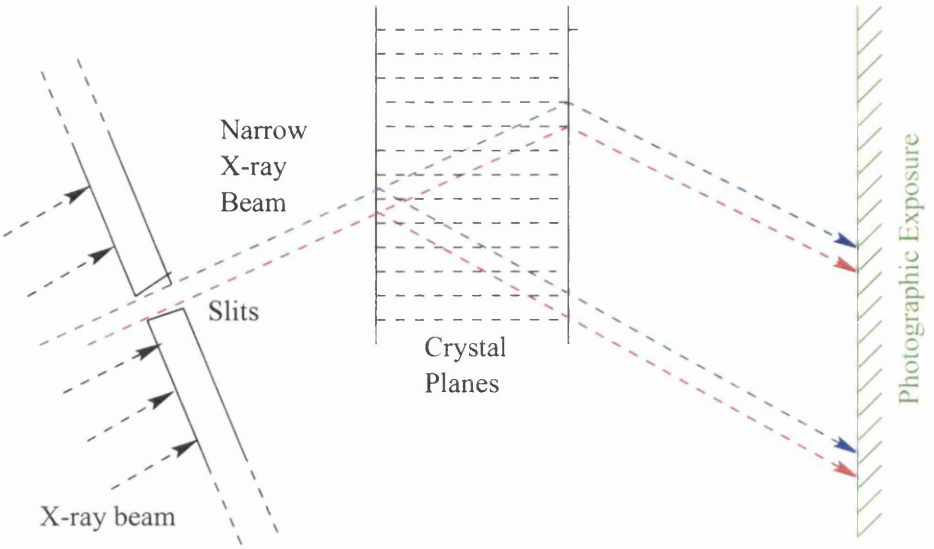

Figure 3.6: A section topograph schematic.

a double crystal topograph, so termed because of the double reflection the X-ray beam undergoes from two distinct crystals, the silicon and the diamond. The reflected flux plotted against orientation of the sample is not a delta function, as has been seen in relation to dynamical X-ray scattering theory, but follows a "rocking" curve, that is, the curve describing the variation in reflected flux with crystal orientation. It is advantageous to orient the diamond specimen at a position midway up one side of the its own rocking curve before taking double crystal topographs, so that misorientations of crystal planes related to strain and other effects causes the greatest variation in reflected flux and therefore results in the greatest degree of topographic contrast. Again, to sample the whole volume of the crystal, the topograph should be acquired with the crystal arranged in the transmission geometry, as shown in figure figure 3.5.

Section Topography

If the incident X-ray beam has dimensions smaller than the thickness of the sample it is seen that cross-sectional information can be obtained. This is illustrated in figure 3.6. Slits can be applied to the X-ray beam to ensure that the width of the beam is narrower than the width of the base of the Boormann fan. When this is the case, the resulting topograph will contain information derived from reflection in a single Boormann fan or a small set of slightly overlapping fans, rather than a large number of overlapping fans which traverse a significant volume of the crystal. This confines the part of the crystal sampled by the beam to a cross-sectional area, with a resolution determined by the width of the beam, which is what restricts the number of overlapping Boormann fans.
Since the X-rays are at all times parallel the inspection of section topographs requires the using of a microscope, or photographic enlargement for offline analysis. The images obtainable are of the dimensions of the illuminated region, that is, the size of the sample. In section topography this implies they are narrow strips of a width comparable to the crystal thickness, which may result in the granularity of the photographic emulsion fatally limiting resolution.

3.4.3 Rocking Curves

The rocking curve of a sample is the variation in the reflected X-ray intensity as the sample is rotated relative to the incident beam to make its orientation pass through the Bragg condition. These can be measured by placing the sample in the position one would to take a double crystal topograph and locating an X-ray detector where the photographic exposure is in figure 3.5. The monochromator is rotated to reflect monochromatic X-rays onto the sample from the primary X-ray beam and the flux reflected by the sample measured at different orientations

incrementally scanned through the Bragg condition.

The rocking curves should be interpreted in relation to the theoretical rocking curve width that would be obtained from a physically unrealistic ideal lattice as predicted by dynamical X-ray scattering theory. This FWHM is

$$W_{theo} = 2 \times (\frac{e^2}{m_e c^2}) \times \frac{\lambda^2 |F|}{\pi a^3 \sin 2\theta_B}$$

where λ is the X-ray wavelength, a is the lattice parameter for diamond, $F = \alpha f$ (α being an integer depending on the crystal reflection being used, f being the mean atomic scattering factor for electrons in carbon) and θ_B is the Bragg scattering angle. In the case of 1.3ÅX-rays reflecting from the {004} planes in diamond $W_{theo} = 8.6\mu$rad, and the angular resolution of the diffractometer used at Daresbury to acquire the rocking curves in this study was 0.5μrad. All the crystals examined in this study have $W_{theo} < 10\mu$rad, other then sample 4 which is the only specimen in which the [110] orientation of the diamond has been investigated. For 1ÅX-rays $W_{theo} = 5.1\mu$rad for reflection off the {004} planes.

A broadening of the rocking curve can be attributed to the crystal by considering the measured width to be the result of adding the theoretical width to the broadening in quadrature thus

$$W^2_{meas} = W^2_{theo} + W^2_{crystal}$$

and so a numerical value for the contribution to the width from the crystal defects is determined.

It has been seen that the reflection of the primary beam in the monochromator directs the beam upwards, whereas the subsequent reflection in the diamond directs the beam back downwards toward the X-ray detector or photographic plate. The reason for this arrangement can be illustrated with reference to the rotations shown in figure 3.7. In A) we see the conventional (+-) setting, with the primary beam (red in the diagram) being reflected twice, once from the

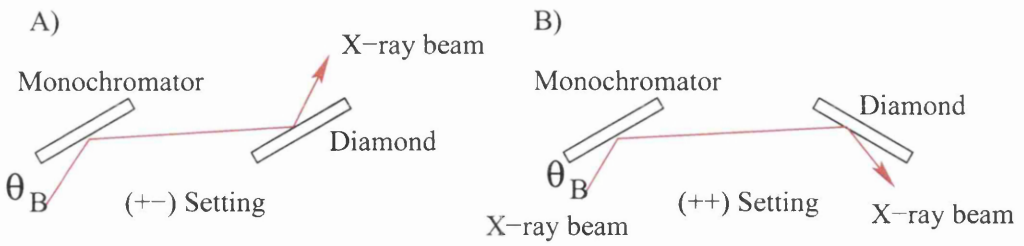

Figure 3.7: Rocking curve crystal rotations.

monochromator, then from the diamond, the last reflection being directed in the opposite sense to the first. In B) the (++) setting is shown, with the reflections of the primary beam both being in the same sense. The first case, the (+-) setting, was the operational mode selected, since this resulted in the rocking curve width being determined by the properties of the diamond under investigation, rather than being influenced by the properties of the silicon monochromator, as would be the case if the (++) setting were selected.

3.5 Results

Table 3.2 shows the tests which were performed on each sample. An entry in a column across from a sample number indicates the figure in which the results of that test is shown. The column labelled Pol. refers to analysis with polarised light, XRT denotes projection topography, DXT denotes double crystal topography, FXR denotes full crystal rocking curve, in which the whole sample was illuminated by the beam, R.C. indicates a rocking curve where only a small portion of the sample was illuminated with the beam, C.B. denotes coherent bremsstrahlung, and S.T. denotes section topography.

In all cases where a rocking curve was obtained, transmission rocking curves were taken, that is, the X-rays were reflected from planes perpendicular to the sur-

List of Tests Performed							
Sample	*Pol.*	*XRT*	*DXT*	*FXR*	*R.C.*	*C.B.*	*S.T.*
1	3.8	3.9	3.11	3.12	3.12	3.13	3.10
2	-	-	-	-	-	3.14	-
3	3.15	-	-	-	3.15	-	-
4	3.16	-	-	-	3.15	-	-
5	3.17	-	-	-	3.17	-	-
6	3.18	3.18	-	-	3.18	-	-
7	-	-	-	-	3.21	3.19/20	-
8	3.22	3.22	-	-	3.22	-	-
9	3.23	3.24	-	-	-	-	-
10	3.23	3.24	-	-	-	-	-
11	3.23	3.24	-	-	-	-	-
12	3.23	3.24	-	-	-	-	-

Table 3.2: A table listing the tests performed in this survey.

face, such that the beam intensity measured had penetrated the entire depth of the crystal. All samples were rotated from negative to positive values of crystal angle during rocking curve measurements. In all topographic images the reciprocal lattice vector of the plane selected is directed vertically, perpendicular to the line of sight. Tungsten balanced slide film was used to obtain the polarised light analyses as the samples were illuminated using a conventional tungsten filament light bulb.

A summary of the results of the rocking curves is shown in table 3.3. For each sample, the type, X-ray wavelength, reflection plane used, Bragg angle, beam-size, theoretical rocking curve width, measured rocking curve width and width

Contributions to Rocking Curves Widths								
Sample	*Type*	λ *(Å)*	*Plane*	θ_B	*Beamsize (mm×mm)*	W_{theo} *(μrad)*	W_{meas} *(μrad)*	$W_{crystal}$ *(μrad)*
1	Ib	1	(004)	33°.9	0.25 × 0.25	5.4	6.7	3.9
3	Ia	1	(004)	33°.9	0.25 × 0.25	5.4	8.6	6.7
4	Ib	1.3	(022)	31°.1	0.15 × 0.15	11.9	25	22
5	Ib	1.3	(004)	47°.2	0.15 × 0.15	8.6	38.4	37.4
6	IIa	1	(004)	33°.9	0.25 × 0.25	5.4	$\sim$ 1200	$\sim$ 1200
7	IIa	1	(004)	33°.9	0.25 × 0.25	5.4	$\sim$ 500	$\sim$ 500
8	IIa	1.3	(022)	31°.1	0.25 × 0.25	11.9	$\sim$ 1000	$\sim$ 1000

Table 3.3: A table showing the rocking curve widths of the various samples.

attributed to the quality of the crystal are listed.

It is seen that type I diamonds exhibit narrow rocking curves, while the rocking curves of type II diamonds are prohibitively broad. The broadening of the rocking curves can be interpreted as indicating the degree of confidence one can have in the orientation of the reciprocal lattice vector in coherent bremsstrahlung experiments. The rocking curve widths can be compared to the angle that characterises bremsstrahlung at the energies of the primary electron beam used in Mainz, 855 MeV, which is $\sim$ 600μrad. This comparison forms the basis of the immediate rejection of the type II samples as candidate radiators.

Table 3.4 shows the results of coherent bremsstrahlung experiments for the samples for which the data was available. The data presented in the table relates to the widths of the coherent peak in the spectra. This is defined as the difference between the energies at which the minimum and maximum intensities occur in

the neighbourhood of this edge, that is

$$W_{edge} = E_{I_{rel}^{max}} - E_{I_{rel}^{min}}$$

This does not take into account the increase in incoherent background observed at all energies, nor deviations in the gradient of the edge from the theoretical prediction. These are seen in the diagrams, where the difference between the theoretical and observed relative intensities are shown, and where deviations from the theoretical gradient values are seen as a feature with a non-zero 2nd derivative in the plot of these differences at the energy of the edge. While the edge width is seen to deteriorate more for type II diamonds, the most marked effect is the increased incoherent background apparent in the figures. This is seen to be worse at higher energies.

The experimental data was divided through by an incoherent spectrum acquired using an amorphous nickel radiator. The intenisty scale was normalised in relation to the theoretical spectra shown by scaling the experimental data by a factor which made the intensity variation observed at an edge the same in both the experimental and theoretical spectra, since this intensity difference is due only to coherent phenomena. The normalisation factor applied to the experimental data was therefore

$$x = \frac{I_{rel(theory)}^{max} - I_{rel(theory)}^{min}}{I_{rel(expt.)}^{max} - I_{rel(expt.)}^{min}}$$

The figures showing the results summarised in these tables are presented below for each sample in turn.

3.5.1 Sample 1

In figure 3.8 the results of an analysis of this sample with polarised light is shown in which the presence of areas of birefringence due to strain caused by growth

Coherent Bremsstrahlung Edge Widths				
	Uncollimated		Collimated	
Sample	*Expt. (MeV)*	*Theory (MeV)*	*Expt. (MeV)*	*Theory (MeV)*
1	38	38	-	-
2	24	18	-	-
7	40	25	35	25

Table 3.4: A table showing coherent edge widths.

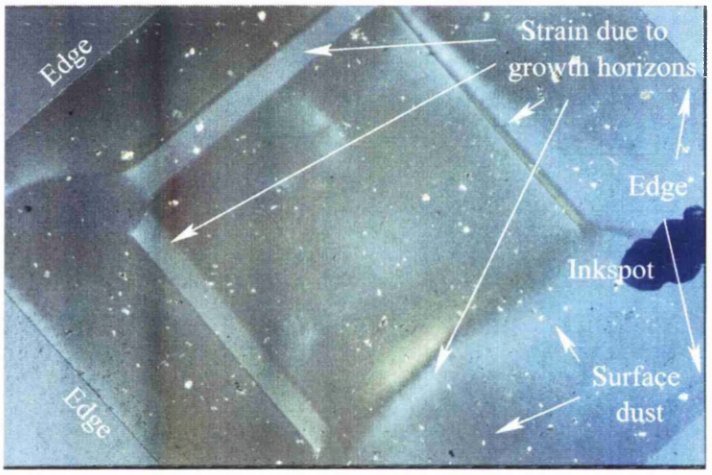

Figure 3.8: Sample 1 polarised light analysis.

horizons is shown. The edge of the sample is also shown, along with the presence of surface dust that is not associated with the sample and a reference inkspot that aided visual identification of the specimen. The image is comparatively featureless, indicating that there is little strain in the sample, and the little there is is highly localised.

Figure 3.9 shows the projection topograph of sample 1. In it the growth horizons are again manifested. On this diagram the location of the area illuminated with a narrow beam to provide the section topograph shown in figure 3.10 is shown.

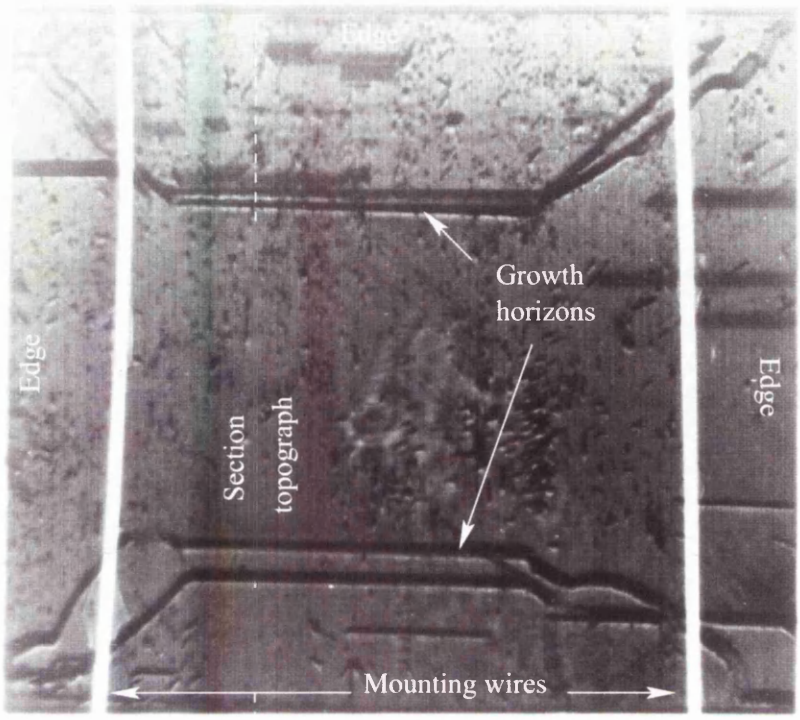

dBb type Ib 100 μ m thick [001] synthetic

Projection Topograph

Figure 3.9: A projection topograph of sample 1.

The left hand side of the section topograph corresponds to the bottom of the line indicated in the projection topograph. It is seen in the section topograph that the growth horizons extend through the sample's thickness, and that the growth boundaries are angled, proceeding further from the seed towards the edge of the sample as they extend through the depth of the cross section away from it as one might expect.

Figure 3.11 shows the double crystal topograph of sample 1 acquired using a 1ÅX-ray beam (12.5 keV) obtained using the {333} reflection from a silicon wafer monochromater inclined at the Bragg angle of $\theta_B = 28°.3513$ in the primary white beam. The Bragg angle for the reflection in diamond of X-rays of a wavelength

Figure 3.10: Section topograph of sample 1.

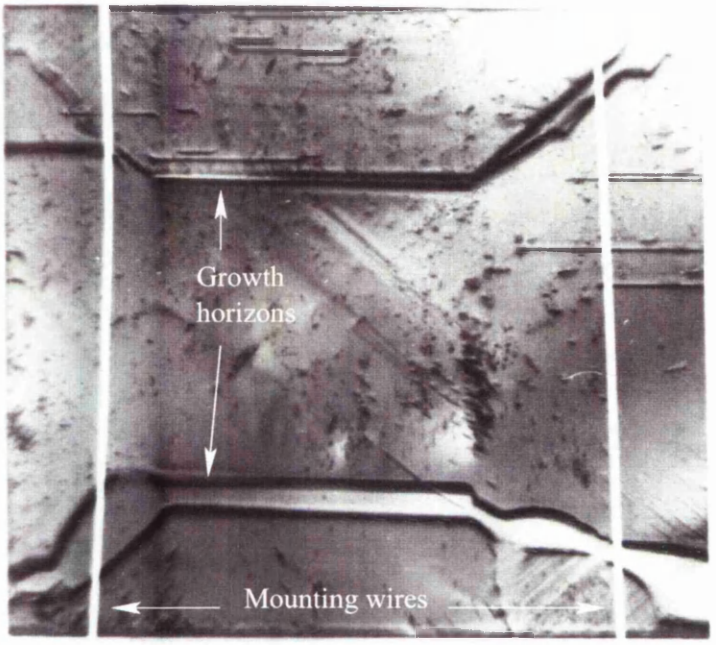

Figure 3.11: A double crystal topograph of sample 1.

of 1Åfrom the {004} planes is $\theta_B = 33°.894$. The double crystal topograph shows a very similar image to the projection topograph, indicating that tilt does not accumulate over the extent of the volume of the sample so as to orient an appreciable portion beyond the rocking curve, that is, the ranges of diamond angles in which reflection occurs, nor is there any granularity that would occur in a polycrystalline sample which might generate split images.

The defect density was low, although concentrated at boundaries caused by differential growth patterns. An analysis of topographs taken using reflections from

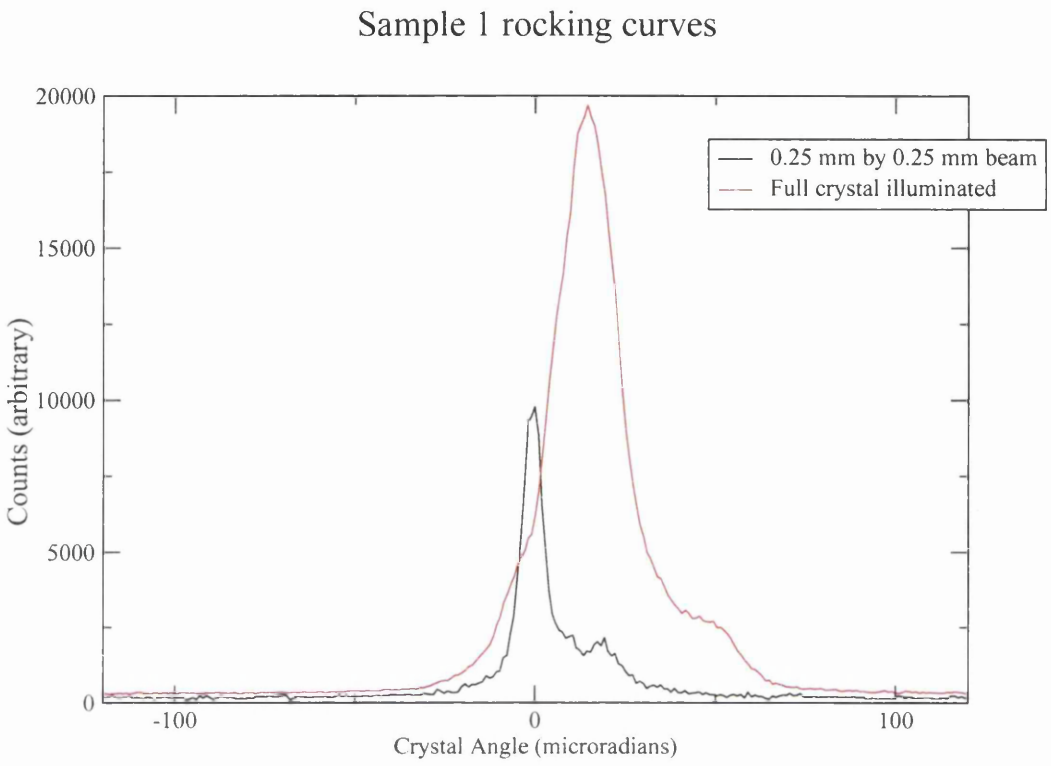

Figure 3.12: Rocking curves obtained using sample 1.

a variety of crystal planes and different rotations of the sample with respect to the beam showed that some defects vanished under certain reflections, by which around 50% of the defects had their Burger's vectors determined. Of these the Burger's vectors were found to be parallel with the [110], [111], [210] and [311] crystallographic directions, which are related to accepted Burgers vectors for diamond. It was not determined whether they were screw or edge in nature.

In figure 3.12 two rocking curves obtained from sample 1 are shown. The rocking curve shown in black was acquired using a 0.25 mm × 0.25 mm beamspot directed at the centre of the specimen. The red curve is the rocking curve obtained by illuminating the full crystal. The reflection chosen was from the {004} planes and X-rays of a wavelength of 1Å(12.5 keV). The sample was found to be of a very high quality with a rocking curve width of $W_{meas} = 6.7\mu$rad in the first case, and

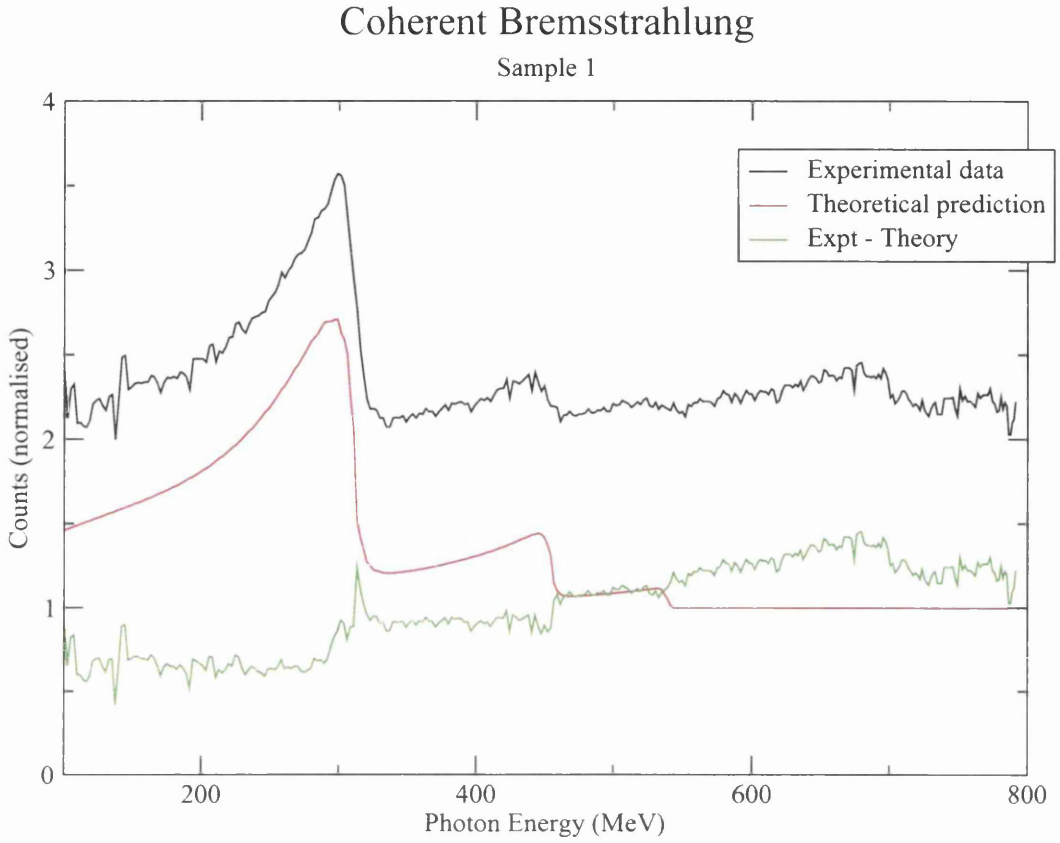

Figure 3.13: Sample 1 coherent bremsstrahlung.

a full crystal rocking curve width $W_{meas} = 23\mu$rad, where the widths are defined as the FWHM of the peaks.

In figure 3.13 a comparison of the experimental coherent bremsstrahlung data acquired using sample 1 with the theoretical prediction is shown. The angle between the beam and the [001] axis was set to 9 mrad in both cases. As with other coherent bremsstrahlung plots, the relative intensity is shown, that is, $I_{rel} = (I_{coh} + I_{incoh})/I_{incoh}$. The spectrum was acquired and then divided through by a reference incoherent spectrum acquired using an amorphous nickel radiator. The plot shows the experimental data, the theoretically prediction, and the result of subtracting the theoretical prediction from the experimental data to leave the contribution to the spectrum due to imperfections in the diamond.

The theoretical data took account of the effect of multiple scattering of electrons in the diamond, using a Moliere potential. The calculation also derived the theoretical incoherent component of the radiation which would occur if a perfect sample were used by modelling the thermal effects which displaced atoms from their lattice sites resulting in incoherent scattering of electrons. This behaviour is described by the Debye-Waller factor, which was calculated by taking the crystal temperature to be 293 K. This determines the fraction of atoms removed from the coherent to the incoherent scattering regime. The primary electron beam divergence was also taken account of in the calculation.

The green line in figure 3.13 shows the additional photon emission caused by the crystal's deviation from a perfect lattice, represented by the red curve. This extra component was taken to be incoherent, as the coherent componont is represented fully in the theoretical red curve. The consequence of this extra incoherent (and hence unpolarised) component due to the crystal's deviations from a perfect lattice is a degradation in the degree of linear polarisation that can be obtained using this sample. This will be seen to be more pronounced with poorer samples. The width of the most prominent coherent edge, the feature at a photon energy of 300 MeV, was the same in both the experimental data and the theoretical prediction, with the difference in the energies at which I_{rel}^{max} and I_{rel}^{min} occured being 38 MeV in this neighbourhood for both datasets.

The sharpness of the coherent edge obtained using this diamond is consistent with the demonstrated quality of the diamond. A deterioration in the sharpness of this edge is an indication of the degradation of the spectrum due to one or more of the three factors outlined above. This edge corresponds to the hard lower limit of the momentum pancake, that is, the low momentum transfer limit of the pancakes corresponding to the highest energy photons obtainable using this reciprocal lattice vector in this orientation. The low energy tail in this uncollimated spectrum

corresponds to the softer high momentum transfer limit of pancakes containing the reciprocal lattice vector. This corresponds to lower energy photon emission. Degradation of the sharpness of this edge can be caused by the orientation of the beam to the lattice being ill defined for one of the three reasons given below. This also degrades all other orientational effects such as polarisation. In the case of this sample however confidence can be held in the degree of linear polarisation that can be obtained using this diamond because of the sharpness of this edge. These results were duplicated using two other identically specified type Ib specimens which gave further confidence in them.

3.5.2 Sample 2

Sample 2 consisted of what remained of sample 1 after it had been ground down as thin as current technology permits without breakage. This reduced the thickness of the specimen to $< 18\mu$rad, although its thickness cannot be stated more accurately than that. This thinning of sample 1 allowed comparisons to be made which would shed light on the benefits of using diamonds that are as thin as possible, allowing the investigation of the improvement in the enhancement of the coherent part of the spectrum over the incoherent background due to a reduction in the influence of multiple scattering, recalling that $\theta_{scat} \propto \frac{\sqrt{t}}{E_0}$ where t is the crystal thickness in radiation lengths and E_0 is the primary beam energy.

The results of the full range of tests applied to sample 1 were deemed to apply to sample 2 apart from those that were the consequences of the sample thickness, therefore only the coherent spectrum was obtained for sample 2. This is shown in 3.14. The width of the coherent edge at a photon energy of 300 MeV was

$$E_{I_{rel}^{max}} - E_{I_{rel}^{min}} = 24MeV$$

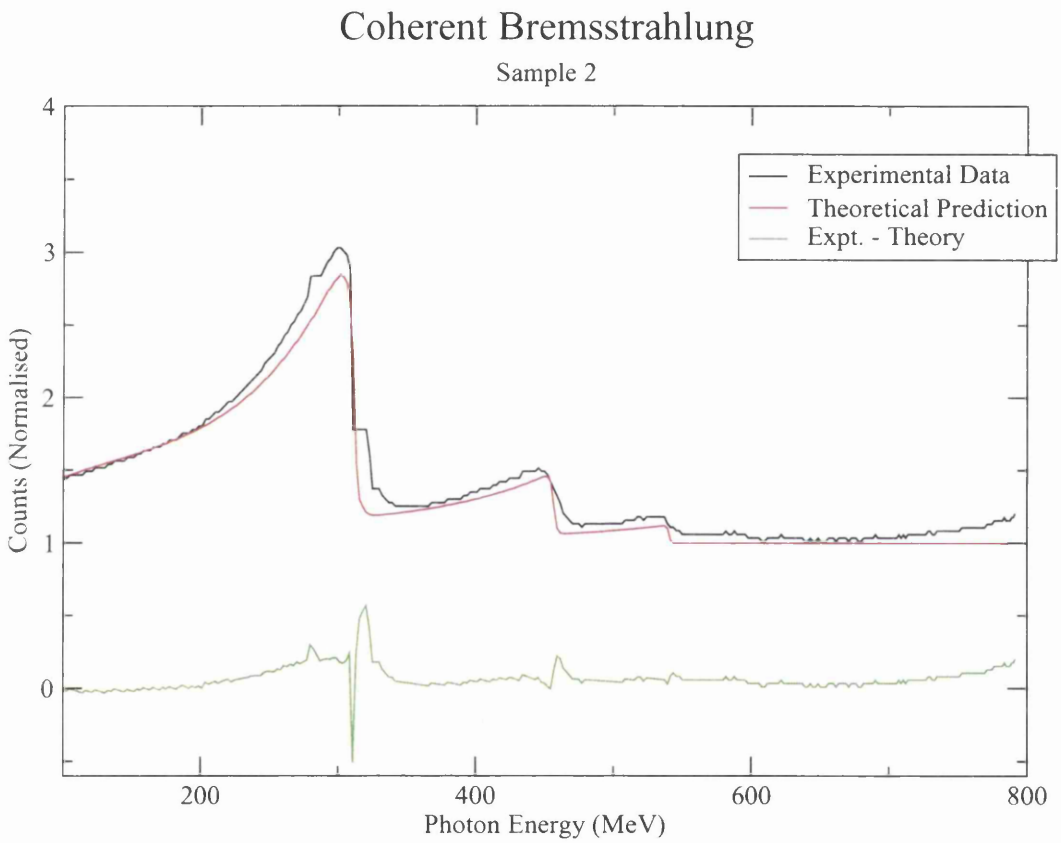

Figure 3.14: Sample 2 coherent bremsstrahlung.

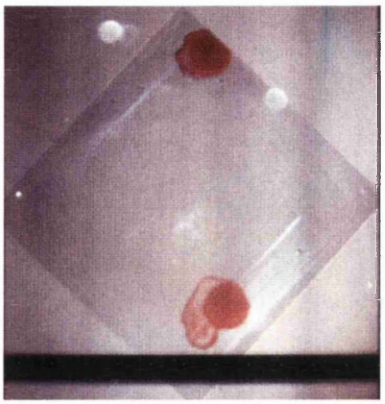

Polarised light analysis

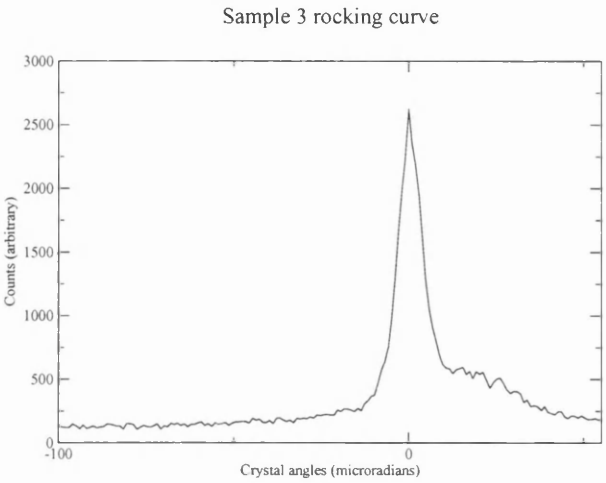

Figure 3.15: The crossed polaroid analysis and rocking curve of sample 3.

The thickness input into the simulation which generated the theoretical prediction was 18μm.

3.5.3 Sample 3

In figure 3.15 the rocking curve obtained from sample 3 using a 0.25 mm $\times$ 0.25 mm beamspot directed at the centre of the specimen is shown on the right. On the left the polarised light analysis is shown, and is seen to be essentially featureless. For the rocking curve, the reflection chosen was from the {004} planes using X-rays of a wavelength of 1Å(12.5 keV). The sample was found to be of a very high quality with a rocking curve width of $W_{meas} = 8.6\mu$rad. The correlation between a featureless image acquired using crossed polaroid analysis and a narrow rocking curve is shown, indicating that this specimen would be suitable for use as a radiator in coherent bremsstrahlung experiments.

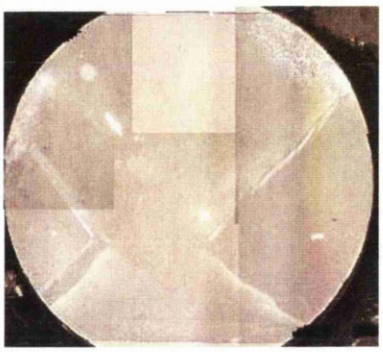

Polarised light analysis

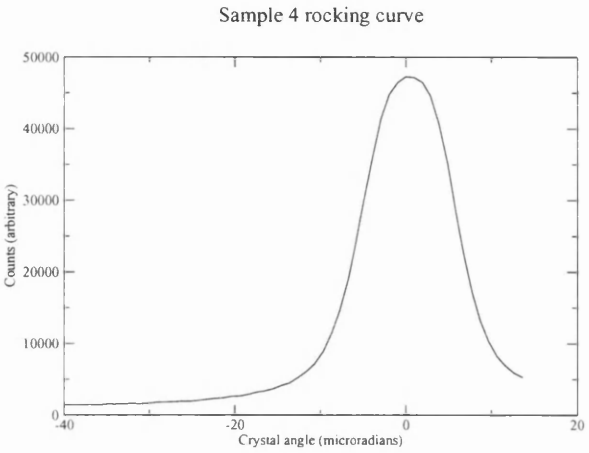

Figure 3.16: The crossed polaroid analysis and rocking curve of sample 4.

3.5.4 Sample 4

Figure 3.16 shows, on the left, the polarised light analysis of sample 4, and on the right, the rocking curve. The polarised light analysis again is relatively featureless. The rocking curve was acquired using a 0.15 mm × 0.15 mm beamspot directed at the centre of the specimen. The {022} reflection was chosen and X-rays with a wavelength of 1.3Å(9.5 keV) were used. The FWHM of the peak was found to be $W_{meas} = 25.0\mu$rad. A featureless image acquired under crossed polaroid analysis is shown to be associated with a very narrow transmission rocking curve.

3.5.5 Sample 5

Figure 3.17 shows, on the left, the polarised light analysis of sample 5, and on the right, the rocking curve. Inspection of the polarised light analysis reveals that a prominent inclusion has caused growth striations to be visible. The inclusion is probably a fragment of the metal solvent in which the diamond was formed. The rocking curve was acquired using a 0.15 mm × 0.15 mm beamspot directed

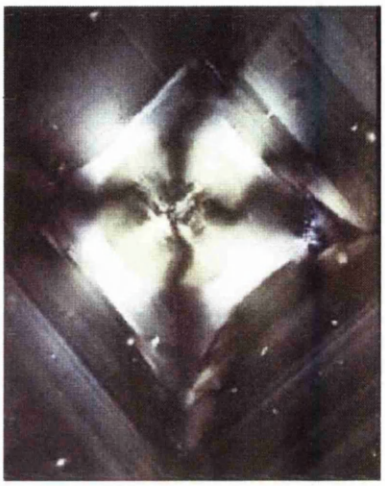

Polarised light analysis

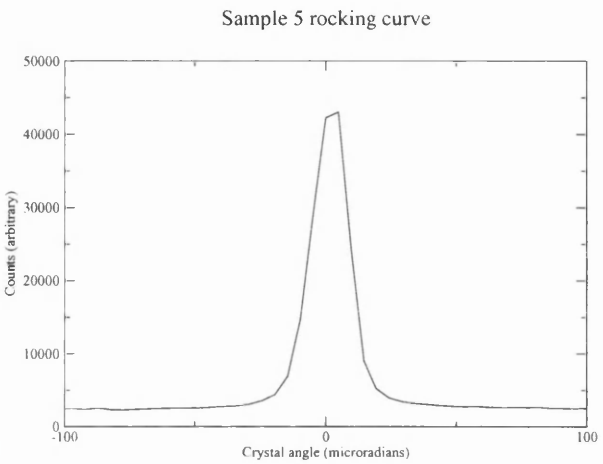

Figure 3.17: The crossed polaroid analysis and rocking curve of sample 5.

at the centre of the specimen. The {004} reflection was chosen and X-rays of a wavelength of 1.3Å(9.5 keV) were used. The FWHM of the peak was found to be $W_{meas} = 38.4\mu$rad. This was deemed to be too far in excess of the ideal minimum to admit this crystal as a viable candidate for coherent bremsstrahlung experiments. Nevertheless the rocking curve is fairly narrow and it is possible that regions of the crystal far from the inclusion may have properties appropriate to a radiator.

3.5.6 Sample 6

In figure 3.18, the polarised light analysis is shown on the top left, the projection topograph on the top right, and the transmission rocking curve at the bottom. For the rocking curve, the reflection chosen was from the {004} planes using X-rays of a wavelength of 1Å(12.5 keV). A 0.25mm × 0.25mm X-ray beam was used to illuminate the sample, centrally located. This type IIa specimen exhibits

substantial plastic deformation, as evidenced by the extensive braided strain patterns that extend throughout almost the entire volume of the sample. The extent to which the plastic deformation that has been incurred has distorted the crystal lattice is seen in the projection topograph which is extremely mis-shapen. The distortion of the image is a reflection of the extreme and unpredictable way in which the lattice parameters and the orientation of major axes in the crystal vary as a result of the deformation, rendering this sample unsuitable for use in coherent bremsstrahlung experiments. The unsuitability of this diamond is further manifest in the rocking curve, which has a width of more than 1200 μrad. This illustrates that the sample possesses an insufficiently regular crystal structure to bestow it with favourable and predictable properties necessary for a radiator.

3.5.7 Sample 7

The investigation of type IIa diamonds continued with sample 7. The uncollimated coherent bremsstrahlung is shown in figure 3.19 in black, with the theoretical prediction shown in red. The difference between the two is shown in green. The difference is marked and deteriorates at higher energies. The comparable data for collimated bremsstrahlung is shown in figure 3.20. The data presented in figure 3.20 was acquired by collimating with a collimator of radius 1.5mm placed 2.5m from the diamond. An improvement is seen, but it is not substantial enough to engender sufficient confidence in the degree of linear polarisation of the photons emitted for this sample to be deemed useful. The difference between the theoretical spectrum shown in figure 3.20 and the earlier theoretical spectra is a consequence of collimation.

The width of the experimental edge, defined as the energy interval between I_{rel}^{max} and I_{rel}^{min} in the neighbourhood of the edge, was 40 MeV and 35 MeV in the

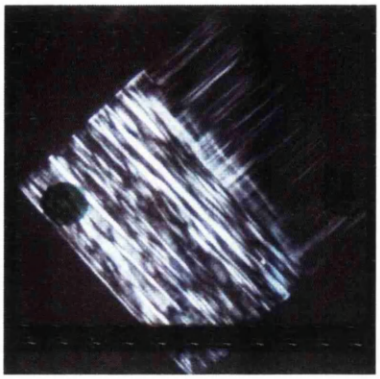

GWUgg Polarised Light Analysis

GWUgg Projection Topograph

Sample 6 rocking curve

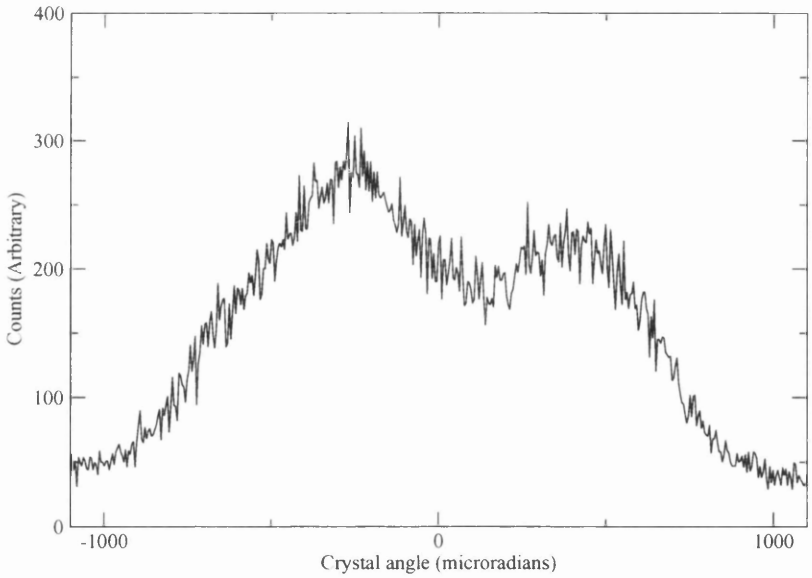

Figure 3.18: Plastic deformation petrographic microscopy, projection topography and rocking curve for sample 6.

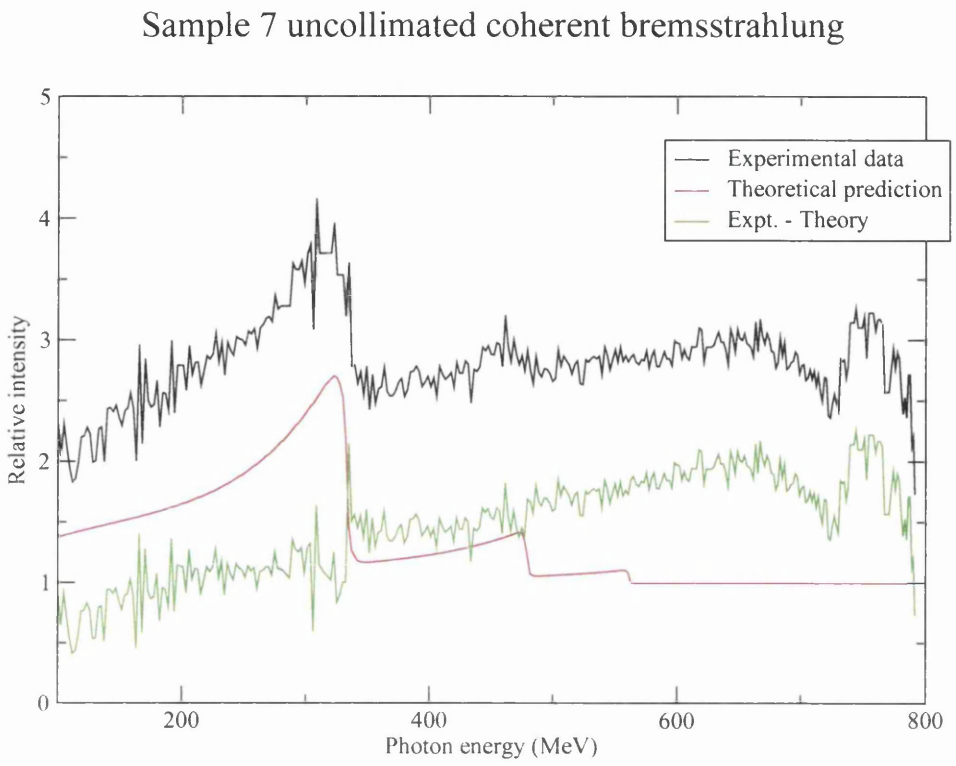

Figure 3.19: Coherent bremsstrahlung with theoretical prediction for sample 7.

uncollimated and collimated cases respectively, in comparison with a theoretical prediction of 25 MeV for both cases. There are high energy deviations from theory, suggesting the distortion of the lattice manifests itself in reciprocal lattice space, causing vectors to impinge upon the momentum pancake that would otherwise be excluded.

The rocking curve is shown in figure 3.21. This was acquired using a 0.25mm × 0.25mm beam of 1Å(12.5 keV) X-rays directed through the centre of the specimen and reflected from the {004} family of planes. The width is $\sim 500\mu$rad. It is seen that specimens exhibiting a broad rocking curve profile perform poorly in coherent bremsstrahlung experiments.

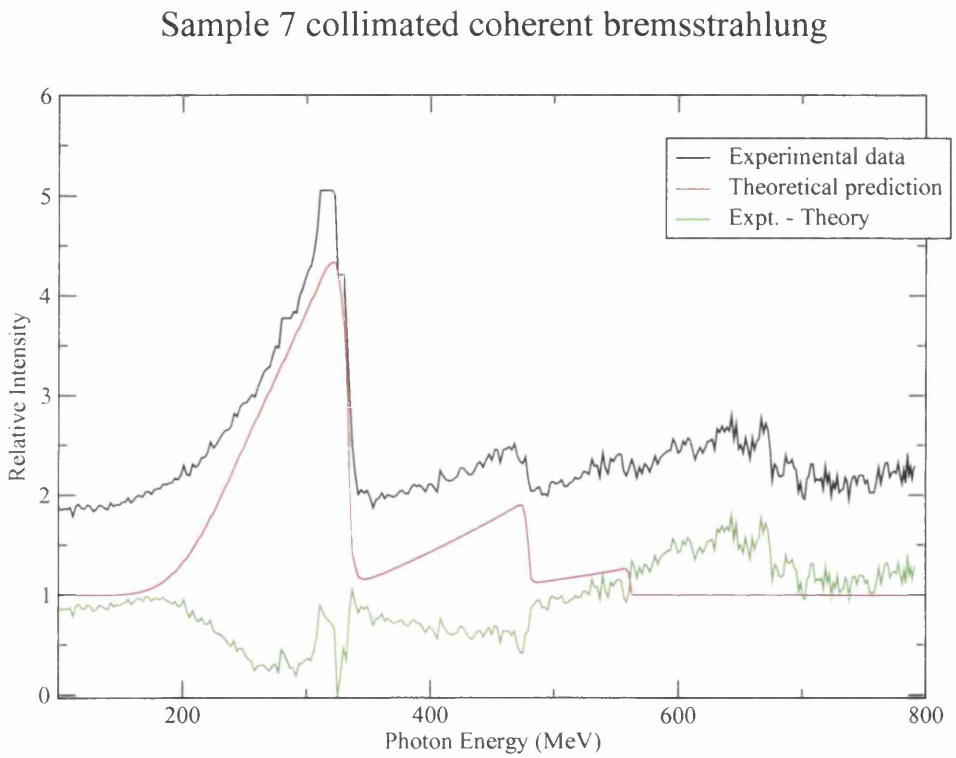

Figure 3.20: Coherent bremsstrahlung with collimation, showing theoretical prediction for sample 7.

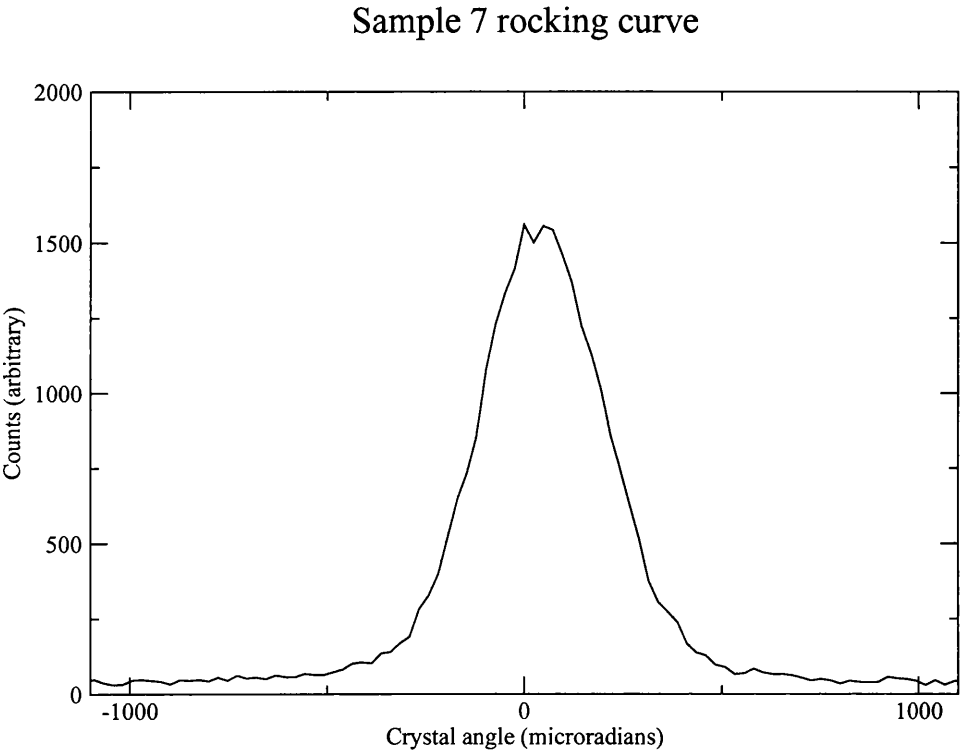

Figure 3.21: The rocking curve for sample 7.

3.5.8 Sample 8

In figure 3.22 the polarised light analysis, projection topograph and rocking curve of sample 8 are shown. The polarised light analysis acquired using petrographic microscopy is shown on the top left and shows the braided strain pattern composed of sheaves of line defects that are the result of plastic deformation. Below this image at the bottom left is the badly misshapen projection topograph. On the right is the rocking curve, acquired by using a 0.25mm × 0.25mm beam of 1.3Å(9.5 keV) X-rays directed through the centre of the specimen and reflected from the {022} set of planes. This shows again the correlation of a broad rocking curve (in this instance with $W_{meas} \sim 1000\mu$rad) with a poor projection topograph and polarised light analysis. The quality of the sample was so poor that it proved too difficult to align it in order to measure the coherent bremsstrahlung spectrum that could be obtained using it.

These results were reproduced using other identically specified samples, each showing plastic deformation, yielding topographs that failed to retain the shape of the sample and having very broad rocking curves.

3.5.9 Samples 9 to 12

Sample 9 to 12 were successive 100 μm cross-sections taken across the (100) plane from the same diamond, a synthetic type I specimen. Figure 3.23 shows the polarised light analyses of these successive slices are, placed in order to show progressively larger square "frames" (labelled as growth horizons in the image) whose sides correspond to the intersection of the cut plane, (100), with the $(111), (1\bar{1}1), (\bar{1}\bar{1}1)$ and $(\bar{1}11)$ planes. The red numbers painted on the samples are for reference only and have no effect on the diamonds interaction with X-rays

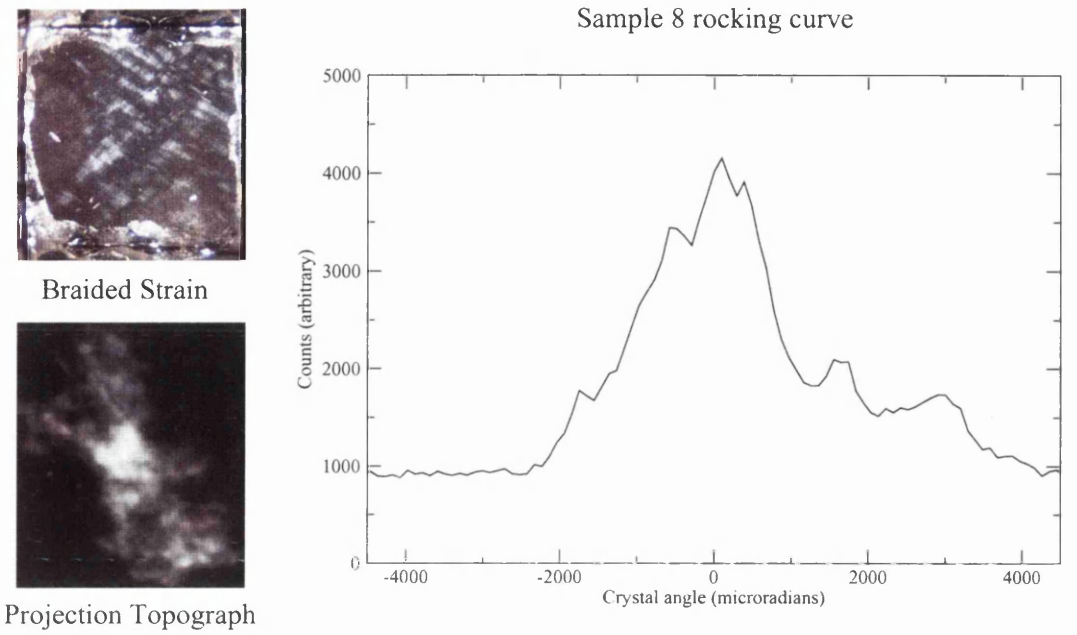

Figure 3.22: Polarised light analysis, projection topograph and rocking curve of sample 8.

or high energy electrons. The differential growth pattern that results from the energetically more favourable deposition of atoms preferentially on some planes, as the diamond grows around the seed, is manifested in the strain patterns seen in this sequence of images. The enlargement of this frame in successive cross-sectional images corresponds to octahedral growth.

The projection topographs of the samples, in the same order and oriented the same, are shown in figure 3.24. The same features are apparent in these images as were seen in figure 3.23. The aspect ratios vary due to foreshortening in reflection, caused by the inclination of the beam to the sample, and the use of asymmetric reflections in which the planes are not parallel to the surface. The concentration of line defects at growth horizons is caused by strain induced by differential growth rates on the crystal planes.

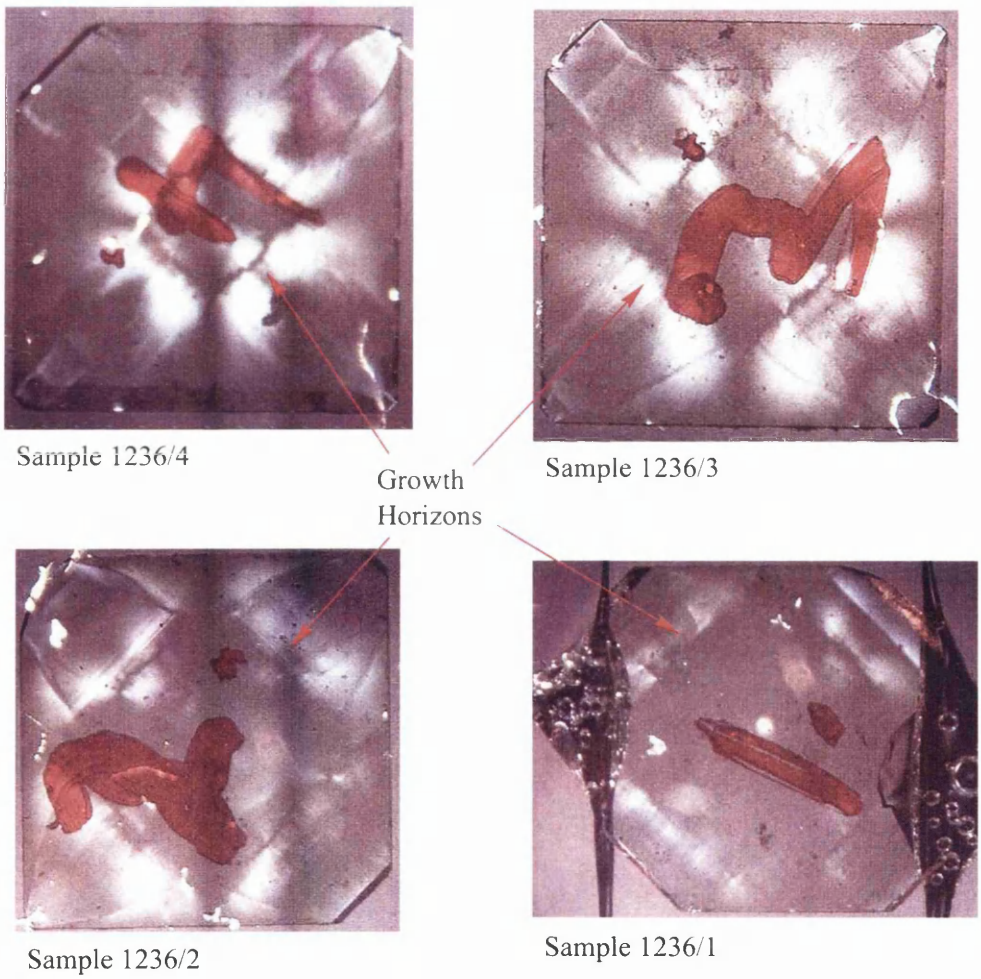

Figure 3.23: Petrographic microscopy of samples 9 to 12.

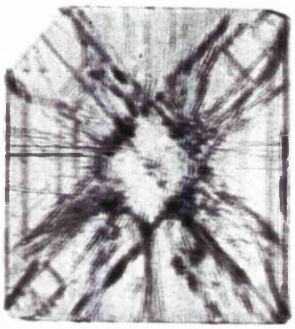

Sample 1236/4

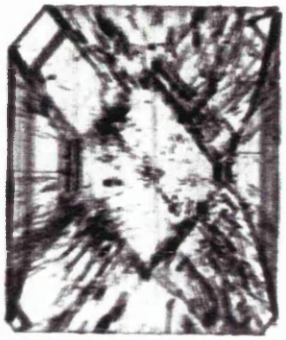

Sample 1236/3

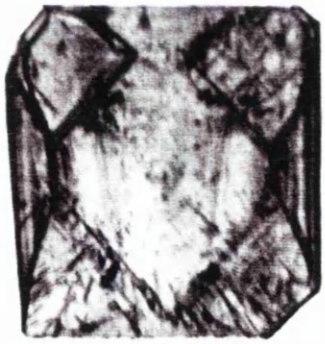

Sample 1236/2

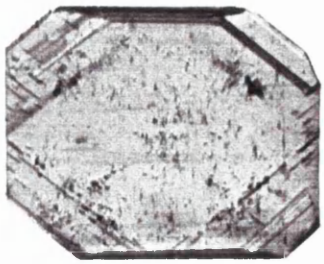

Sample 1236/1

Figure 3.24: Samples 9 to 12, projection topographs.

3.6 Conclusions

Contrary to received wisdom, it is seen that diamonds with a low nitrogen content, specifically type II diamonds, do not necessarily make the best radiators The consequences of plastic deformation dominate the behaviour of the crystals. The selection procedure to be used when presented with a candidate diamond for use in coherent bremsstrahlung experiments has been determined as a result of this study to conform to the following steps

1. Images of the candidate are acquired using a petrographic microscope and crossed polaroids which reveal local strain fields which impose orientational or dilational departures from ideal lattice conditions revealed by the local birefringence they cause. If the diamonds appear relatively strain free we proceed to step 2, otherwise the candidate is rejected.

2. Images of the diamond are acquired using X-ray topography which characterises the defects which are present in the crystal with greater precision. This is best achieved using a synchrotron radiation source. This is complementary to the procedure followed in step 1, and comparisons should be drawn between the results. If the topograph is not distorted and retains the shape of the sample without appearing to have a high defect density step 3 may be implemented.

3. A rocking curve of the sample should be obtained, using both a narrow beam of dimensions similar to the primary electron beam which would be incident upon it were it to prove suitable, and a broad beam which illuminates the whole sample, giving a quantitative measurement of the range of orientational and dilational deviations of the lattice which may result from

tilt boundaries and granularity. Locally favourable conditions may prevail at any given location of the narrow beam, but the direction of the lattice vectors may slowly vary through the entire volume of the crystal such that there may be a slight unpredictable misalignment dependent upon where the primary beam is incident on its surface. This is revealed if the whole crystal rocking curve is much broader than the narrow beam rocking curve.

It was concluded that plastic deformation causes damage of such a nature and extent to the diamond as to render it unsuitable for use as a radiator. The misshapen topographs and broad rocking curves indicate a broad range of alignments of lattice vectors and a variety of lattice parameters which would degrade a photon spectrum acquired through coherent bremsstrahlung, severely limiting the ability to gain a high degree of polarisation by imposing collimation. Degrees of polarisation of 70% or more can be obtained using collimation since this exploits the fact that the coherent part of the emitted spectrum is emitted into a smaller solid angle than the incoherent component. However, the misalignments of the lattice vectors evident in samples which have undergone plastic deformation compromise such directional effects and the extent to which they can be exploited. This problem is greater at higher primary electron beam energies, as the characteristic angle which describes the cone into which coherent bremsstrahlung is emitted is smaller at higher energies, having a $1/E_0$ dependence, while the range of angles at which the lattice vectors are oriented are independent of beam energy, and therefore dominate directional effects to a greater extent at higher beam energies. It is advantageous that a crystal which has undergone plastic deformation is easily recognisable using petrographic microscopy, therefore obviating the need to proceed with further, more laborious tests once encountered. Such samples can immediately be rejected at the stage of being identified using crossed polaroids. Plastic deformation occurs in type IIa diamonds, which were previously preferred

due to their low nitrogen content, however this study demonstrates that their behaviour is dominated by the plastic deformation rather than the nitrogen content. Indeed, it may be concluded that a reasonably high nitrogen concentration can be tolerated as it is associated with the growth of relatively more defect free lattices.

Once a good sample is found the additional expense of having its thickness reduced to improve the ratio of electron scattering angle to coherent bremsstrahlung characteristic angle is justified. The samples which were deemed most suitable on the evidence of this study were synthetics of type Ib.

Chapter 4

Radiation Damage

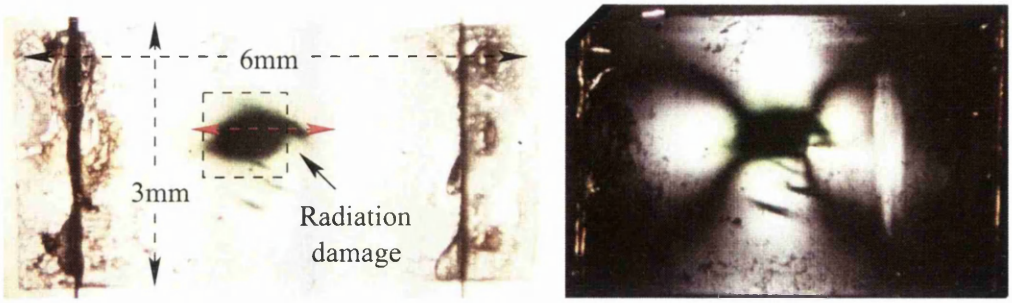

Figure 4.1: Petrographic microscopy of the radiation damaged sample.

4.1 Introduction

It is important to be able to ascertain the reasonable working lifetime of a sample in relation to coherent bremsstrahlung. The use of $\sim$ 1 GeV electron beams to produce photon beams using diamond radiators must eventually incur substantial damage to the crystal, causing extrinsic defects which may degrade the performance of the sample as a radiator. The nature of the irradiation occurs only in this application of diamonds and has not been studied at length previously. The majority of studies regarding radiation damage of diamonds are concerned with radiation characterised by energies of a few eV, whereas the application of diamonds this study is concerned with is characterised by energies of hundreds of MeV or a few GeV. In fact this is true of studies about diamond more generally - the interactions of interest to the diamond community are characterised by energies several orders of magnitude smaller than those typical of this study.

As a result of heavy usage, a severely radiation damaged sample was available for study in this respect. This sample, a 100 μm thick specimen cut across its (100) plane, has been irradiated by an 855 MeV electron beam running with a current of $\sim$ 30 nA for hundreds of hours, sufficient to expose it to a dose of $\sim 10^{21}$ 855 MeV electrons. This is predicted by Timm [5] to cause enough damage to begin to degrade the performance of the diamond as a radiator noticeably. A

wider survey of radiation damage incurred in photonuclear studies and its consequences would benefit from analysis of a range of samples irradiated by different beam energies and currents for different lengths of time. However, the availability of such specimens is limited by their generation through usage in photonuclear studies. In this chapter study is restricted to an analysis of the single sample which was irradiated during photonuclear experiments conducted in Mainz from 1994 until the present.

Petrographic photography, x-ray topography and rocking curve analyses were all used and the correlation of their results with the performance of the diamond as a radiator interpreted. This is a heavily used specimen which exhibits serious radiation damage in a central region roughly 1 mm square.

4.2 Petrographic Photography

The battery of tests applied in the previous chapter to ascertain the suitability of a specimen as a radiator were used. Initially petrographic exposures were taken with and without crossed polaroids. Figure 4.1 shows on the left the image acquired without crossed polaroids and on the right the image acquired using crossed polaroids showing the local birefringence caused by strain in the diamond. On the image on the left a central region is marked with a box. This region was surveyed using coherent bremsstrahlung, the results of which are given below. The red dashed line shows the range of locations at which rocking curves were acquired. The damaged region is immediately apparent due to the extreme discolouration caused by the density of defects. From the dark green hue of the specimen an estimate of defect density of a few sites per hundred lattice sites was made [34]. The shading of the discolouration shows that defects have diffused from the location in the diamond where they were formed - the $80\mu m \times 20\mu m$

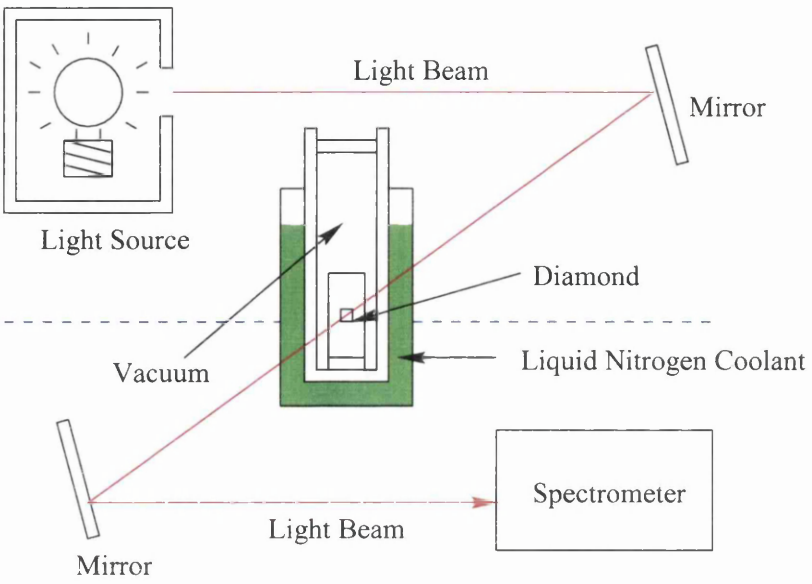

Figure 4.2: A schematic of the apparatus necessary for acquiring absorption spectra of diamond.

beam spot. The polarised light analysis indicates that the strain field in the crystal is centred on the radiation damaged area. A uniform strain field is revealed which has 4-fold symmetry. It is possible that the diamond had no strain prior to the damage, although it is impossible to determine the extent to which any previous strain field may have been modified by the damage.

4.3 Spectroscopic Techniques

A seemingly inexhaustible array of spectroscopic techniques can be deployed to characterise diamonds and identify the defects that inhere in them. Available expertise and equipment constrained this to the three used in this study, two absorption and one emission based technique. Initially the optical absorption spectrum was obtained, as seen in figure 4.3. Absorption in the infra-red was also

observed as illustrated in figure 4.4, and finally a cathodoluminescence spectrum was obtained (figure 4.5). However no spectra were acquired using an undamaged diamond for comparison.

4.3.1 Optical Absorption

The optical properties of diamond are dominated by the absorption of photons by defects. Absorption occurs as a result of electronic excitation of defects. However if the excited and ground states of the defect have different physical configurations within the lattice, vibrational modes become involved in the interaction of the light with what is termed a "vibronic" system, producing a sharp zero phonon line (ZPL) and a sideband corresponding to absorption due to electronic excitation plus the production of one or more phonons.

A diagram of the apparatus required for acquiring these absorption spectra is shown in figure 4.2. The sample is illuminated by a light source while held *in vacuo* and cooled to liquid Nitrogen temperatures. The transmitted light spectrum is measured by a spectrometer. The dashed blue line indicates the optical isolation of the two halves of the experiment to ensure that the results are not contaminated by extraneous light. Initially a background measurement is made, without the diamond in the light beam, to ensure that features observed in the diamond absorption spectrum are genuine. The spectrum of the light transmitted through the diamond is measured in a spectrometer. The mounting ensured that only the damaged region of the diamond was illuminated.

A peak is observed at 2.454 eV, which is interpreted as being due to the presence of Nitrogen. When vacancies are created as a result of irradiation, they can migrate and be captured by the A aggregate centres (pairs of substitutional Nitrogen atoms) in type IaA diamonds to form the H3 optical centre, with structure

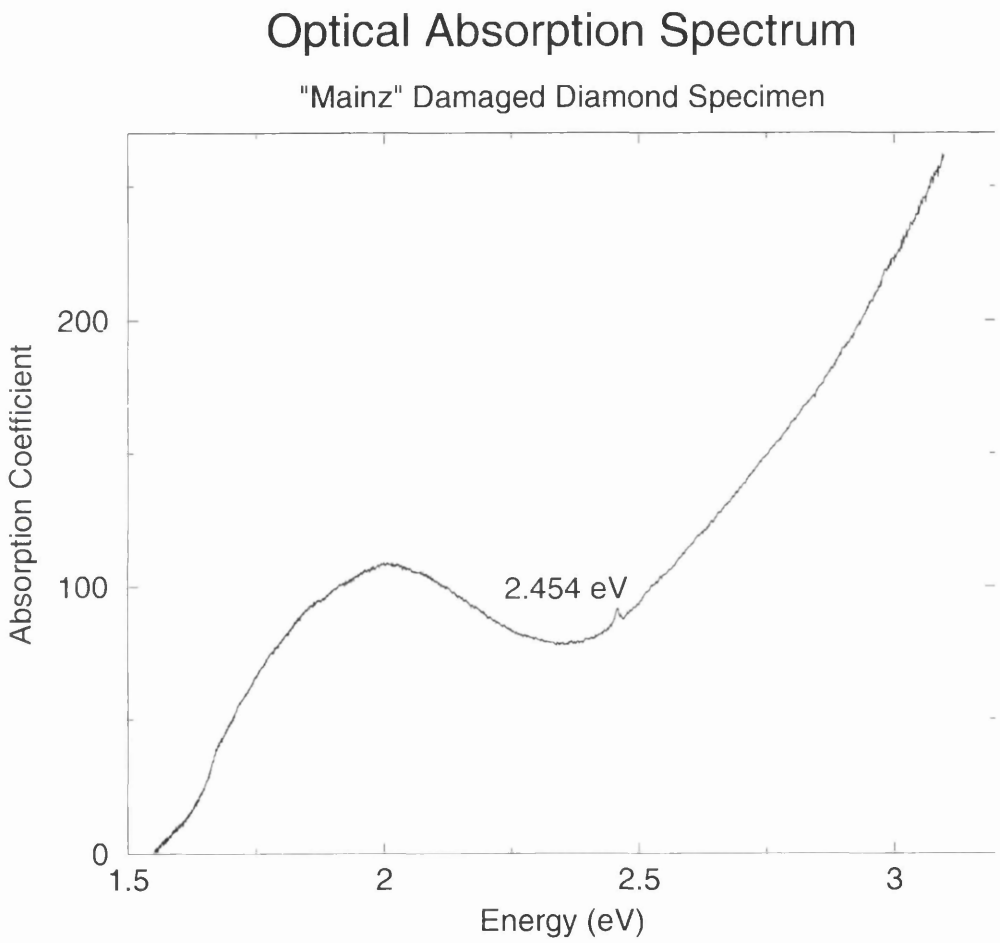

Figure 4.3: The optical absorption spectrum of the radiation damaged specimen.

N-V-N, which has a ZPL at 2.463 eV. However the history of this diamond was not thought to include the annealing which would normally be required to activate sufficient vacancy migration to produce this structure. Three substitutional Nitrogen atoms bonded to a vacancy produces a ZPL at 2.985 eV, and imparts a yellow hue. The formation of a complex consisting of a vacancy and a single Nitrogen atom due to irradiation would produce a ZPL at 2.156 eV in a negative charged state and a ZPL at 1.945 eV in the neutral state [35]. The B aggregate plus a vacancy produces a ZPL at 2.498 eV. Isolated vacancies are associated in their negatively charged state with a ZPL at 3.150 eV with an absorption sideband termed the ND1 band, and 1.673 eV in their neutral state, with a sideband termed the GR1 band. These vacancies may be generated by irradiation, with the ND1 absorption predominating until the boron acceptor impurity sites found in type Ib diamonds are fully compensated, and then proceeding with vacancy generation resulting in GR1 absorption after that. Self-interstitials due to irradiation would cause a ZPL at 1.685 eV. These ZPLs are not observed, and the most likely interpretation of the spectrum is that the line at 2.454 eV is associated with N-V-N structure, although vacancies are mobile in the lattice only at temperatures above 650°C and isolated substitutional Nitrogen atoms only above 1700°C, unless geological periods of times are concerned. This suggests that the sample underwent heating during irradiation.

4.3.2 Infra-red Absorption

A similar experimental setup as was used to acquired the optical absorption spectrum was used to obtain an infra-red absorption spectrum. This is shown in figure 4.4. The feature at around $2400cm^{-1}$ was due to absorption associated with water in the chamber, an imperfect vacuum having been achieved. The spectrum

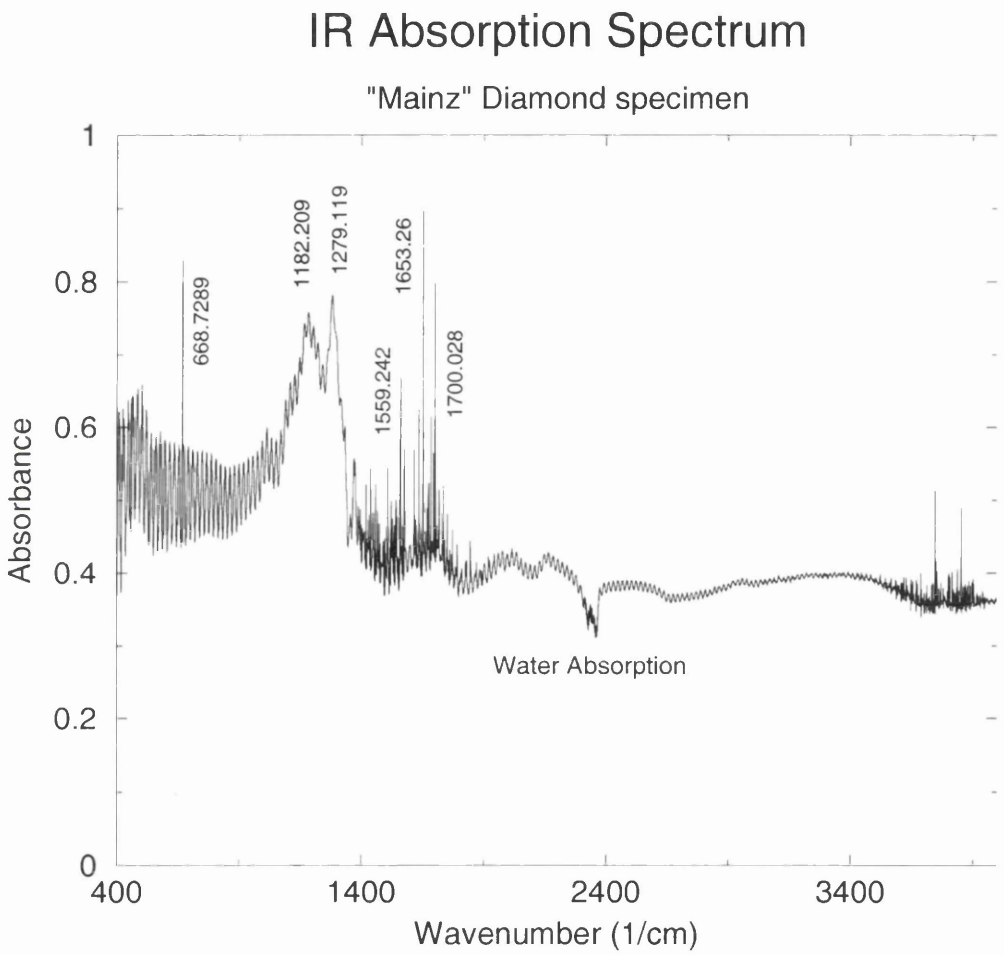

Figure 4.4: The infra-red absorption spectrum of the damaged specimen.

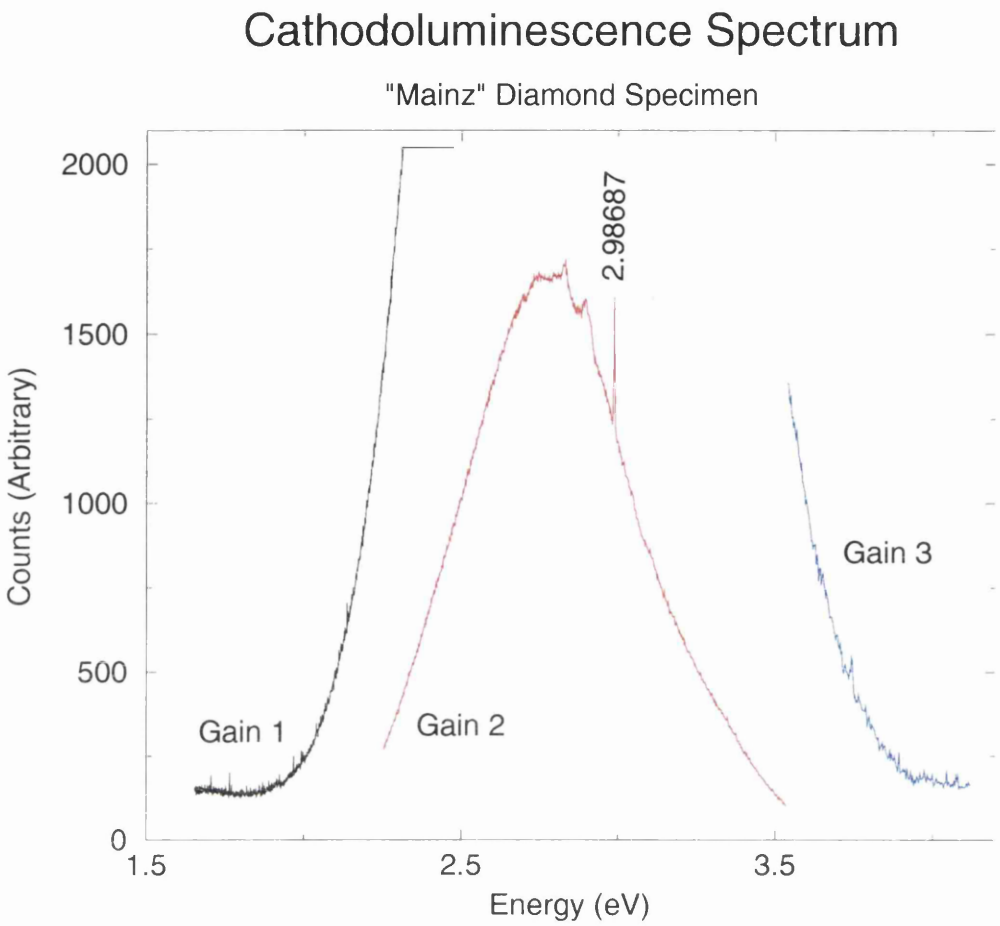

Figure 4.5: The cathodoluminescence emission spectrum of the radiation damaged specimen.

appears to be superimposed upon fringes caused by the thinness of the sample. Nevertheless features are prominent. Peaks are observed at $668.7289cm^{-1}$, $1182.209cm^{-1}$, $1279.119cm^{-1}$, $1559.242cm^{-1}$, $1653.26cm^{-1}$ and $1700.028cm^{-1}$.

Infrared absorption lines are caused by the excitation of vibrational modes of the defect. The highest frequency at which the diamond lattice can vibrate, the Raman frequency, has a wavenumber of 1332.5 cm^{-1}, and so defects producing absorption at higher frequencies do so through the excitation of local modes. Absorption due to single substitutional Nitrogen as would be expected with type

Ib synthetic diamonds would produce a peak at 1130 cm^{-1} and absorption due to a local mode at 1344 cm^{-1}, both of which are absent from the spectrum. The line corresponding to absorption caused by the presence of the charged Nitrogen ion N^{+}, expected at the Raman frequency of 1332.5 cm^{-1}, is also absent, although a barely perceptible rise occurs at 1331.19 cm^{-1}. Since this is near the Raman frequency little weight can be put on any interpretation of it, as it could be due to many other defects. The lines associated with A aggregates at 1282 cm^{-1} and 1212 cm^{-1} are also absent.

4.3.3 Cathodoluminescence

The diamond was again placed in a vacuum and cooled using liquid Nitrogen. Thermal and electrical contact was achieved by mounting the diamond using silver paint as an adhesive. A $\sim$ 40 keV electron beam was then directed onto the diamond to induce luminescence, whose spectrum was measured. There were more stringent demands on the apparatus as a lower concentration of contaminants is required to produce interpretable results than is the case in absorption based tests. Therefore a harder vacuum and larger liquid Nitrogen reservoir were used than was appropriate to the absorption tests. The luminescence occurs due to the excitation of electrons and holes which recombine radiatively when trapped at defects.

The gain of the photon detector used to record the spectrum was altered to accommodate the possibility of saturation, thereby acquiring the best possible statistics over the whole range of the spectrum, shown in figure 4.5. Three separate gain settings were used three in different energy ranges (shown with blue, red and black curves in the plot). The spectrum is typical of those obtained using synthetic diamonds, having a broader FWHM than would be obtained using a natural diamond. A sharp peak is observed, superimposed on the Gaussian shape

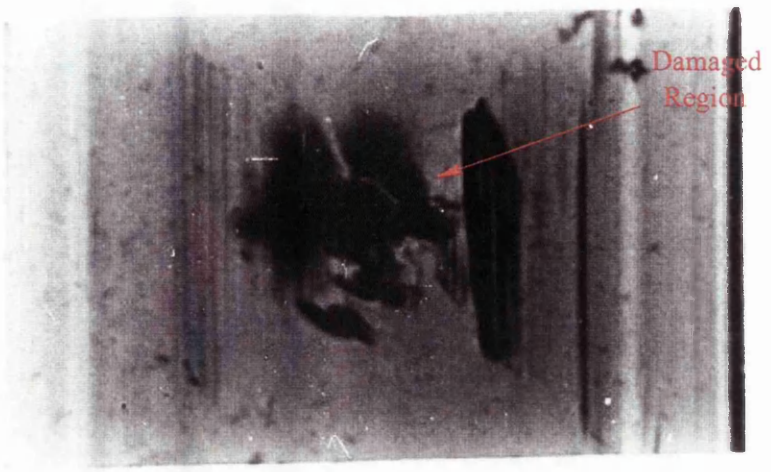

Figure 4.6: The projection topograph of the damaged sample.

of the curve on the higher energy flank, at 2.98687 eV, which is caused by the presence of nitrogen impurities in the diamond.

From the spectroscopic evidence available it was concluded that the Mainz specimen was a type Ib synthetic diamond with H3 centres in it. The spectroscopic evidence did not indicate any noticeable degradation resulting from irradiation, or any departure from the spectra that would be expected from a diamond not subjected to severe irradiation. There seem to be no features in these spectra that would not be expected to occur in the spectra of undamaged diamonds.

4.4 X-ray Topography

In figure 4.6 the projection topograph obtained by illuminating the whole crystal in a white X-ray beam is displayed. The region which has sustained the radiation damage is clearly visible. A pattern similar to growth horizons is seen to frame the damaged region, suggesting that the strain incurred in the lattice by the damage and the associated defect density has exceeded some threshold resulting in the

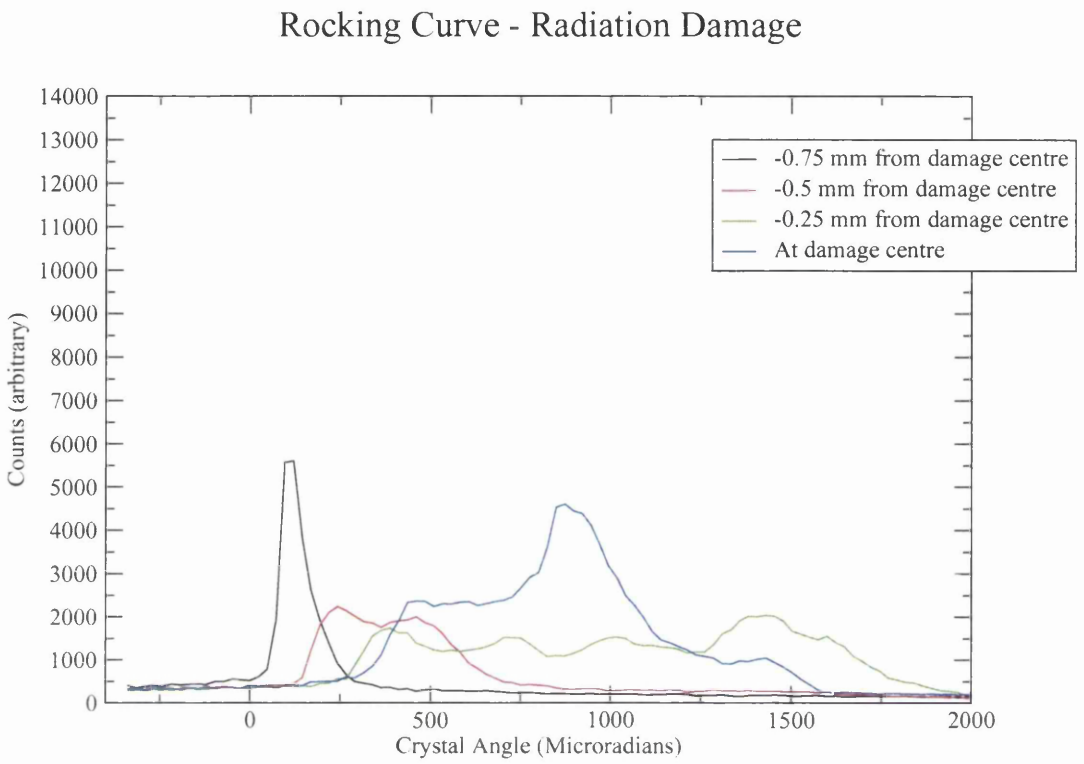

Figure 4.7: Four rocking curves taken at four successive points along a path that traverses the damaged region of the sample.

formation of these boundaries. The dilational strain caused by the high density of vacancies created by the electron beam which has produced the radiation damage may have induced a relaxation in the lattice at these boundaries.

4.5 Rocking Curve Analysis

Given the localised nature of the damage in the region of the diamond onto which the beam has been directed, a series of rocking curves were taken traversing this region. The points at which rocking curves were measured lie on the red line shown on the left hand image on figure 4.1. The rocking curves are shown in figures 4.7 and 4.8. Negative values of distance from the damage centre quoted

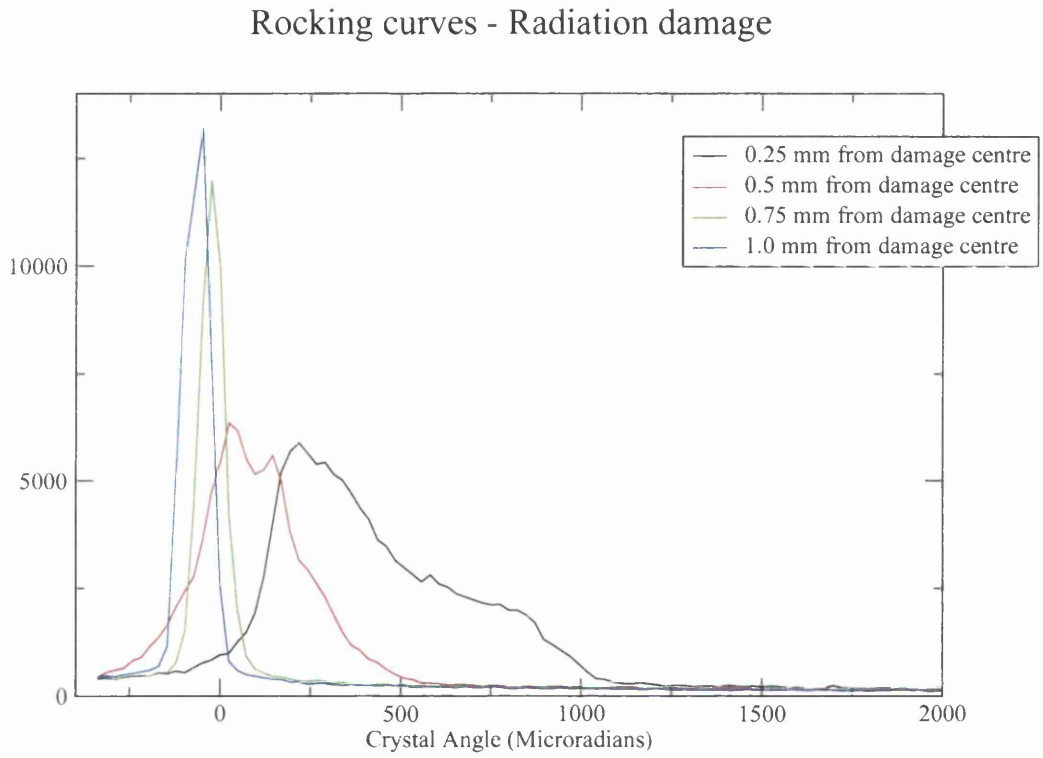

Figure 4.8: Rocking curves taken at the next four steps along the path which traverses the damaged region of the diamond.

relate to points to the left of the damage centre on the image, and positive values refers to points to the right of the damage centre. Figure 4.9 shows the information plotted on the eight plots in the previous two figures set against each other as the damaged area is traversed.

The rocking curves were acquired at locations 0.25mm apart, using a 0.25mm × 0.25mm X-ray beam with a square profile. The 1ÅX-rays were reflected from the {004} set of planes. It was found that the radiation damage was associated with a dramatic broadening of the rocking curve profile. The rocking curve obtained in an undamaged region of the diamond was close to ideal, as is seen in figure 4.10. The FWHM is 19.2μrad, which compares favourably with an ideal theoretical minimum of 5.4 μrad.

4.6 Coherent Bremsstrahlung Spectra

A series of coherent bremsstrahlung spectra were acquired by directing the electron beam delivered at Mainz through a region of the diamond, illustrated in figure 4.1 enclosed in the black 1mm × 1mm dashed box, in an attempt to ascertain whether there was any degradation in the performance of the specimen as a radiator which could be correlated with the radiation damage. This would help indicate the viable lifetime of diamonds as radiators.

The diamond was inserted into the goniometer at Mainz and aligned using the Stonehenge technique described in chapter 2, using the 855 MeV electron beam delivered there. The translational axes of the goniometer are Z and X as outlined in chapter 2. A grid of points spanning the damaged region were selected to investigate whether there was any appreciable variation in the coherent spectra acquired by directing the beam through the region of the diamond at those points

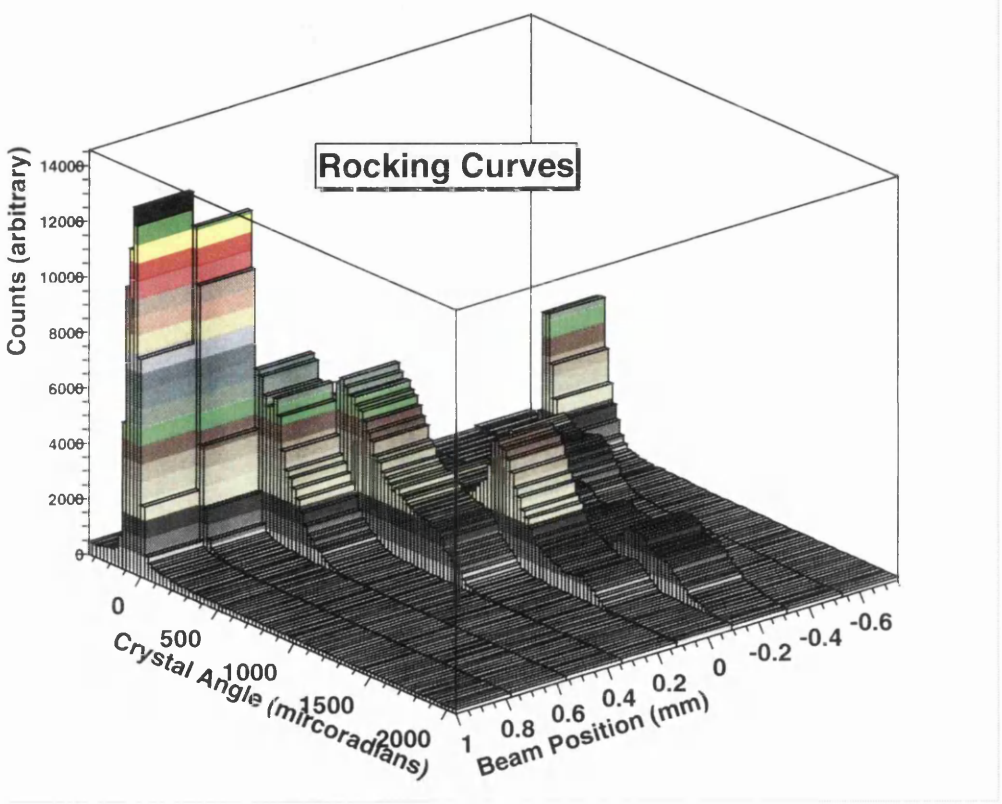

Figure 4.9: A plot showing the dramatic broadening of the rocking curve that occurs as the rocking curve survey of the diamond sweeps through the radiation damaged region.

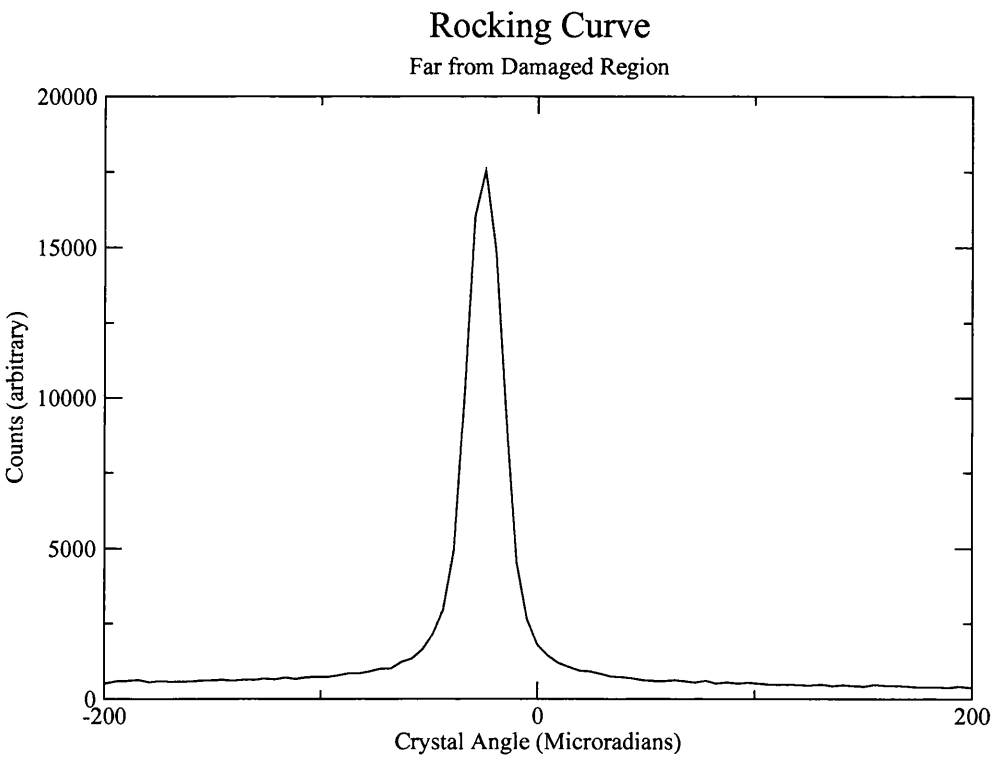

Figure 4.10: The rocking curve in the undamaged region of the crystal.

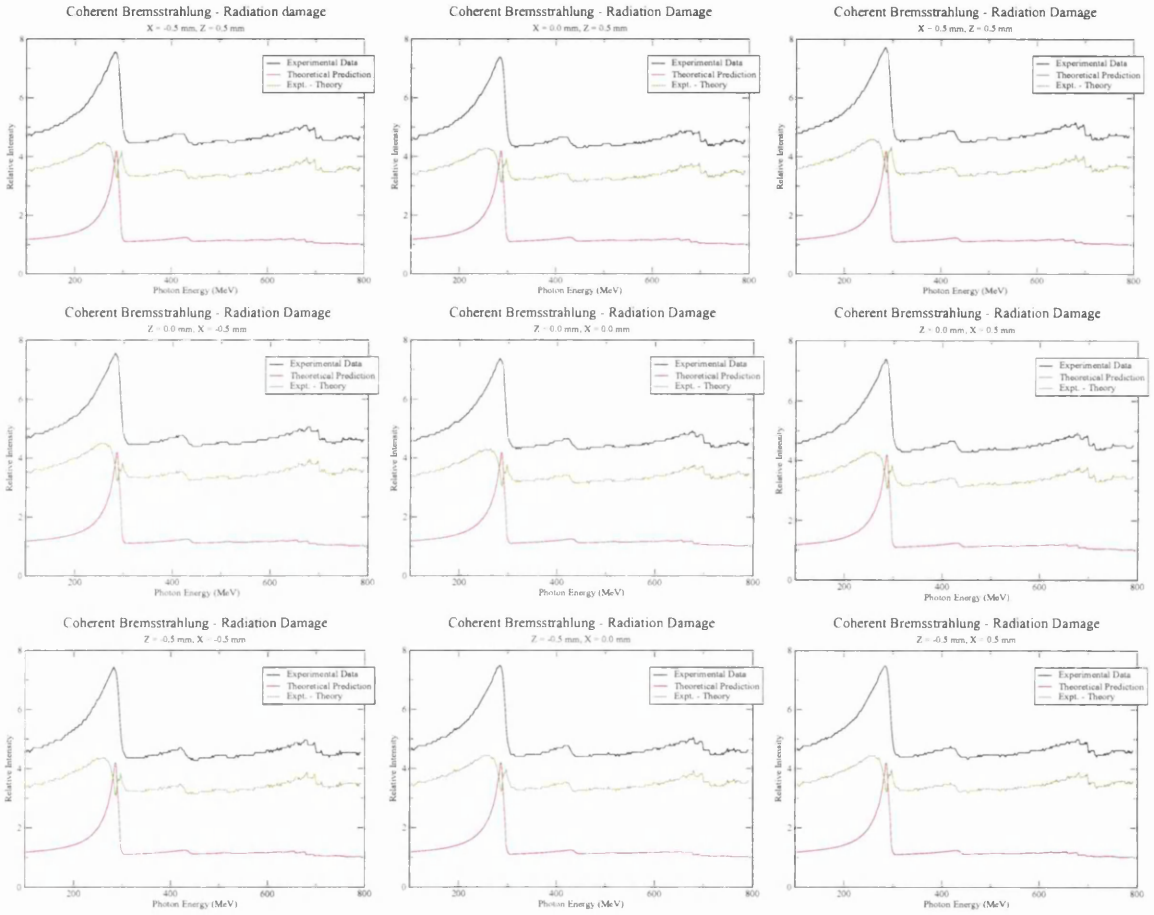

Figure 4.11: Coherent bremsstrahlung spectra taken at different points on a 1mm × 1mm grid that spans the damaged region.

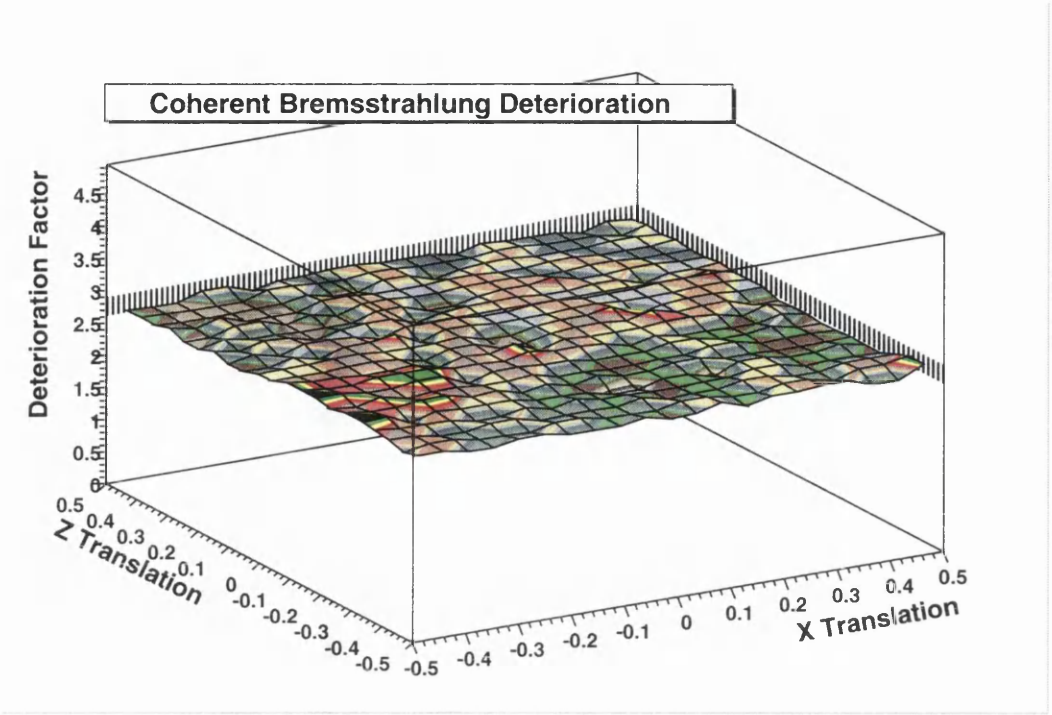

Figure 4.12: The deterioration in coherent spectra in the damaged region of the diamond.

due to the radiation damage. A 1 mm × 1 mm grid was chosen such that the Z = 0mm, X = 0mm position corresponded to the centre of the damaged region. Positive values of Z relate to points above this in figure 4.1, while positive values of X refer to points to the right of this in figure 4.1. The coherent spectra obtained were those produced with the sample rotated about the vertical goniometer axis by 10 mrad and about the horizontal axis by 60 mrad and are shown in figure 4.11. These plots were normalised as previously in chapter 3. The theoretical width of the coherent edge seen at 300 MeV is 9 MeV. The experimental width is found to be 30 MeV.

It is seen that the experimental relative intensity data includes an enhanced component that does not contribute to the theoretical plots. This additional background appears at all energies and is deemed to be incoherent and due to

the radiation damage. In figure 4.11 the experimental data is shown in black, the theoretical data in red and the difference between the two in green. Experimental data was acquired in the damaged region at X and Z increments of 0.05 mm. For each of these points the extra component, $I_{rel}^{expt.} - I_{rel}^{theory}$, was added for all energies and divided by the total theoretically predicted emission at all energies to give a factor which could be used to characterise the deterioration of the coherent bremsstrahlung due to the radiation damage. This factor is defined as

$$\alpha = \frac{\int_{energy}(I_{rel}^{expt.}(E) - I_{rel}^{theory}(E))dE}{\int_{energy} I_{rel}^{theory}(E)dE}$$

This is shown in figure 4.12. It is found to be remarkably uniform over the damaged region, and was equal to 2.8. The uniformity of the value of this factor can be see as due to two things. Damage was incurred at all points in the region surveyed due to the primary electron beam being directed through different parts of it on different occasions. Also, the defects that resulted from the damage will have migrated throughout the region. This is in agreement with the optical spectroscopic data which indicated that vacancies that had arisen due to irradiation had migrated combine with A aggregate centres to form H3 optical centres.

This deterioration factor can be considered to be the extent to which the linear polarisation of the experimental coherent bremsstrahlung has been degraded by the inclusion of the damage related incoherent component.

These results were reproduced with the horizontal rotation set to 10 mrad and the vertical rotation set to 60 mrad. This results in generating the spectra by emission from electrons scattered off planes perpendicular to those the electrons were scattered off in figures 4.11 and 4.12. This was done to ascertain whether the selection of reciprocal lattice vector would influence the results, which was found not to be the case. The azimuthal rotation was set at its default for coherent bremsstrahlung of 45% and was not adjusted since the symmetry of the crystal is

four-fold. The results were also reproduced after rotating the crystal about the the vertical axis to 60 mrad and about the horizontal axis to -15 mrad.

4.7 Conclusions

It was seen that spectroscopic techniques did not reveal compelling evidence of radiation damage incurred in a diamond as a result of use as a radiator in coherent bremsstrahlung experiments. The spectroscopic techniques are sensistive to defects which the coherent bremsstrahlung is not sensitive to, and *vice versa.* The cathodoluminescence results indicated that the sample under investigation was synthetic in origin. The spectroscopic techniques were not deemed to be good indicators of the occurrence of significant radiation damage.

However it was apparent from the deterioration of the coherent spectra that such damage had occurred and degraded the confidence that could be held in the degree of linear polarisation obtainable from such specimens. It was seen that the damage did not result in a significant broadening of the coherent edge. However the incoherent background was greatly enhanced so as to limit the degree of linear polarisation obtainable. In the case of the sample studied here the linear polarisation was 2.8 times less than that obtainable in theory.

While the coherent edge retained a profile that closely matched that predicted by theory, this in itself was not seen to be a sufficient reason to hold confidence in the degree of linear polarisation represented by the edge, since the incoherent background was seen to be uniformly enhanced at all energies, thereby degrading the degree of linear polarisation. The damage is not manifested most prominently as a broadening of the edge since the variation in the orientation of crystal lattice vectors as evidenced by the broadened rocking curves nevertheless does

not exceed the characteristic angle for coherent photon emission of $\sim 600\mu$rad. The damage is manifested most prominently as an enhancement of the incoherent background at all energies, causing a corresponding deterioration in the degree of linear polarisation. Nevertheless the diamond retains a sufficiently ordered crystal structure to produce prominent coherent phenomena.

Chapter 5

Channeling Effects

5.1 Introduction

A crystal axis or plane can be modeled as consisting of a continuum of charge, rather than as a set of discrete charges arrayed in a row or a sheet, as has been described in chapter 1. The potential well associated with the axis or plane can trap the particles of an incident primary electron beam in a trajectory which is governed by the direction of the axis or plane if the angle between the beam and the axis or plane is sufficiently shallow to prevent the electrons from having enough kinetic energy transverse to the potential to traverse it. The electrons become bound and travel along the direction of the axis or between planes. Relativistic contraction of the axis or plane renders the continuum approximation more accurate at higher beam energies. Electrons undergoing this interaction of correlated collisions governed by the lattice are said to be channeled.

The angle which characterises channeling is the Lindhard angle, or critical angle for channeling, Ψ_L, which is the angle between the electron beam and the crystal axis below which the electrons have insufficient transverse kinetic energy to escape from the string continuum potential, such that channeling occurs [36]. It is given by the expression

$$\Psi_l^{axial} = \sqrt{\frac{2Z_1 Z_2 e^2}{E_0 d}}$$

in the case of axial channeling, where d is the distance between atoms along the string of atoms on the axis, Z_1 and Z_2 are the charges of the nuclei and the projectile (in this case an electron), and E_0 is the primary beam energy. $e = 3.795 \times 10^{-3}\sqrt{MeV\mathring{A}}$ and in the case of axial channeling along the [100] axis $d = a$, the distance between the atoms on the axis, whereas along the [110] axis $d = a/\sqrt{2}$. $Z_1 = 6$ and $Z_2 = 1$ and the primary beam energy is 855 MeV. In diamond $a = 3.567\mathring{A}$. This gives $\Psi_L^{[100]} = 238\mu$rad and $\Psi_L^{[110]} = 283\mu$rad. This is an order of magnitude greater than the beam divergence of the electron beam

Planar Channeling Lindhard Angles	
Plane	*Lindhard Angle (μrad)*
(100)	185
(110)	220
(210)	124
(211)	19
(111)	281

Table 5.1: Critical Angles for Planar Channeling.

used for this study.

For planar channeling the critical angle is

$$\Psi_l^{planar} = \sqrt{\frac{4Z_1 Z_2 e^2 N d_p C a}{E_0}}$$

where d_p is the distance between the planes, $C \simeq \sqrt{3}$ and N is the number density of atoms, which for diamond is $N = 1.54 \times 10^{22} cm^{-3}$ (or $N = 1.54 \times 10^{-2} \mathring{A}^{-3}$). The Lindhard angles for planar channeling for significant diamond planes are shown in table 5.1.

As the electrons are accelerated in this potential they radiate channeling radiation [37]. Many studies of this phenomenon have been made ([38, 39, 40, 41, 42, 43, 44, 45, 46, 47, 48] and others). However it was deemed that there was a deficiency in the literature with regard to the energy regime that prevails at the coherent bremsstrahlung facility where this study was conducted. At low electron beam energies of a few MeV the electrons radiate by making transitions between discrete energy levels within the two dimensional (in the case of axial channeling) or one dimensional (in the case of planar channeling) potential well defined by the continuum potential. However, as this potential well is deepened by the relativistic contraction of the axis or plane in the electron rest frame at higher

beam energies, the number of electron transverse energy levels is multiplied until the spectrum becomes a continuum. The discrete spectrum that occurs at lower incident beam energies has been well studied, as has the continuum spectrum observed at energies of a few GeV. There is a dearth of material concerning the region of a few 100 MeV to 1 GeV.

The main motivation of this study is not to address this dearth *per se* but to investigate the utility of channeling radiation as a source of photons in photonuclear studies. To that end more information is required than has been available in the literature, specifically, the number of variables recorded requires to be greater. Although previous studies have measured the angular distribution of the photons, the angular distribution of the emergent electrons, the energy spectrum of the radiation and the angle of the crystal with respect to the beam at which the radiation phenomena associated with channeling occur, these variables have not previously been recorded in combination. In particular, in investigating the utility of channeling radiation as a photon source for use in photonuclear physics, it is necessary to ascertain the angular distribution of the photons in combination with their energy spectrum and the crystal angle in order to discover whether there is a feature in the energy spectrum which can be usefully enhanced by collimation. To this end the spectrum of photons emitted due to electron scattering processes in diamonds at a range of angles which included those which satisfied the channeling criteria were acquired. The measurements could be restricted to the spectra of those photons emitted into a particular solid angle by tagging them and applying collimation to the photon beam before their detection down beam from the diamond.

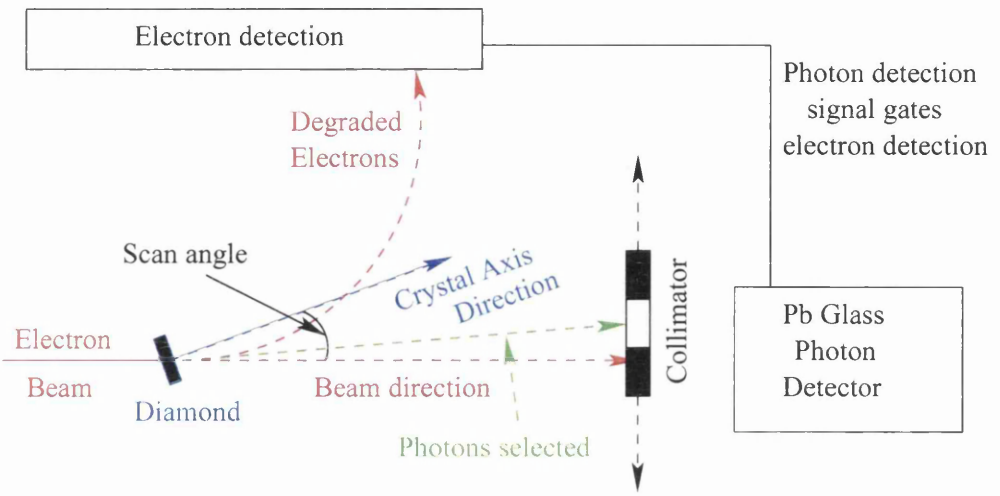

Figure 5.1: A schematic representation of gating the scalers.

5.2 Experimental Apparatus and Methods

The electron beam was delivered to the sample as described in chapter 2. The experiment was set up to run in two distinct modes,

1. If information about the directions in which the photons were emitted was not required, they were not detected and their spectrum was deduced entirely from the residual energies of the degraded electrons.

2. The photons contributing to the measured spectra could be restricted to those emitted in a certain direction by collimating the photon beam and then limiting those electrons contributing to the accumulation of a spectrum to those associated with a detected photon. The photons were tagged.

In the second case, the scalers which accumulated the counts in each of the electron energy channels of the spectrometer were gated by the detection of a photon. The collimator and photon detector constitutes a single pixel the signal from which is used to gate the scalers. This collimator could be placed on or off the beam axis to select the direction of photon emission being investigated. This

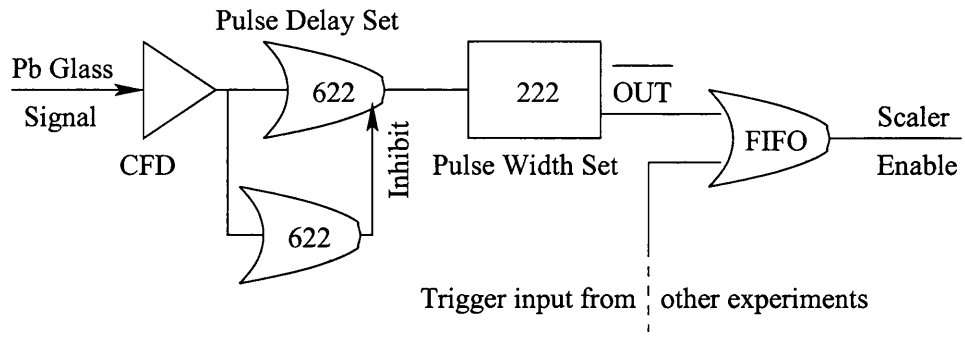

Figure 5.2: A schematic representation of gating the scalers.

is shown in figure 5.1. The electron beam and the degraded electrons are shown in red. The scan angle between the direction of the crystal axis and the primary electron beam direction is the angle which is varied incrementally with a spectrum acquired at each step. When the crystal axis direction is aligned with the beam direction to within the Lindhard angle, channeling occurs. When running in mode 2, the collimator can be placed in one of a range of positions to select a given direction. The detection of photons emitted in this direction can be used to gate the scalers so that they only accumulate counts for electrons associated with photons emitted in this direction.

The collimator was located 2.51m from the crystal radiator, such that a 2.5mm collimator was roughly equivalent to restricting the photon emission investigated to those emitted into a 1mrad cone. Its default position lay on the beamline, but it could be offset above the line of the beam direction by propping up either end with shims of different thicknesses. A Pb glass scintillator was used as the photon detector whose output was used to gate the spectrometer scalers. The trigger which enabled the gating of the scalers with this signal is shown in figure 5.2. The signal from the scintillator is input into a constant fraction discriminator (CFD), whose output is input into a LeCroy622 which sets the delay of the signal in order to make it enable the scalers to accumulate when the electron associated

with the detected photon is registered. This is inhibited by a second 622 which is set to output a pulse of 300 ns width as a window in which the first 622 can output a pulse. This is installed to veto reflections. The delayed pulse has its width set to 65 ns by a LeCroy222, whose $\overline{OUT}$ is input into a FIFO (Fan In Fan Out) into which all signals for enabling scaler accumulation are entered.

This setup has the disadvantage of restricting the information pertaining to the angular distribution of the photons to only those photons emitted into the solid angle subtended by the collimator, but has the advantage of allowing the rapid accumulation of excellent statistics, and the added advantage of practical simplicity, since data acquired with more than one pixel would have to be handled on an event-by-event basis (It could be argued this is making a virtue of necessity).

The diamonds were aligned using the Stonehenge technique referred to in chapter 2, and the zero offsets found, such that goniometer angles coincided with crystal angles relative to the beam. Once this was done the orientation of the crystal with respect to the electron beam could be incremented through a range of angles which included those satisfying the criteria for channeling, and a photon spectrum could be acquired at each step according to which of the above two modes was being operated. These spectra were plotted as a surface representing the relative intensity of photon emission displayed by energy and crystal angle. This process was termed a scan.

The normalisation scheme employed previously in plotting coherent bremsstrahlung spectra has often hidden the channeling contribution. Scans performed to investigate coherent bremsstrahlung at various angles have conventionally been normalised by making constant the relative intensity at an energy at which coherent phenomena do not occur in the angular range surveyed. Since channeling phenomena are predicted to occur at all photon energies, these will not have been seen in these scans because they will have been normalised away. The beam was

deemed stable enough to allow the former normalisation scheme to be dispensed with.

It was recognised that multiple emission may occur from a single channeled electron. This would have the consequence of producing spurious high energy features in the spectrum, as a single degraded electron would have all the energy lost by it attributed to a single photon regardless of whether multiple emission had occurred, unless each photon is resolved, and a photon detector with an at least crude energy resolution would ensure cases of multiple emission were identified and handled appropriately. Data acquired without the angular distribution of the photons being determined in this study neglects to address this issue, as the photons are not detected, only the residual energy of the degraded electrons. Data acquired using collimation and a Pb glass photon detector to impose a degree of angular resolution on the results do not address this issue as the possibility exists that multiple emission could occur into a part of the photon angular distribution not sampled.

5.3 Channeling Radiation Results

Three diamond specimens were used to perform 9 scans. The diamonds used are listed in table 5.2. They are allocated a sample number and the name by which they were customarily known is listed. The axis along which channeling is observed is listed, and it is this axis which makes the angle with the primary beam which is incremented during a scan. The thickness is also listed.

Table 5.3 lists the 9 scans which were performed in the course of this study of channeling radiation. The column labeled Coll. shows the diameter of the collimator, if collimation was applied. The column labeled Offset shows the amount

Channeling radiation samples			
Sample	*Name*	*Axis*	*Thickness (μm)*
1	Mainz	[100]	100
2	dBb	[100]	< 18
3	Bonn C	[110]	120

Table 5.2: The samples used in channeling experiments.

by which the collimator was raised above the beamline. 1.5mm corresponds to 0.6 mrad and 1 mm corresponds to 0.4 mrad subtended at the diamond by these dimensions of collimator situated 2.5m from the samples. H denotes the angle the crystal was set at about the horizontal rotation axis (varying this directs the crystal axis above or below the beam line). V denotes the vertical rotation (varying this directs the crystal axis to the side of the beam line). A denotes the azimuthal angle, which is conventionally set at 45° during coherent bremsstrahlung experiments. A range of values is quoted in the column corresponding to the rotation varied during a scan, the scan angle. The scan angle was incremented by 0.1 mrad during a scan. This is slightly higher than the limit set on resolution by the electron beam divergence of 80μrad.

Table 5.4, summarising the observed angular widths of channeling peaks and comparing them with the Lindhard angles of the associated planes or axes, is included after the results for each scan are detailed.

Figure 5.3 shows the scan geometries for the [001] specimens. The beam is directed into the page. The traces of the crystal planes are shown in dashed black lines, intersecting at the [001] axis, which is directed into the page. As the crystal angle relative to the beam is incremented the position of the beam moves along a red line. The position at which the scan angle is such that the crystal axis is

Channeling radiation scans						
Scan	*Sample*	*Coll. (mm)*	*Offset (mm)*	*H (mrad)*	*V (mrad)*	*A (degrees)*
1	1	-	-	-5 to 5	0	45
2	1	-	-	-5 to 5	5	45
3	1	1.5	1	-5 to 5	0	45
4	1	1.5	1	-5 to 5	5	45
5	2	-	-	-5 to 5	0	45
6	2	-	-	-5 to 5	5	45
7	2	-	-	-5 to 5	0	55
8	3	-	-	0	-5 to 5	45
9	3	-	-	0	-5 to 15	47

Table 5.3: The channeling scans performed.

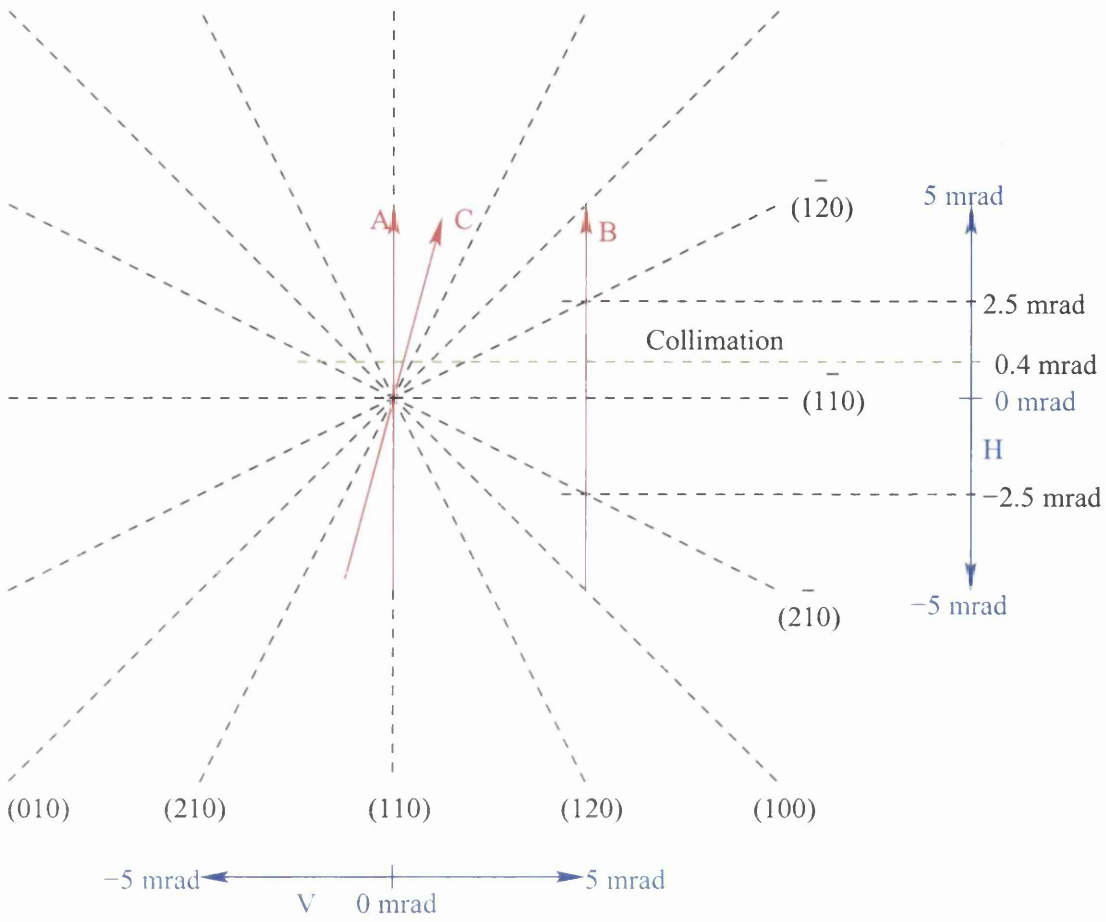

Figure 5.3: Scan geometry for [001] axis specimens.

directed in the direction of the offset collimation is shown as a green dashed line, that is, in the space represented in this diagram, the collimation is located at the point where the dashed green line intersects the trace of the (110) plane. Scans 1, 3 and 5 move the beam along line A in relation to the axis. Scans 2, 4 and 6 scan the beam along line B. Scan 7 moves the beam along line C. Dashed black lines show on the angular scale on the right hand side of the diagram where path B crosses crystal planes, that is, the angles at which the beam is aligned with these planes.

Scans 1, 3 and 5 were devised to investigate axial [001] channeling, with offset collimation applied in scan 3 and a thinner sample used in scan 5. Scans 2, 4 and

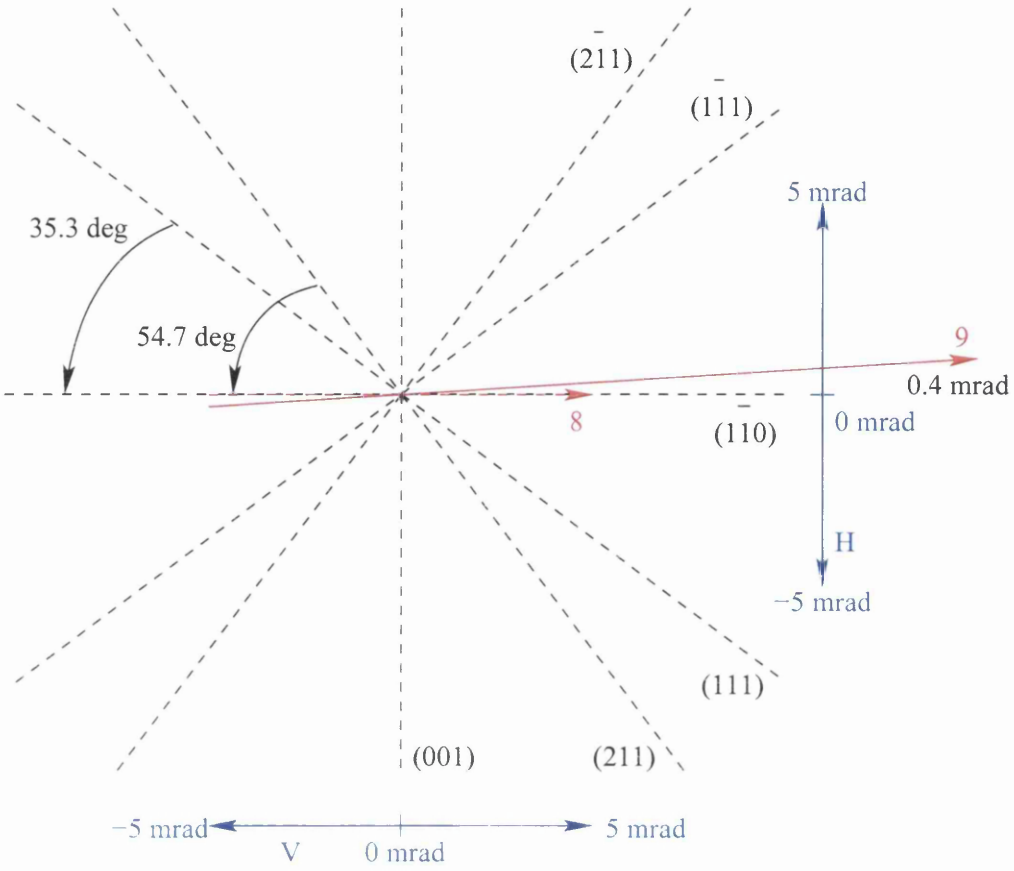

Figure 5.4: Scan geometry for [110] axis specimens.

6 are concerned with planar channeling from the $\{1\bar{1}0\}$ planes, with collimation applied in scan 4 and a thinner sample used in scan 6. Scan 7 investigated axial channeling with an azimuthal offset of 10° applied to ensure that there was no planar channeling from the {110} planes when the angle between the beam and the axis was not within the axial channeling regime.

Figure 5.4 shows the scan geometries for the [110] specimen. The crystal planes are again shown in dashed black, with the [110] axis directed into the page where they intersect. The positions the beam is scanned through relative to the axis is shown in red for scans 8 and 9. Scan 8 investigates axial channeling, while scan 9 has an azimuthal offset of 2° to eliminate the contribution of planar channeling outside the axial channeling regime of angles. This scan reveals a ridging phe-

nomenon also seen in scan 6 and described below. The [110] axis is seen to have two-fold symmetry, compared with the four-fold symmetry of the [100] axis. Comparisons are made below between the observed widths of channeling phenomena in terms of the range of crystal angles within which they occur, that is, the number of scan increments that are required to see the phenomena, and the Lindhard angles for channeling on the specific plane or axis being investigated as listed at the beginning of this chapter. This is because the Lindhard angle describes the the amount the angle formed between the crystal feature (a plane or an axis) may deviate from perfect alignment while still remaining within the channeling regime, that is, while still forming a sufficiently small angle for channeling to occur. This angle is what is varied during the course of a scan and so the observed response in terms of variation in photon beam intensity is directly related to the Lindhard angle. The value of the widths quoted below for the channeling peaks are the σs of the Gaussian fits made to the experimental peaks. The scalers were gated when collimation was applied, as in scans 3 and 4. Otherwise they were ungated.

5.3.1 Channeling on the [100] Axis - Sample 1

Scan 1

The surface which plots relative instensity against photon energy and crystal angle for scan 1 is shown in figure 5.5. Figure 5.6 shows the intensity integrated over all energies between 500 MeV and 791 MeV plotted against crystal angle. The prominent peak apparent in figure 5.6 is not obvious in figure 5.5 since the coherent peaks sweeping down in energy as the crystal angle approaches zero are the dominant features. The channeling in figure 5.6 was fitted with a Gaussian

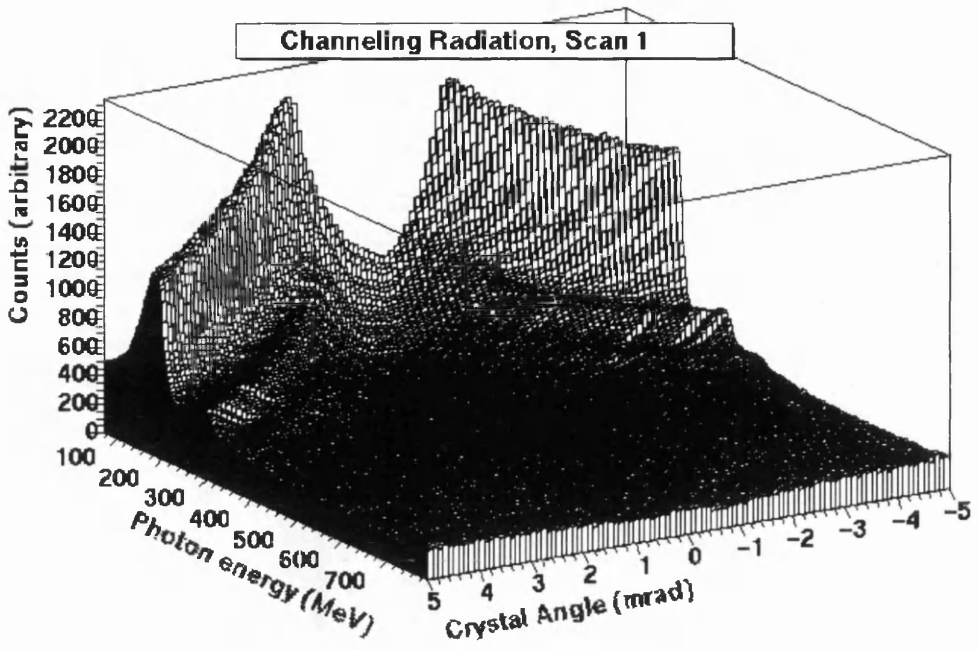

Figure 5.5: Scan 1.

and found to have $\sigma = 325\mu$rad and a FWHM of 765μrad, which is over three times the Lindhard angle of 238 μrad. The broadening may be related to the radiation damage this specimen has experienced. The rocking curve of this specimen was seen to have been markedly broadened in the previous chapter.

Figure 5.6 shows the intensity to drop to a minimum on either side of the central channeling peak, at angles of -0.8 mrad and 0.8 mrad. $I_{rel.}^{max}/I_{rel.}^{min} = 1.25$ in the neighbourhood of this peak. At angles further from the peak the intensity begins to rise again. This was interpreted as being due to planar channeling, since the beam is directed along the (110) plane at all points in the scan. The minima are then seen to be the consequences of the finite thickness of the sample. The distance between successive strings of atoms in the plane parallel with the channeling axis subtended $\sim 4\mu$rad over the thickness of the sample. The planar channeling effect is seen only once the electron beam is traversing many of these. The observation that planar channeling begins to manifest itself when the crystal

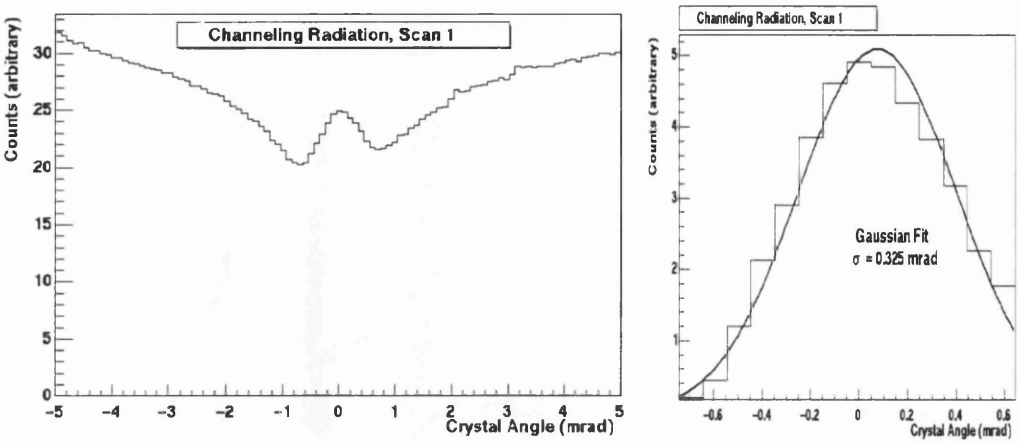

Figure 5.6: Scan 1.

angle exceeds $\sim$ 1 mrad suggests the electrons only "see" a plane once they are traversing around 250 of its constituent strings of atoms. This planar effect will not be apparent if there is an orthogonal offset to the rotation of the crystal, as is the case in scan 2, since then the beam satisfies channeling criteria only as the crystal angle passes through zero.

Scan 2

The results of scan 2 are shown in figure 5.7. A coherent edge is present at all angles because of the offset on the vertical orientation of the sample relative to the beam illustrated in the scan geometry. Summing over all energies between 500 MeV and 791 MeV gives the results shown in figure 5.8. As is expected from the scan geometry, planar channeling is seen at the angles at which the beam is aligned with the $(2\bar{1}0)$, $(1\bar{1}0)$ and $(1\bar{2}0)$ planes. However these peaks do not occur at the angles -2.5 mrad, 0 mrad and 2.5 mrad, but at the angles -2.5 mrad, 0 mrad and 2.8 mrad, which suggested some azimuthal and vertical misalignment of the sample. The peaks were fitted with Gaussians and found to have σ =

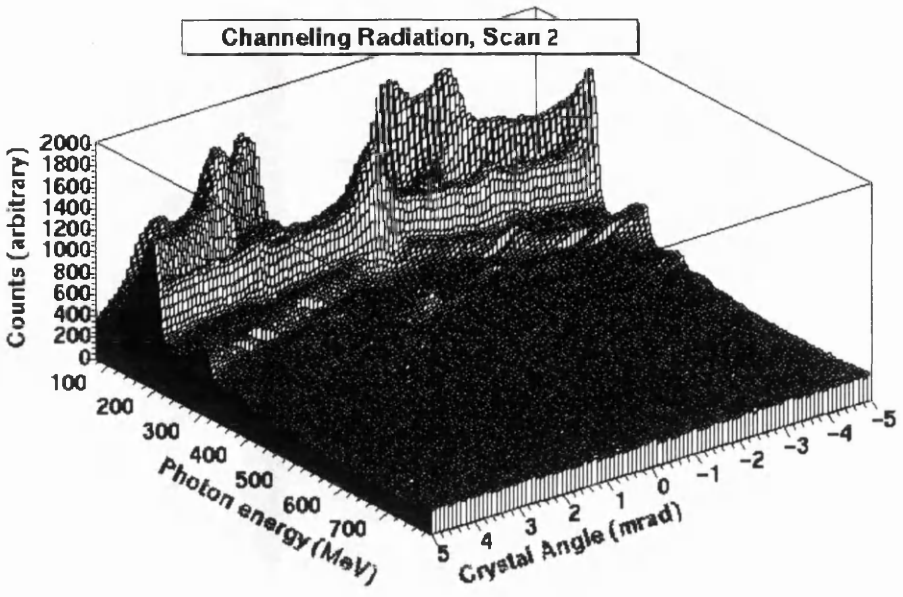

Figure 5.7: Scan 2.

153μrad, σ = 189μrad and σ = 94μrad, and FWHM of 360μrad, 445μrad and 221μrad, respectively, which are roughly twice the theoretical Lindhard angles for channeling of 124μrad, 220μrad and 124μrad as might be expected.

Knowing the distances between the plane crossings and the angles between those planes allowed the corrections to the offsets to be determined and the true scan geometry to be known. This is illustrated in figure 5.9. Figure 5.9 shows the section of figure 5.3 that illustrates scan B. The offsets misorient this scan, as is shown. The peaks in figure 5.8 occur where the scan crosses the crystal planes in figure 5.9, and the asymmetry of these peaks can be interpreted as being due to the misorientation of this scan. It is seen that if the azimuthal offset is β, the angles between the planes (equal in this symmetric case) are α, the measured distance between the peaks are a and b, and the true vertical offset is v. From the diagram it is seen that

$$\sin 2\beta = \frac{2(b-a)}{(b+a)tan\alpha}$$

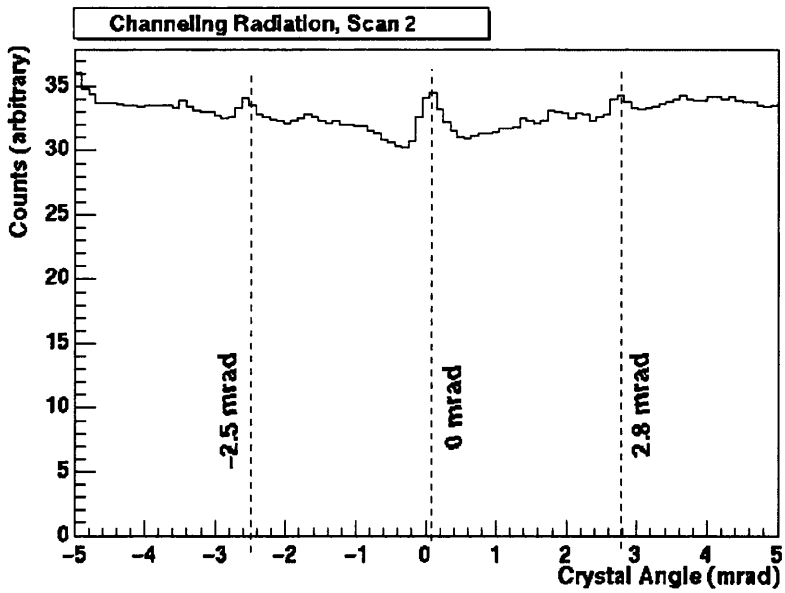

Figure 5.8: Scan 2.

$$v = a\left(\sin\beta + \frac{1}{\cos\beta\tan\alpha}\right)$$

In this case $\alpha = 22.5°$, a = 2.5 mrad and b = 2.8 mrad, which gives an azimuthal offset of $\beta = 7.93°$ and a vertical offset of v = 6.44 mrad.

The minima adjacent to the channeling peaks were not as pronounced as in scan 1, as expected.

Scan3

Scan 3 was identical in geometry to scan 1, but in this case collimation was applied, and so the experiment ran in gated scaler mode. The results are shown in 5.10. Summing over all energies from 500 MeV to 791 MeV gives results shown in 5.11. The width of the channeling peak was fitted with a Gaussian, with $\sigma = 350\mu$rad and FWHM = 824μrad, which is three times the Lindhard angle for axial channeling along this [100] axis, 238μrad. The peak occurs at the point in the scan when the crystal axis is pointing in the direction of the

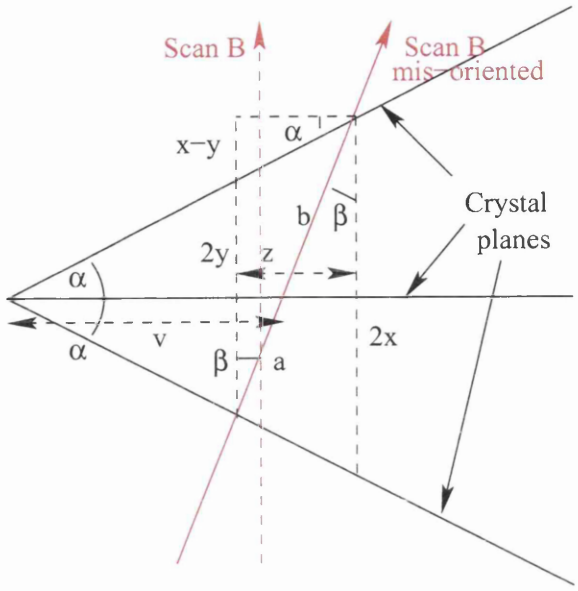

Figure 5.9: Finding the true scan geometry.

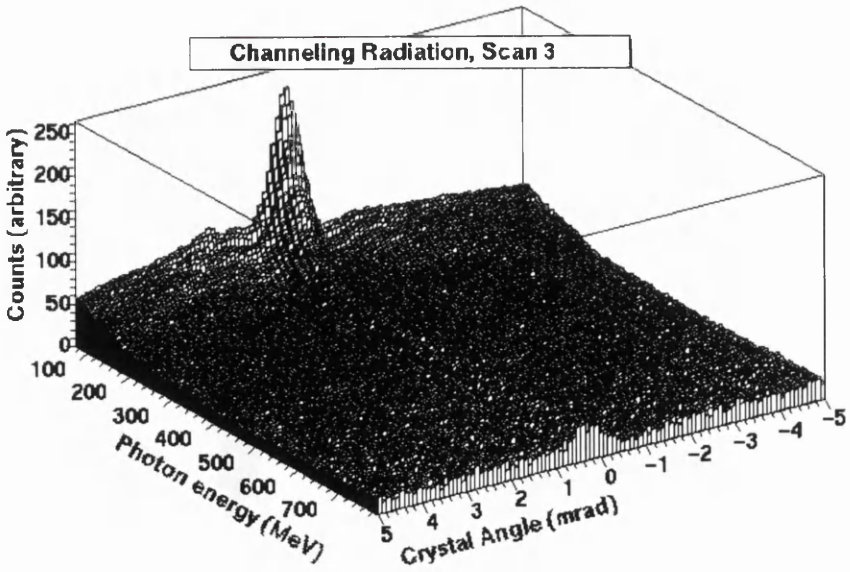

Figure 5.10: Scan 3.

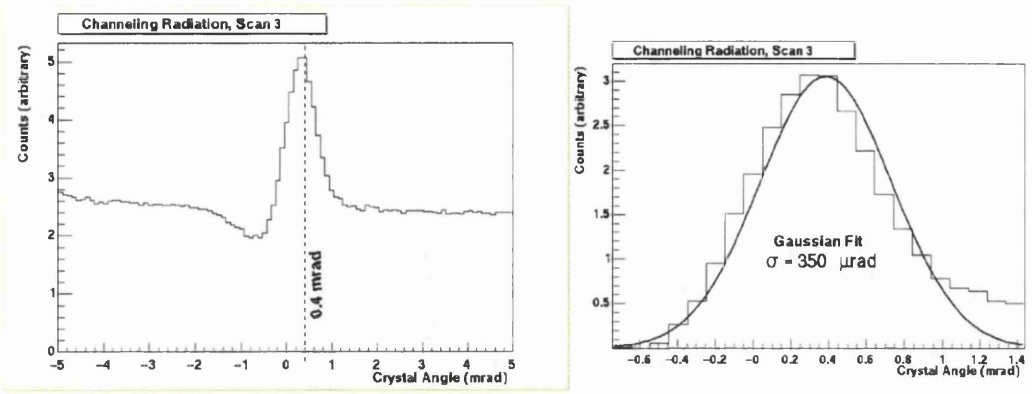

Figure 5.11: Scan 3.

collimation. The channeling radiation is emitted in the direction of the crystal axis, while the bremsstrahlung is emitted in the direction of the primary electron beam, therefore the greater prominence of the channeling peak is to be expected. $I_{rel.}^{max}/I_{rel.}^{min} \sim 2$ in the neighbourhood of this peak.

Scan 4

The sample was scanned with collimation applied such that the crystal axis at no point was directed towards the collimation. Both collimation and a vertical offset were applied. The results of summing over all energies between 500 MeV and 791 MeV are shown in figure 5.12. The peak occurs at a crystal angle of 0.2 mrad. The peak was fitted with a Gaussian and found to have $\sigma = 211\mu$rad, FWHM = 497μrad and $I_{rel.}^{max}/I_{rel.}^{min} \sim 1.5$. It can be deduced from the scan geometry that the peak represents planar channeling along the (110) plane. The FWHM is over twice the Lindhard angle, as is expected.

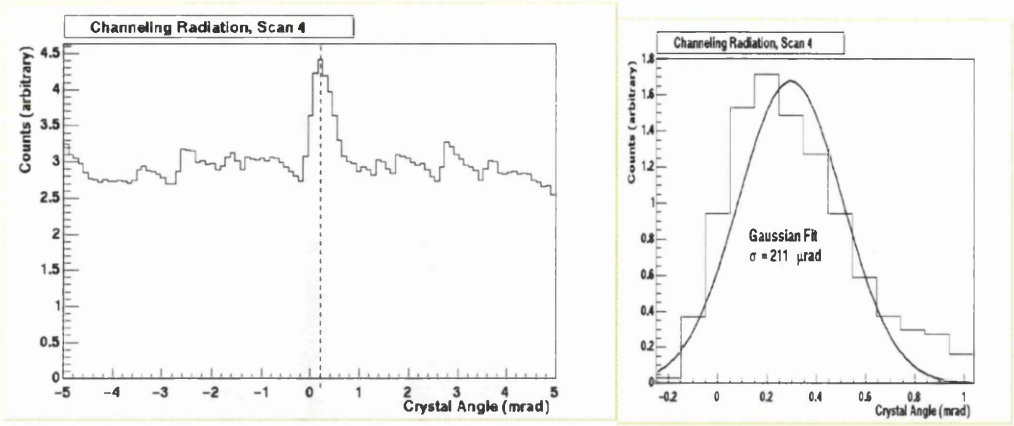

Figure 5.12: Scan 4.

5.3.2 Channeling on the [100] Axis - Sample 2

Scan 5

Scan 5 was identical in geometry to scan 1, but a thinner sample was used ($\sim$ 18μrad) which had not been subject to significant radiation damage. The results of performing scan 5 are shown in figure 5.13. Summing over the energies from 500 MeV to 791 MeV gave the intensity distribution shown in figure 5.14. It was found that the channeling enhancement was $I_{rel.}^{max}/I_{rel.}^{min} \sim 2.5$ in the neighbourhood of this peak. The width of the peak was ascertained, by fitting a Gaussian to it, with $\sigma = 153\mu$rad and FWHM = 360μrad, which is close to the Lindhard angle of 238μrad.

Again minima were observed between the axial and planar channeling regimes. The distance between the planes subtended $\sim$ 0.02 mrad over the thickness of the sample. If planar channeling does not occur at angles below which the electrons traverse no more than a sufficient number of constituent atomic strings of the plane, and the minima occur at $\sim$ 0.8 mrad, which is observed, then the electrons traverse only $\sim$ 40 atomic strings in this instance before behaving as though channeled. This lower number in comparison with sample 1 may be related to the

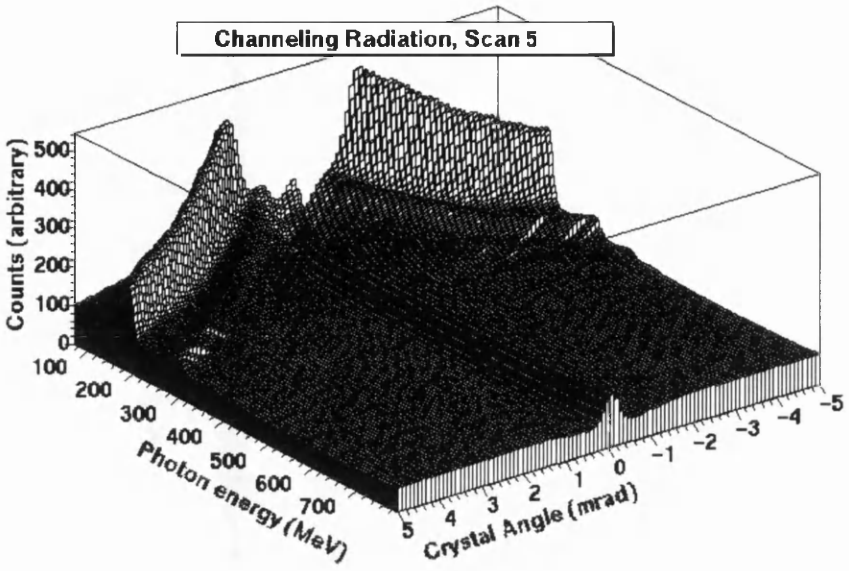

Figure 5.13: Scan 5.

radiation damage sample 1 experienced, which has resulted in sufficient numbers of defects being embedded in the lattice of sample 1 to increase the number of strings that must be traversed for planar channeling to occur by a factor of 6 with respect to sample 2.

Scan 6

Scan 6 was geometrically identical to scan 2. Ridging was again observed at the points in the scan where the electron beam was aligned with the $(2\bar{1}0)$, $(1\bar{1}0)$ and $(1\bar{2}0)$ planes, as expected from the scan geometry. The scan surface showing relative intensity against photon energy and crystal angle is shown in figure 5.15. The result of summing these results over the energy range 500 MeV to 791 MeV is shown in figure 5.16.

The peaks at -2.5 mrad, -0.5 mrad and 2.35 mrad were fitted with Gaussians and found to have $\sigma = 76\mu$rad, $\sigma = 97\mu$rad and $\sigma = 99\mu$rad, and FWHM of

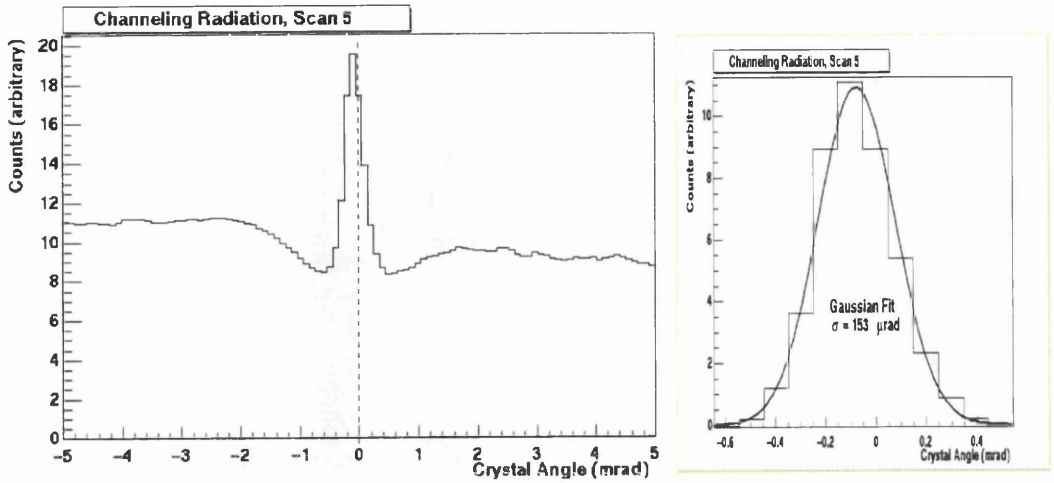

Figure 5.14: Scan 5.

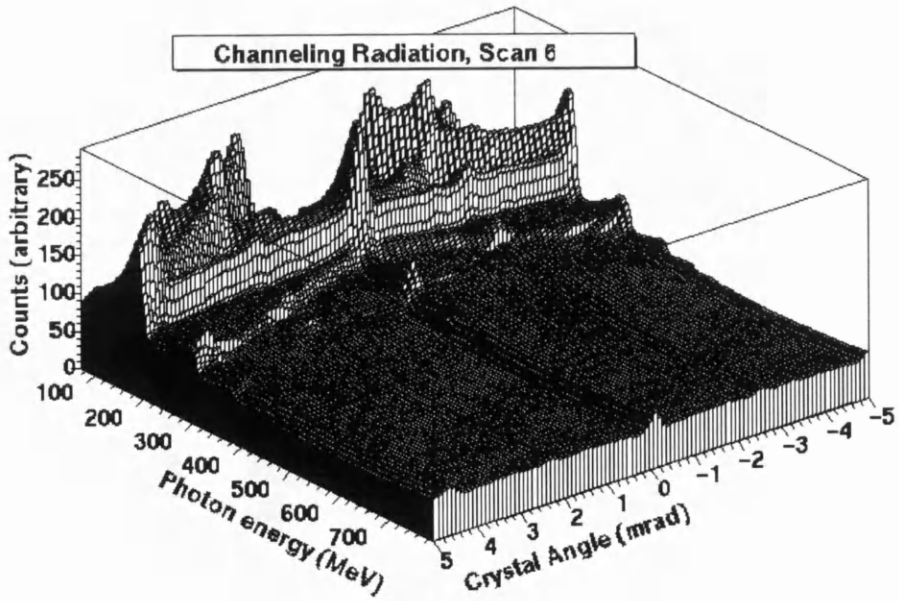

Figure 5.15: Scan 6.

179μrad, 228μrad and 233μrad, respectively. These are similar to the associated Lindhard angles of 124μrad, 220μrad and 124μrad. The fact that the peaks did not occur when the crystal angle was -0.25 mrad, 0 mrad and 2.5 mrad exactly, as would be expected from the scan geometry, suggested that crystal misalignment had occurred while installing the vertical offset of 5 mrad. As with scan 2, the azimuthal and vertical offsets were calculated and found to be $\beta = -1.45°$ and v = 5.855 mrad.

The widths of the peaks at -2.5 mrad and 2.35 mrad are influenced by the angle ϕ at which the scan traverses the planes these peaks represent. ϕ is the angle between the scan shown in red on the scan geometry and the plane causing the peak, for example in figure 5.19. To find the intrinsic widths the measured widths must be multiplied by $\sin\phi$. $\phi = 90° - \alpha \pm \beta$ where α is the angle between the plane and the scan rotation axis, and β is the azimuthal offset. The intrinsic widths of these peaks are found to be σ = 69.5μrad, FWHM = 164μrad in the case of the peak at -2.5 mrad and σ = 92.4μrad, FWHM = 218μrad in the case of the peak at 2.35 mrad. Both the FWHM are similar to the corresponding Lindhard angles.

Scan 7

Scan 7 was the same geometrically as scans 1, 3 and 5 other than the application of an azimuthal offset of 10°. This was applied to avoid a planar channeling background with local minima at the transition to an axial channeling regime, such that exclusively axial channeling could be investigated. The results are presented in figure 5.17. Figure 5.18 shows the intensity between 500 MeV and 791 MeV at the different angles the crystal axis made with the beam.

Three features were apparent in figure 5.18, at -1.4 mrad, 0 mrad and 1 mrad

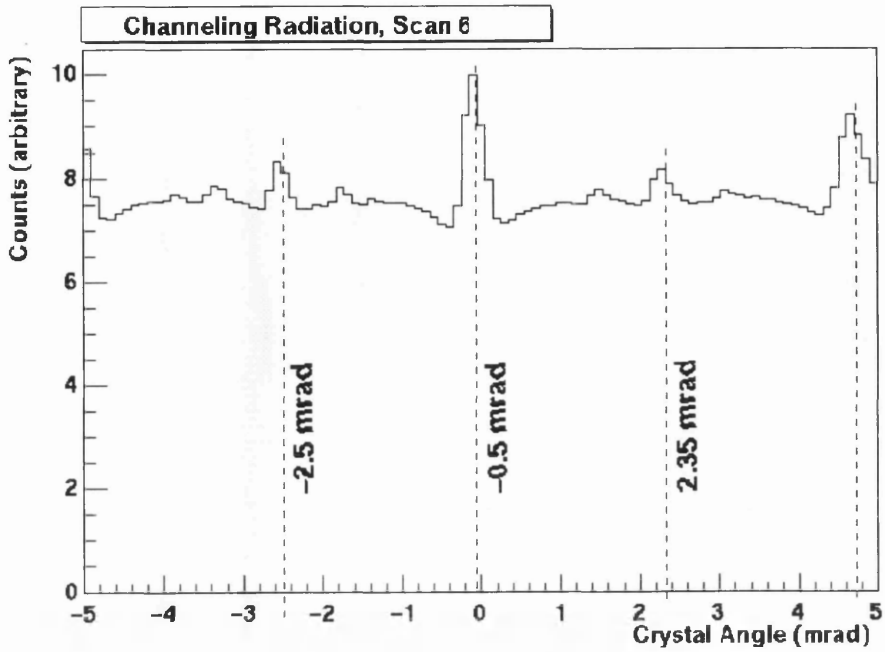

Figure 5.16: Scan 6.

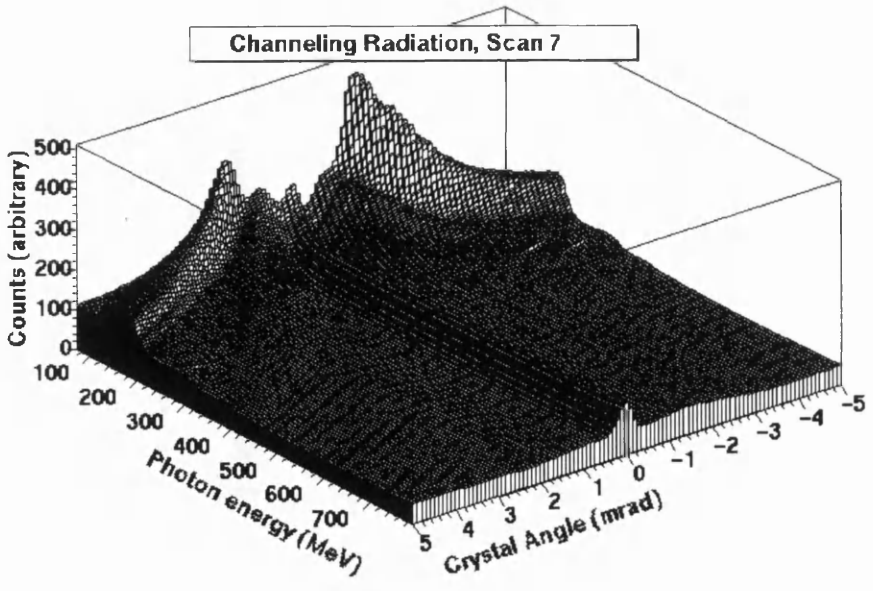

Figure 5.17: Scan 7.

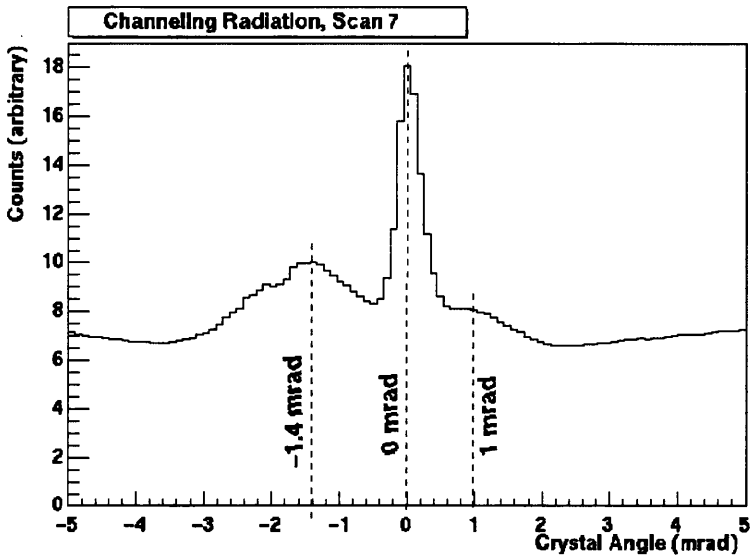

Figure 5.18: Scan 7.

respectively. They were fitted with Gaussians and found to have $\sigma = 885\mu$rad, $\sigma = 149\mu$rad and $\sigma = 696\mu$rad, and FWHM of 2084μrad, 351μrad and 1639μrad, respectively. This was interpreted with reference to figure 5.19 as the result of a vertical offset of $a \sin\beta = 0.24$ mrad having been introduced during the installation of the azimuthal offset, where $\beta = 10°$ is the azimuthal offset. The oblique angle at which the scan traverses (110) results in the broadening of the leftmost peak in figure 5.17 by $1/\sin\beta$, such that the intrinsic width of this peak is $\sigma = 885 \sin\beta = 153\mu$rad, FWHM $= 360\mu$rad. This intrinsic width is close to that of the main peak and both FWHM are greater than the Lindhard angles for these planes, 220μrad.

5.3.3 Channeling on the [110] Axis - Sample 3

Sample 3 gave the opportunity to investigate channeling on the [110] axis.

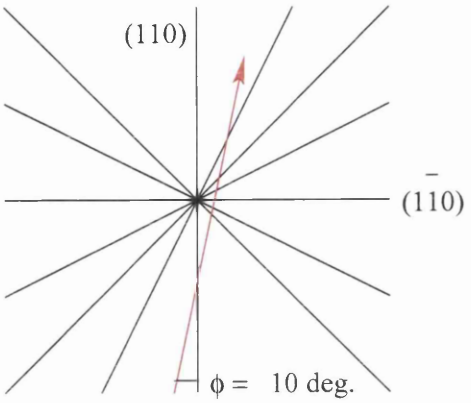

Figure 5.19: The geometry of scan 7.

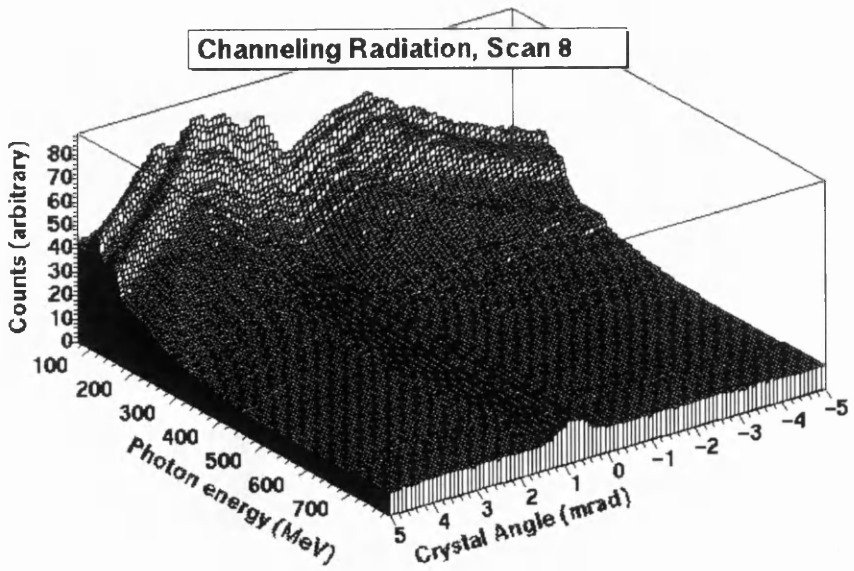

Figure 5.20: Scan 8.

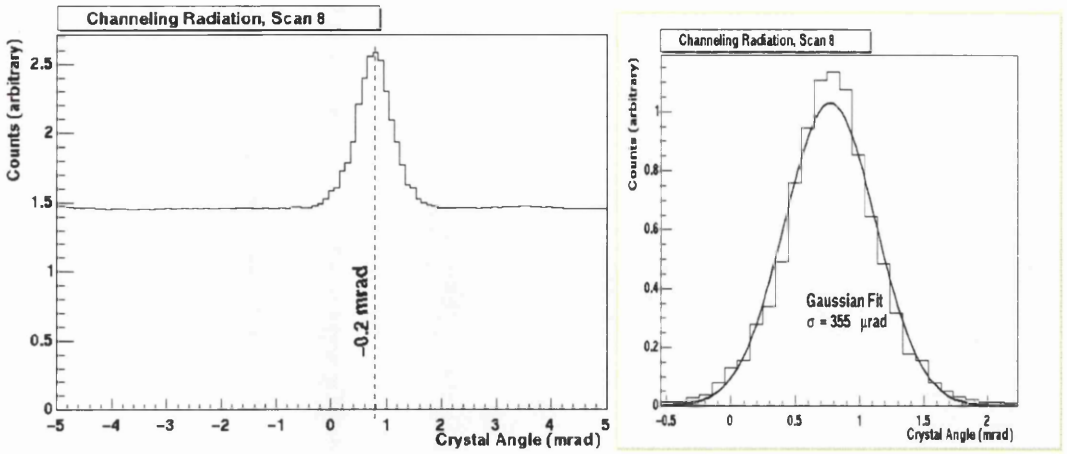

Figure 5.21: Scan 8.

Scan 8

The results of performing scan 8 are shown in figure 5.20. The relative intensity summed from 500 MeV to 791 MeV is shown in figure 5.21. The peak occurs at -0.2 mrad and the minima that occur between the axial and channeling regimes are not in evidence. This suggests some slight misalignment. The peak has $\sigma = 355\mu$rad, and a FWHM = 836μrad, which is three times the Lindhard angle of 283μrad. $I_{rel.}^{max}/I_{rel.}^{min} \sim 1.7$

Scan 9

Scan 9 was asymmetric, running from a crystal angle of -5 mrad to a crystal angle of 15 mrad. This is shown in figure 5.22. Figure 5.23 shows the intensity added for energies from 500 MeV to 791 MeV. Peaks are observed at -3 mrad, -0.2 mrad, 2.1 mrad, 4.3 mrad, 6.5 mrad and 10 mrad. It was apparent that once more the application of an azimuthal offset had introduced an unknown rotational offset.

Given the scan geometry and the existence of 6 peaks, the 1st and 5th peaks were chosen to calculate the offsets, and these were calculated independently

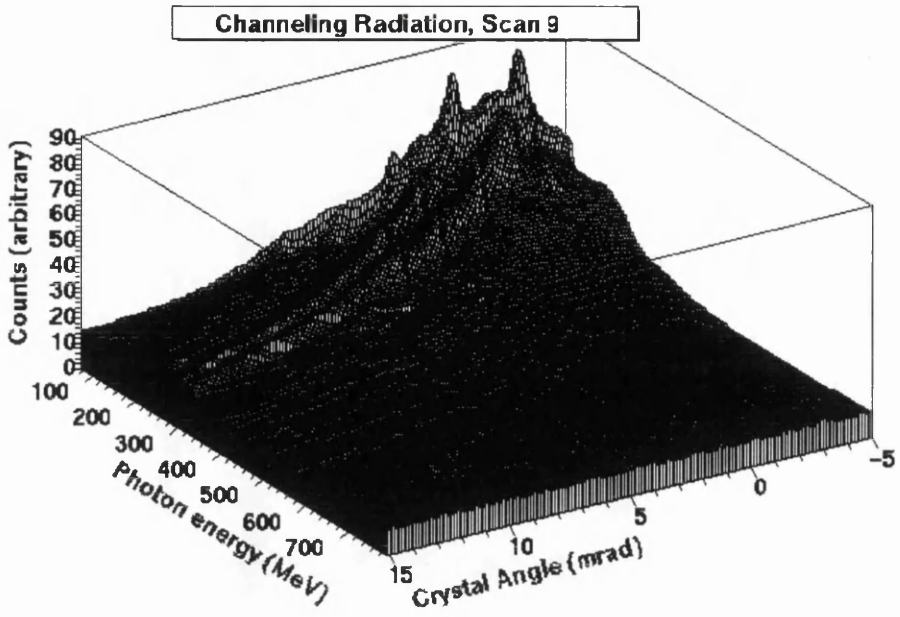

Figure 5.22: Scan 9.

using the 2nd and 4th peak positions. The 3rd peak was interpreted as deriving from channeling along the (100) plane. If the 4th peak was thus interpreted, then the intervals between it and each of its two nearest neighbouring peaks would be equal, which would be consistent with only 5 peaks being evident, from the implied symmetry of the scan geometry. The observation of 6 peaks implies an asymmetric scan geometry. This is illustrated in figure 5.24.

Using the 1st and 5th peaks, an azimuthal offset of $\beta = -3°$ and a horizontal offset of 3.349 mrad were calculated. Using the 2nd and 4th peaks, an azimuthal offset of $\beta = -1.8°$ and a horizontal offset of 3.178 mrad were calculated. The correct scan geometry was deemed to be $\beta = -2.6°$ and h = 3.26 mrad, and that the ridges correspond to the beam traversing the $(1\bar{1}1)$, $(2\bar{1}1)$, (100), (211), (111) and (011) planes as the angle between it and the crystal is scanned.

The widths of the peaks found from fitting Gaussians to them were $\sigma = 164\mu$rad, $\sigma = 120\mu$rad, $\sigma = 174\mu$rad, $\sigma = 183\mu$rad, $\sigma = 112\mu$rad and $\sigma = 170\mu$rad, and

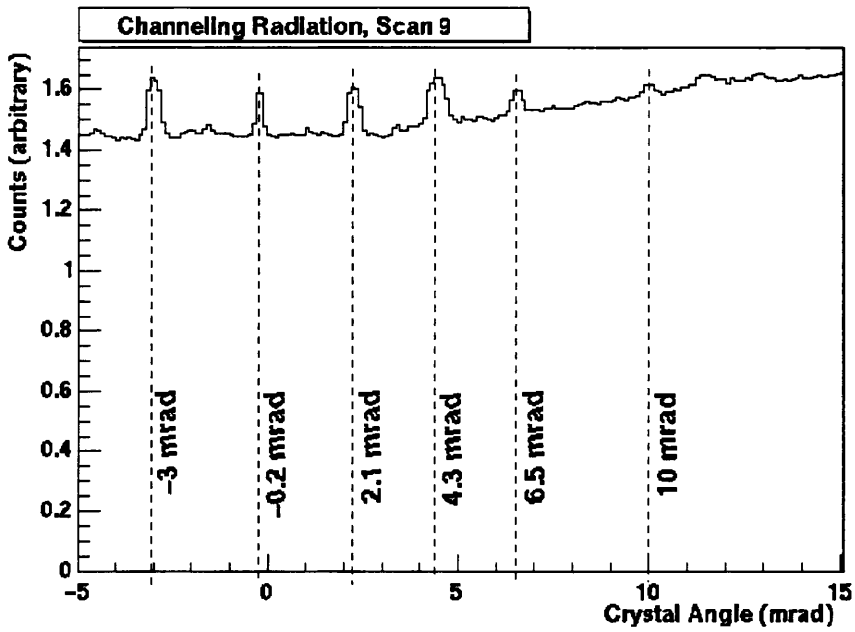

Figure 5.23: Scan 9.

FWHM = 386μrad, FWHM = 283μrad, FWHM = 410μrad, FWHM = 431μrad, FWHM = 264μrad and FWHM = 400μrad, respectively.

5.3.4 Line Widths

Table 5.4 summarises the results pertaining to the widths of the channeling peaks, that is, the range of angles in a scan where the beam was sufficiently closely aligned with and axis or plane for the electrons to be channeled. The widths referred to are the σs and FWHMs derived from Gaussian fits of the peaks. Where the value of the width has been scaled because the scan traversed a plane at an oblique angle, the corrected value is shown in brackets. The FWHM of the peaks are 2.3548σ. The results are listed by sample, then scan, then the channeling plane or axis is listed, followed by the observed value of σ, the FWHM and the Lindhard angle.

Channeling radiation peak angular widths					
Sample	*Scan*	*Channel*	σ μrad	*FWHM* μrad	*Lindhard* μrad
1	1	[100]	325	765	238
1	2	$(2\bar{1}0)$	153(141)	360(332)	124
1	2	$(1\bar{1}0)$	189	445	220
1	2	$(1\bar{2}0)$	94(87)	221(205)	124
1	3	[100]	350	824	238
1	4	(110)	211	497	220
2	5	[100]	153	360	238
2	6	$(2\bar{1}0)$	76(69)	179(164)	124
2	6	$(1\bar{1}0)$	97	228	220
2	6	$(1\bar{2}0)$	99(92)	233(218)	124
2	7	(110)	885(153)	2084(360)	220
2	7	(101)	149	351	220
2	7	-	696	1639	-
3	8	[110]	355	836	283
3	9	-	164	386	-
3	9	-	120	283	-
3	9	-	174	410	-
3	9	-	183	431	-
3	9	-	112	264	-
3	9	-	170	400	-

Table 5.4: The channeling peak widths.

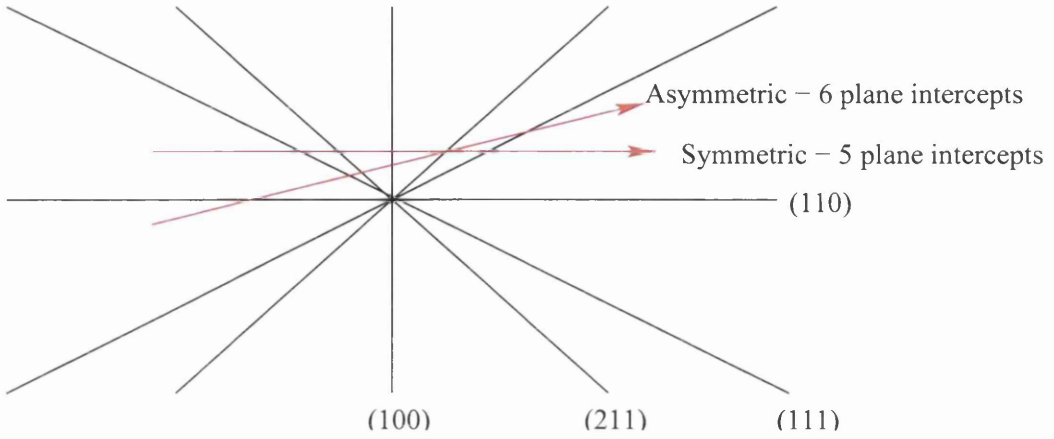

Figure 5.24: Symmetric and asymmetric scans.

5.3.5 Dechanneling

Electrons can be scattered out of the channeling regime of angular incidence as a result of encountering defects or due to thermally induced vibrations of the lattice ([49, 50, 51] among others). At the beam currents operated in this study the electrons do not interact with each other, indeed the average number of channeled electrons instantaneously present in the lattice is less than unity. Diamond is a particularly favourable material to use in channeling experiments from the point of view of dechanneling as its high Debye temperature ensures that lattice vibrations at room temperature have very long wavelengths. The dechanneling length of diamond at room temperature, that is, the depth to which the beam penetrates after which there has been a reduction of the fraction of electrons in the channeling regime due to dechanneling by a factor of e^{-1}, is $\sim 40\mu$m [52]. This is of the same order of magnitude as the thickness of the radiators investigated in this study. A comparison of the widths and channeling enhancements of the relative intensity between sample 1 and sample 2 is consistent with the hypothesis that dechanneling occurs in sample 1 to a greater extent, partly due to its thickness and partly due to the defects in it which are a consequence of the

radiation damage it has sustained.

5.4 Conclusions

Channeling radiation is emitted at all energies when the channeling criteria regarding crystal angle are met. The enhancement is improved by an order of magnitude by the application of collimation. This renders the radiation useful as a source of photons for use in photonuclear studies, with intensities up to 2.5 times higher than the background attainable. The observed widths of the channeling peaks in terms of crystal angle are consistent with the calculated Lindhard or critical angles for channeling.

The emission of planar channeling radiation is applicable in photonuclear studies, since these photons are linearly polarised and the enhancement due to channeling is observed at all energies. The polarisation arises due to the dimensionality of one of the interplanar potential governing the trajectories of the channeled electrons. Axial channeling radiation is not polarised, since the string potential governing the motion of the electrons has zero dimensionality. However, the axial channeling radiation is useful in addition, since the enhancement over the incoherent background it represents is greater at higher energies.

The effects of dechanneling are apparent when the results of scattering electrons from diamonds of two different thicknesses are compared - the channeling radiation from the thick sample has no practical utility given the meager enhancement over the background it exhibits. The large enhancement associated with the thin sample indicates that channeling radiation from thin samples could be used as a viable source of high energy photons in preference to incoherent bremsstrahlung. The thicker sample had sustained radiation damage through heavy use as a coher-

ent bremsstrahlung radiator and it must be considered that blocking of channeled electrons by self-interstitials may account for its poor performance. This requires further investigation.

The initially striking observation of regularly spaced ridges in the channeling scans proved to be a consequence of difficulties in aligning the crystal, corresponding to planar channeling.

Chapter 6

Conclusions and Future Developments

6.1 Conclusions

At the outset of this study three related questions were posed.

1. How does one go about selecting the best diamonds to use to produce coherent bremsstrahlung in photonuclear experiments ?

2. Does the performance of the diamond deteriorate as a result of its use ? Does it sustain damage which degrades its performance ?

3. Can diamonds be used in ways other than the production of coherent bremsstrahlung to provide a photon beam for photonuclear studies ? Specifically what are the properties of channeling radiation and do these properties lend themselves to photonuclear studies ?

The answers to these questions must be considered in relation to the need to provide a photon beam with a high degree of linear polarisation. The coherent component of photon emission is the polarised part, and the incoherent component is unpolarised.

6.1.1 Diamond Selection

A variety of tests were deployed in order to see how their results were correlated with optimal diamond performance. A broad distinction could be made between diamonds on the basis of a polarised light analysis which revealed the strain in the them. More detailed qualitative information could be obtained using x-ray topography which vividly revealed linear defects. A quantitative measurement of the extent to which the direction of a reciprocal lattice vector had been blurred was given with a rocking curve analysis. It was found that type II diamonds are unsuitable; although they have a low nitrogen content their behaviour is dominated by the plastic deformation they have undergone, which renders them

unsuitable. This can be detected with the least expensive test (the first that should be deployed when faced with a new candidate diamond), which is polarised light analysis.

Specimens that are not rejected on the basis of the petrographic images acquired during polarised light analysis should then be scrutinised using x-rays. x-ray topography will reveal features in greater detail than polarised light. Rocking curves will give a quantitative measurement of the quality of the diamond in terms of the breadth of its rocking curve in comparison with the ideal.

The improvement in quality as one considers thinner diamonds was striking. Thinner diamonds perform much better than thicker diamonds.

It was found that damage or imperfections in a diamond may not cause the reciprocal lattice vector to vary in direction sufficiently to broaden the coherent edge in a coherent bremsstrahlung spectrum, but there may be sufficient to raise the incoherent background to a level that greatly reduces the degree of linear polarisation. This can be understood by considering the difference in magnitude of the characteristic angle of coherent bremsstrahlung, $\sim 600\mu$rad, and the typical rocking curve width of a good diamond, $\sim 6\mu$rad. The variation in the direction of a reciprocal lattice vector typical of a poor specimen will manifest itself as a severe broadening of its rocking curve while it nevertheless retains a sharp coherent edge in its coherent bremsstrahlung. However the incoherent background on which the coherent emission is superimposed is enhanced at all energies by the damage, and so the degree of linear polarisation is reduced.

6.1.2 Diamond Degradation

The properties of a diamond which had been exposed to significant amounts of beamtime were studied using the tests used to ascertain diamond quality, and

spectroscopic tests which can be used to investigate the impurities and defects in diamond. The spectroscopic techniques were found to be of little significance; the properties to which they were sensitive were not of real importance for coherent bremsstrahlung. The cathodoluminescence spectrum was consistent with the specimen being of synthetic origin.

The damaged diamond exhibited a massively broadened rocking curve in the region where most of the damage was concentrated. The coherent edge in the coherent bremsstrahlung spectrum remained reasonably sharp, but it was seen by comparison with theory that the incoherent component was greatly enhanced at all energies, thereby degrading the degree of linear polarisation obtainable using this specimen.

6.1.3 Diamond Utilisation

Despite difficulties aligning the samples, planar and axial channeling radiation was observed from a variety of specimens. Again the sample that exhibited the most favourable properties, such as yielding results closest to theory, and showing the greatest channeling photon beam intensity enhancement, was the thinnest. The utility of this phenomenon is limited; although the photon flux is enhanced at all energies, including high energies, for axial channeling, the beam is unpolarised, and so nothing can be achieved which could not otherwise be achieved by using a higher primary electron beam current.

6.2 Further Investigation of Channeling Phenomena

One important avenue of investigation that has not been adequately covered by the present study is that associated with the angular distribution of the emergent photons associated with channeling radiation. In this study the energy distribution of photons for different orientations of crystal radiator has been surveyed. However, detailed information concerning the angular distribution of the photons themselves was not obtained. This information should be acquired with a much finer resolution than the crude resolution available due to offset collimation in order to ascertain if there are any parts of the emission which might be collimated on to isolate a potentially useful component of the emitted photon flux.
A strip detector could be employed in line with established methods [53]. This would provide an array of pixels, such that photons were dealt with on an event-by-event basis. Spurious high energy features resulting from multiple emission could be resolved. Features that are more prominent at certain angles could be investigated with a view to collimating on them.

6.3 Further Investigation of Selection Criteria for Crystal Radiators

The work presented here should be seen as a commencement, rather than a conclusion, of investigations into selection criteria for diamond radiators. New specimens that have been first studied in the course of the work presented here and have yet to experience the high doses of high energy irradiation should be regularly monitored to see how their properties change.

List of Figures

List of Tables

Bibliography

[1] Calum Powrie. A study of the $^{12}C(\gamma,pp)$ reaction. Ph.D. Thesis, University of Glasgow, 1999.

[2] S. Boffi, C. Giusti, F.D. Pacati, and M. Radici. *Electromagnetic Response of Atomic Nuclei.* Oxford University Press, 1996.

[3] W. Heitler. *The Quantum Theory of Radiation.* OUP, at the Clarendon Press, 1954.

[4] J.U. Andersen. Notes on channeling. Private communication, 1997.

[5] U. Timm. *Fortschritte der Physik*, 17:765, 1969.

[6] G. D. Palazzi. *Rev. Mod. Phys.*, 49:611, 1968.

[7] J. Kellie *et al.* The selection of crystal radiators for the production of coherent bremsstrahlung. University of Glasgow, 2001.

[8] R.O. Avakyan *et al. JETP Lett.*, 21(7):206, 1975.

[9] C. Erginsoy. *Phys. Rev. Lett.*, 15(8):360, 1965.

[10] E. Uggerhoj. *Physics Letters*, 22(4):382, 1966.

[11] E. Bogh and J.L. Whitton. *Phys. Rev. Lett.*, 19(10):553, 1967.

[12] J. Lindhard. *Mat.Fys.Medd. Dan.Vid.Selsk.*, 34(14):1, 1965.

[13] M.A. Kumakhov. *Physics Letters A*, 57(1):17, 1976.

[14] M.A. Kumakhov. *Sov. Phys. Dokl.*, 21(10):581, 1976.

[15] J.F. Bak *et al. Nuclear Physics B*, 242:1–30, 1984.

[16] J. Bak *et al. Physics Letters*, 93B(4):505, 1980.

[17] A.F. Elishev *et al. Physics Letters*, 88B(3,4):387, 1979.

[18] Yu.A. Chesnokov, V.M. Biryukov, and V.I. Kotov. *Phys-Uspekhi*, 37(10):937, 1994.

[19] B. K. Tanner and D. K. Bowen. *High resolution X-ray diffractometry and topography.* Taylor and Francis, 1998.

[20] R. O. Owens. *NIM A*, A288:574, 1990.

[21] L. Van Hoorebeke *et al. NIM A*, 321:230, 1992.

[22] I. Anthony *et al. NIM A*, 301:230, 1991.

[23] S. J. Hall *et al. NIM A*, 368:698, 1996.

[24] A. Schmidt. Diplomarbeit. Master's thesis, Instituet der Kernphysik, Mainz, 1995.

[25] K. Livingston. The stonhenge plot - a crystal alignment technique. University of Glasgow, 2001.

[26] D. Lohmann *et al. NIM A*, 343:494, 1994.

[27] C. Kittel. *Introduction to Solid State Physics.* John Wiley and Sons, 1986.

[28] S. Elliott. *The Physics and Chemistry of Solids.* John Wiley and Sons, 1998.

[29] E. Henderson. *Defects in Crystalline Solids.* John Wiley and Sons, 1998.

[30] A. Natter. A coherent bremsstrahlung simulation code. Private communication, 2001.

[31] G. Davies. *Diamond.* Adam Hilger, 1984.

[32] J.E. Field, editor. *The Properties of Diamond*, chapter 1. London: Academic, 1979.

[33] B. K. Tanner. *X-ray diffraction topography.* Pergamon, 1976.

[34] J. Harris. Radiation damage of mainz diamond. Private communication, 1999.

[35] A. T. Collins. *Diamond and related materials*, 9:417, 2000.

[36] J. A. Ellison. Theory of particle motion in straight or distorted crystals. In Jr. R. A. Carrigan, editor, *Relativistic Channeling.* Plenum, 1986.

[37] G. Shirmer and M. A. Kumakhov. *Atomic Collisions in Crystals.* Gordon and Breach, 1989.

[38] W. Lotz *et al. NIM B*, 48:256, 1990.

[39] S. Satpathy and A.P. Pathak. *NIM B*, 48:248, 1990.

[40] B. Gruska and G. Goetz. *NIM*, 194:199, 1984.

[41] J.U. Andersen *et al. NIM*, 194:209, 1984.

[42] M. Gouanere *et al. NIM*, 194:225, 1984.

[43] S.D. Bloom *et al. NIM*, 194:229, 1984.

[44] R.L. Swent *et al. NIM*, 194:235, 1984.

[45] N.A. Filatova *et al. NIM*, 194:239, 1984.

[46] A. Ootuka, K. Komaki, and F. Fujimoto. *NIM*, 194:243, 1984.

[47] D. Mihalache, V.K. Fedyanin, and G.M. Gavrilenko. *NIM*, 194:247, 1984.

[48] A.P. Pathak and B. Rath. *NIM*, 194:251, 1984.

[49] Yu. V. Kononets and V. A. Ryabov. *NIM B*, 48:187, 1990.

[50] K. Gaertner, W. Wesch, and G. Goetz. *NIM B*, 48:192, 1990.

[51] K. Kimura and M. Mannami. *NIM B*, 48:197, 1990.

[52] M. A. Kumakhov and F. F. Komarov. *Radiation from charged particles in solids.* AIP, 1989.

[53] T. Davinson *et al.* *NIM A*, 28:245, 1990.